# STUDIES OF LEVITATED SINGLE DROPLETS

Thesis by :

**Chak Keung Chan**

In Partial Fulfillment of the Requirements

for the Degree of

Doctor of Philosophy

California Institute of Technology

Pasadena, California

1992

(Submitted September 26, 1991)

**Dedicated to My Late Father**

**Acknowledgments**

I would like to thank my advisors, Professors John Seinfeld and Richard Flagan for their technical advice, financial support, and patience during my graduate studies in Caltech. Their understanding and encouragement at times when frustration seemed to be the epitome of research progress was very much appreciated. I also enjoyed our research meetings where I learned about the right attitudes towards research. In addition, I am very grateful to Dr. Brian Wong who has helped me in many facets of my experiments, especially in the early stage of my research.

I am fortunate to have had a group of nice people to work with: Brian, Steve, Aaron, Xiaoming, Shih Chen, Missy, and Barbara. All of you have made working in the lab more fun than it seems. I also enjoyed many discussions with my officemate, Yong Kim, about graduate studies and life in general. I would like to thank Thomas Au and Frederick Cheung for their support and concern during these few years. Chris Koh and Ricky Ng, two of my best friends in Caltech have given me much advice and support in my graduate studies. I also have had a wonderful time with Alex, Atta, Chi, Richard, and Pete. I surely will remember those days when going out for Chinese dinners and Chinese movies afterwards was a weekend ritual.

I will be forever grateful for the support of my parents and family members at home. It has been almost nine years since I left home and came to the United States. I enjoyed every moment with them on my occasional holidays in Hong Kong. They have sacrificed a lot in supporting my pursuit of higher education

and personal interests. Without their indulgence in letting me excuse myself from family responsibilities, my graduate study would not have come true.

Finally, I am very thankful to my wife, Anna, for her support and understanding throughout my graduate studies. She sacrificed her own brilliant and dynamic career in Hong Kong and came to the United States to stay with me. Without her company and encouragement, my final year at Caltech would have been quite miserable.

**Abstract**

The electrodynamic balance is a very unique and versatile device to study single particles. *In-situ* measurements of particles in a well characterized and controlled environment are possible. Supersaturated solutions can also be studied. In this research, its applications in studying light scattering, water activities and evaporation kinetics of single droplets are demonstrated. In particular, we studied the elastic and Raman scattering of an evaporating $NaNO_3$ droplet. Different types of size dependent optical resonance structures were identified. The strongest Raman signal received was due to internal resonance of the excitation beam, giving similar enhancements to all Raman emissions. The intensity ratio of Raman nitrate to Raman water peaks can be used as a probe to semi-quantitatively characterize the droplet compositions.

Water activities of mixed $NH_4NO_3/(NH_4)_2SO_4$ aqueous solutions were also studied using the Spherical Void Electrodynamic Levitator. The compositional water activity data were used to evaluate the performance of three commonly used mixed electrolyte models: the Zdanovskii-Strokes-Robinson model, the Kusik and Meissner model, and the Pitzer model. They all predict droplet concentrations in mass fractions to a few percents error within the range where water activity data of single electrolytes are available. Evaporation of a few ceramic precursor solution droplets were investigated. While some precursor solutions crystallized, some others formed gels. Gel formation hindered further evaporation of water and the droplets exhibited a sharp decrease in evaporation rates. An approach to study rapid evaporation of droplets in the time scales of a few seconds was also demonstrated.

## Table of Contents

## List of Tables

### Chapter 3



### Appendix 3

## List of Figures

Chapter 2

**Chapter 3**

**Appendix 1**



**Appendix 2**



**Appendix 4**



**Appendix 5**

# Chapter 1

## Introduction

In the past ten years, the electrodynamic balance has been recognized as a very unique tool to study aerosol particles. It enables *in-situ* measurements of well characterized single particles in a controlled environment virtually as long as one desires. Using a quadroupole electric field in the electrodynamic balance, micron-sized particles can be trapped. A single particle can be levitated stationary when its weight is balanced by the force it experiences due to an applied DC field. Light scattering requiring an extended period of time for characterization of particles can therefore be studied. Spectroscopic technique can then be applied to determine the chemical composition of a single particle, with an ultimate goal of understanding the reaction kinetics of chemical processes occurring in a single particle. Since the droplet is not in contact with any foreign surface, extremely high supersaturation ratio can be achieved. The thermodynamic and transport properties of supersaturated solution can then be studied. In addition, mass change of a particle can be easily followed by monitoring the DC potentials. The concentration of a droplet is known by measuring its required DC potential and that of the dried particle resulting from crystallization. The compositional dependence of water activity of aqueous solutions can be obtained from the composition of a droplet in equilibrium with its ambient relative humidity. Furthermore, the history of the mass loss of an evaporating droplet can also be determined.

In Chapter 2, the studies of resonance structures in elastic and Raman

scattering from microspheres are presented. Raman spectroscopy recently received some attention as a potential technique to determine chemical composition of aerosol particles. Whereas chemical compositions of irregularly shaped particles can be readily determined, quantitative chemical speciations of droplets or other spherical particles are complicated by Mie resonances. Mie resonance is a phenomenon observed in elastic scattering of spherical objects in which the light intensity scattered and absorbed are extremely strong functions of the size parameter, $X$ (defined as particle size over wavelength), when $X > 10$. In order to understand the role of Mie resonance in Raman spectroscopy of droplets, we measured the elastic and Raman scattering of a slowly evaporating sodium nitrate droplet simultaneously using an optical multichannel analyzer. As the droplet slowly evaporated, $X$ decreased and crossed a few Mie resonances. By comparing the measured intensity profiles of the elastically scattered laser light (at 488.0 nm) and the Raman emissions of nitrate (at 514.1 nm) and water (at 578nm to 606 nm), the interactions between Mie scattering and Raman emissions were investigated. Different types of resonances in the Raman emissions were identified and discussed. The strongest signal measured was due to the internal resonance of the excitation beam, giving similar enhancements of the nitrate and the water peak. A roughly linear relationship between the nitrate peak intensity and the water peak intensity was obtained. The use of Raman spectroscopy to semi-quantitatively determine droplet compositions is demonstrated in Appendix 1 where Raman spectra of a $NaNO_3$ droplet of changing concentrations from under saturation to supersaturation are presented.

Chapter 3 describes an experimental study to determine the water activities of

mixed $NH_4NO_3/(NH_4)_2SO_4$ aqueous solutions. The thermodynamics of the $NH_4NO_3$-$(NH_4)_2SO_4$-$H_2O$ system are important to the understanding of the properties of atmospheric aerosols. Of central importance is the effect of ambient relative humidity on the equilibrium composition of droplets of this system. In addition, ammonium nitrate is a volatile salt and ultimately leaves a droplet in the form of gaseous ammonia and nitric acid. Compositional data as a function of relative humidity are also essential to understanding the effect of $(NH_4)_2SO_4$ on the loss of $NH_4NO_3$ from a mixed solution droplet. At equilibrium, the water activity of an aqueous droplet equals to the ambient relative humidity. We intended to determine the compositional effects on the water activity of the droplets of mixed $NH_4NO_3/(NH_4)_2SO_4$ solutions. The ambient relative humidity can be controlled by flowing a stream of humidified nitrogen through the balance. However, the time for measurement of each droplet needs to be minimized because of the volatility of $NH_4NO_3$. The electrodynamic balance which was used in the light scattering experiments in Chapter 2 are housed in a vacuum chamber of about 350 ml. The excessive volume of the chamber prohibits efficient conditioning of the ambient relative humidity. Therefore, a new balance, smaller balance in the form of a spherical void with volume 4 ml was constructed so that thermodynamic measurement of each droplet was finished in about four hours. Within this period, no appreciable loss of $NH_4NO_3$ was observed. We measured the compositions of droplets at various known $NH_4NO_3/(NH_4)_2SO_4$ mole ratios as a function of relative humidity. The compositional water activity data were also used to evaluate the performance of three mixing models of electrolytes solutions commonly used in atmospheric chemistry: the Zdanovskii-Stokes-Robinson, the Kusik and Meissner, and the Pitzer models. These models require only the

water activity data of individual $NH_4NO_3$ and $(NH_4)_2SO_4$ solutions. Within the range of water activity or concentration where water activity data are available, these models all predict the concentration in mass fractions to a few percents error.

The use of the electrodynamic balance to study evaporation kinetics is also demonstrated in the appendices. Evaporation studies of a few ceramic precursor solution droplets are reported in Appendix 4. Instead of crystallizing to form dried particles, some of these solution droplets formed gels. The formation of gel drastically reduced the evaporation rate and its onset was also evident from light scattering of the particle. The results of these preliminary studies suggest different drying characteristics for different ceramic precursors, which may ultimately lead to understanding the control of particle morphology in the process of spray pyrolysis.

Study of evaporation in a time scale of a few seconds using a flowing system to change the ambient relative humidity is difficult since the residence time employed is usually much longer than a few seconds. An approach was devised to study rapid evaporation of aqueous droplets such as NaCl solutions by dropping a droplet into a well controlled relative humidity environment. The experimental procedures and the results are presented in Appendix 5. The mass loss of an evaporating droplet was followed by an electro-optical servo system. Evaporation process occurring in a time scale of 1 second was monitored. Simple gas diffusion limited transport theory with and without evaporation cooling of the droplet were used to compare with experimental measurements. The time scale of the measured evaporation process matches

that of the theoretical predictions, indicating that the approach is suited for intrinsic evaporation studies in the order of a few seconds. Also, predictions taking considerations of evaporation cooling of the droplet are more consistent with the experimental data.

Chapter 2

# RESONANCE STRUCTURES IN ELASTIC AND RAMAN SCATTERING FROM MICROSPHERES★

Chak K. Chan, Richard C. Flagan, and John H. Seinfeld

Department of Chemical Engineering

California Institute of Technology

Pasadena, CA 91125

★ As appeared in *Applied Optics* **30(4)**, 459-467, 1991

Abstract

To study the interactions between Mie scattering and Raman emissions of spherical particles, we measured the Raman spectra together with the elastically scattered light of the excitation source of an evaporating aqueous sodium nitrate droplet. Resonance structures were observed in the temporal profiles of the elastically scattered light and Raman nitrate and water emissions. The resonance structures in these three profiles occurred in a concerted mode but sometimes occurred independently of each other. A model of inelastic scattering by microspheres by Kerker *et al.* ["Raman and Fluorescent Scattering by Molecules Embedded in Spheres with Radii up to Several Multiples of the Wavelength," Appl. Opt. **18,** 1172-1179 (1979); "Lorenz-Mie Scattering by Spheres: Some Newly Recognized Phenomena," Aerosol Sci. Technol. **1,** 275-291 (1982); "Inelastic Light Scattering," in *Aerosol Microphysics I: Particle Interaction,* W. H. Marlow, Ed. (Springer-Verlag, New York, 1980); "Model for Raman and Fluorescent Scattering by Molecules Embedded in Small Particles," Phys. Rev. A **13,** 396-404 (1976)] and the behavior of low order Mie resonances were used to explain the data. This type of data can be used for the determination of chemical compositions of spherical particles.

## I. Introduction

Spectroscopic techniques such as Raman spectroscopy can be used to determine the chemical composition of single suspended particles.[1] Raman spectroscopy of aerosol particles was first applied by analyzing microparticles on a substrate.[2] Recently, Raman spectroscopy has been applied to levitated single microparticles, using either the electrodynamic balance or optical levitation. Preston *et al.*[3] measured the Raman spectra of optically levitated dioctyl phthalate droplets. Thurn and Kiefer also used optical levitation to study Raman emissions of glass microspheres[4,5] and of water and glycerol droplets.[6] Using an electrodynamic balance, Fung and Tang[7–10] studied Raman emissions from droplets of aqueous solutions of various inorganic salts such as sulfates and nitrates. By using a high resolution monochromator, they observed fine spectral structures indicating phase transitions in supersaturated droplets and cation effects on the Raman spectra of anions (*e.g.*, sulfates and nitrates).

Although identification of the chemical nature of single suspended particles using Raman spectroscopy has been demonstrated, quantitative Raman analysis of spherical particles for chemical composition determination is complicated because of the coupling with Mie scattering. Benner *et al.*[11] observed structural resonances in the fluorescence spectra from dye impregnated polystyrene microspheres suspended in water. Resonance structures in Raman spectra of levitated spherical particles have also been reported. Thurn *et al.*[6] observed resonance structures superimposed on the broad spectrum seen in bulk sample spectra in the O-H stretching region of the Raman spectra of a 1:6 water-glycerol droplet mixture. They identified individual peaks of the measured

Raman spectrum as Mie resonance peaks. Preston *et al.*[3] reported similar resonance structures in the Raman spectra of the C-H stretching region of optically levitated dioctyl phthalate droplets. As the droplet evaporated due to heating from the Argon laser used as the excitation source and also that for optical levitation, the resonance peaks in the Raman spectra shifted systematically with time. Moreover, the observed resonance structures in the measured Raman spectra changed when different sizes of droplets were used.

The resonance peaks in inelastic spectra of spherical particles reported by the above mentioned researchers can be attributed to morphology dependent resonances that are strong functions of particle size and optical properties. Since a minute change in size that occurs during slow evaporation can result in large fluctuations in scattering intensity, this sensitivity of the scattered light intensity can be used to determine particle size to 1 part in $10^5$. The refractive index of the particle and the size parameter, which is the ratio of particle circumference to the optical wavelength of interest, determine the locations of these resonances. In Raman scattering, the wavelengths involved are the excitation laser wavelength and those of the Raman emissions. If any wavelength involved in the process corresponds to a resonant wavelength of the particle, the scattered intensity will be significantly affected by Mie resonances.

Raman emissions can be envisioned to occur as a result of a two step process. The first is the excitation of the Raman active molecules by absorption of photons of incident frequency. The second step is the release of photons at a shifted frequency when the excited molecules fall back to their ground states. The local emitted Raman intensity is proportional to the local excitation field

intensity. For a bulk sample, the local field strength is relatively uniform, or can be corrected for the Gaussian nature of the excitation laser beam when the dimension of the scattering volume is comparable to or larger than the beam waist of the laser beam. On the other hand, in the case of Mie scattering, the local excitation field intensity inside the particle is strongly dependent on the size and refractive index of the particle. Hence, Raman scattering from spherical particles can be complicated by Mie scattering in two ways. Since the internal excitation field drives the Raman emissions, one expects Raman emissions at all wavelengths to be enhanced when the incident excitation itself is at a Mie resonance. When the Raman shifted light corresponds to a resonant wavelength, the emission intensity at that particular wavelength will be selectively enhanced.

Understanding of the interactions of Mie scattering and Raman emissions is crucial to the application of quantitative Raman spectroscopy of spherical particles. Kerker and associates[12–15] have modeled inelastic scattering from microspheres, predicting the intensities of the elastically scattered light and the Raman emissions as a function of particle size and optical properties. Although resonance peaks in Raman spectra have been reported by various researchers,[3–8] systematic studies of resonance peaks in the elastically scattered light and Raman emissions as a function of the size parameter have not been presented. Such data are necessary for the validation of quantitative models of Raman scattering from microspheres and the ultimate application of this technique to quantitative analysis.

We present results of some experimental studies relating to the interactions of

resonances in the intensity profiles of the elastic and the Raman scattering of an evaporating aqueous sodium nitrate droplet. We first describe Kerker's model and present some of the key results for elastic and Raman scattering from microspheres. From these equations, the relationships between resonances in elastic and Raman spectra can be understood. Experimental measurements of the elastically scattered light and Raman emissions from an evaporating sodium nitrate droplet will then be reported.

## II. Inelastic Scattering of Microspheres:

Kerker and coworkers[12–15] developed a detailed model for inelastic scattering from microspheres. The microsphere is assumed to contain a Raman active molecule arbitrarily located at position $\vec{r}'$, and that the boundary of the particle only affects the local exciting field inside the particle and the emitted radiation but not the molecular transitions. The field inside the particle consists of two parts, the internal field due to the incident excitation of frequency $\omega_0$ and a secondary field of a different frequency $\omega$ that represents the Raman emissions. The Raman emission is classically viewed as generated by a dipole representing the Raman active molecule located at $\vec{r}'$, which undergoes forced oscillations at frequency $\omega$ induced by the local excitation field. The strength of the induced dipole, $\vec{p}$, on which the Raman field depends is described as the product of an effective polarizability $\alpha$ and the local excitation field. The secondary field of frequency $\omega$ in the particle is the sum of the induced dipole field and an internal field due to the medium of the microsphere which is postulated to account for the effects of the boundary of the particle. Outside the particle, there are two outgoing fields: one of frequency $\omega$ due to Raman scattering from

the particle; and another of frequency $\omega_o$ from the elastic scattering. Here, we present the key expressions for the elastic internal and external fields and inelastic external fields for Raman emissions. Using these equations, we will examine the relationship of resonances of elastic and Raman scattering from a spherical particle. This analysis is important to the interpretation of resonance peaks in the Raman spectra reported later in this paper.

In the following equations, the media inside and outside the particle are labeled 1 and 2, respectively, with magnetic permeabilities $\mu_1$ and $\mu_2$, wave numbers $k_1$ and $k_2$, and refractive indices $n_1$ and $n_2$. The particle radius is $a$. The local excitation electric field $\vec{E}(\vec{r})$ and magnetic field $\vec{B}(\vec{r})$ of frequency $\omega_o$ at location $\vec{r}$ inside the particle, which were also called the transmitted fields in Chew *et al.*,[15] may be written as a series of vector spherical harmonics:

$$\vec{E}_1(\vec{r}) = \sum_{l,m} \left\{ \left( ic/n_1^2\omega_o \right) \gamma_E(l,m) \nabla x \left( j_l(k_1 r) \vec{Y}_{llm}(\hat{r}) \right) + \gamma_M(l,m) j_l(k_1 r) \vec{Y}_{llm}(\hat{r}) \right\}, \tag{1}$$

$$\vec{B}_1(\vec{r}) = \sum_{l,m} \left\{ \gamma_E(l,m) j_l(k_1 r) \vec{Y}_{llm}(\hat{r}) - \left( ic/\omega_o \right) \gamma_M(l,m) \nabla x \left( j_l(k_1 r) \vec{Y}_{llm}(\hat{r}) \right) \right\}, \tag{2}$$

where $r = \| \vec{r} \|$ and $\hat{r} = \vec{r}/r$. The units and other notations are the same as in Jackson,[16] except for the vector spherical harmonics which follow Edmonds.[17] The internal field coefficients $\gamma_E(l,m)$ and $\gamma_M(l,m)$ are:

$$\gamma_E(l,m) = \frac{\left( in_1^2 \mu_1 / k_2 a \right) \alpha_E(l,m)}{n_1^2 \mu_2 j_l(k_1 a) \left\{ k_2 a h_l^{(1)}(k_2 a) \right\}' - n_2^2 \mu_1 h_l^{(1)}(k_2 a) \left\{ k_1 a j_l(k_1 a) \right\}'}, \tag{3}$$

$$\gamma_M(l,m) = \frac{-\left(i\mu_1/k_2 a\right)\alpha_M(l,m)}{\mu_2 h_l^{(1)}\left(k_2 a\right)\left\{k_1 a j_l\left(k_1 a\right)\right\}' - \mu_1 j_l\left(k_1 a\right)\left\{k_2 a h_l^{(1)}\left(k_2 a\right)\right\}'}, \tag{4}$$

where :

$j_l$ and $h_l^{(1)}$ denote spherical Bessel functions of order $l$, $\left\{xf(x)\right\}' \equiv \frac{d}{dx}\left\{xf(x)\right\}$, and $\alpha_E(l,m)$ and $\alpha_M(l,m)$ are the incident field coefficients, functions of $l$ and $m$ only.

Similarly, the external elastically scattered field outside the particle can be described as:

$$\vec{\mathrm{E}}_{\mathrm{sc}}(\vec{\mathrm{r}}) = \sum_{l,m}\left\{\left(ic/n_2^2\omega_{\mathrm{o}}\right)\beta_E(l,m)\nabla\mathrm{x}\left(h_l^{(1)}(k_2 r)\vec{\mathrm{Y}}_{llm}(\hat{r})\right) + \beta_M(l,m)h_l^{(1)}(k_2 r)\vec{\mathrm{Y}}_{llm}(\hat{r})\right\}, \tag{5}$$

$$\vec{\mathrm{B}}_{\mathrm{sc}}(\vec{\mathrm{r}}) = \sum_{l,m}\left\{\beta_E(l,m)h_l^{(1)}(k_2 r)\vec{\mathrm{Y}}_{llm}(\hat{r}) - \left(ic/\omega_{\mathrm{o}}\right)\beta_M(l,m)\nabla\mathrm{x}\left(h_l^{(1)}(k_2 r)\vec{\mathrm{Y}}_{llm}(\hat{r})\right)\right\}, \tag{6}$$

where the external elastically scattered field coefficients $\beta_E(l,m)$ and $\beta_M(l,m)$ are:

$$\beta_E(l,m) = \frac{\left\{n_2^2\mu_1 j_l\left(k_2 a\right)\left\{k_1 a j_l\left(k_1 a\right)\right\}' - n_1^2\mu_2 j_l\left(k_1 a\right)\left\{k_2 a j_l\left(k_2 a\right)\right\}'\right\}\alpha_E(l,m)}{n_1^2\mu_2 j_l\left(k_1 a\right)\left\{k_2 a h_l^{(1)}\left(k_2 a\right)\right\}' - n_2^2\mu_1 h_l^{(1)}\left(k_2 a\right)\left\{k_1 a j_l\left(k_1 a\right)\right\}'}, \tag{7}$$

$$\beta_M(l,m) = \frac{\left\{\mu_1 j_l(k_1 a)\left\{k_2 a j_l(k_2 a)\right\}' - \mu_2 j_l(k_2 a)\left\{k_1 a j_l(k_1 a)\right\}'\right\}\alpha_M(l,m)}{\mu_2 h_l^{(1)}(k_2 a)\left\{k_1 a j_l(k_1 a)\right\}' - \mu_1 j_l(k_1 a)\left\{k_2 a h_l^{(1)}(k_2 a)\right\}'} . \tag{8}$$

Note that the $k_1 a$ and $k_2 a$ terms in the $\gamma$ and $\beta$ refer to light of frequency $\omega_o$, the incident light frequency. The poles of the $\gamma$ and $\beta$ determine the conditions for resonances. Since the coefficients $\alpha_E$ and $\beta_E$, $\alpha_M$ and $\beta_M$ have the same denominators, both the internal and external fields will exhibit resonance when $\omega_o$ is coincident with a resonance frequency of the particle . In a similar fashion, the Raman field at frequency $\omega$ outside the particle can also be written as :

$$\vec{E}_2(\vec{r}) = \sum_{l,m}\left\{\left(ic/n_2^2\omega\right)c_E(l,m)\nabla x\left(h_l^{(1)}(k_2 r)\vec{Y}_{llm}(\hat{r})\right) + c_M(l,m)h_l^{(1)}(k_2 r)\vec{Y}_{llm}(\hat{r})\right\} , \tag{9}$$

$$\vec{B}_2(\vec{r}) = \sum_{l,m}\left\{c_E(l,m)h_l^{(1)}(k_2 r)\vec{Y}_{llm}(\hat{r}) - \left(ic/\omega\right)c_M(l,m)\nabla x\left(h_l^{(1)}(k_2 r)\vec{Y}_{llm}(\hat{r})\right)\right\} , \tag{10}$$

where the Raman outgoing field coefficients $c_E(l,m)$ and $c_M(l,m)$ are:

$$c_E(l,m) = \frac{\left(in_2^2\mu_2/k_1 a\right)a_E(l,m)}{n_1^2\mu_2 j_l(k_1 a)\left\{k_2 a h_l^{(1)}(k_2 a)\right\}' - n_2^2\mu_1 h_l^{(1)}(k_2 a)\left\{k_1 a j_l(k_1 a)\right\}'} , \tag{11}$$

$$c_M(l,m) = \frac{-\left(i\mu_2/k_1 a\right)a_M(l,m)}{\mu_2 h_l^{(1)}\left(k_2 a\right)\left\{k_1 a j_l\left(k_1 a\right)\right\}' - \mu_1 j_l\left(k_1 a\right)\left\{k_2 a h_l^{(1)}\left(k_2 a\right)\right\}'} . \tag{12}$$

It should be noted that some of the field coefficients listed above are not identically the same as those in Chew *et al.*[15] We have substituted the dielectric constant, $\epsilon$, which was used in their original equations with $\mu$ and $n$, using:

$$n_1^2 = \mu_1\epsilon_1 \quad \text{and} \quad n_2^2 = \mu_2\epsilon_2 , \tag{13}$$

so that the field coefficients can be compared more clearly.

The coefficients $a_E$ and $a_M$ in Eqs. (11) and (12), respectively, are the dipole field coefficients referring to a specific dipole representing a Raman active molecule localized at $\vec{r}'$. However, they are proportional to the dipole moment $\vec{p}$ which can be described by the product of an effective polarizability $\alpha$ and the local transmitted field, $\vec{E}_1(\vec{r}')$ of frequency $\omega_0$. Hence $c_E$ and $c_M$ are both proportional to $\vec{E}_1(\vec{r}')$. If $\omega_0$ corresponds to a resonance frequency for $\vec{E}_1(\vec{r}')$, the Raman scattering field will also be at resonance, regardless of the frequency $\omega$ at which the Raman emissions occur. Therefore, one can expect that resonances in the entire Raman spectrum at all $\omega$'s and in the elastic scattering occur simultaneously. More precisely, resonance in the elastic scattering is a necessary and sufficient condition for simultaneous resonances of Raman emissions at all frequencies.

Notice that the $\gamma_E$ and $c_E$ (and similarly $\gamma_M$ and $c_M$) have the same form of

denominator, although the argument in the former refers to the incident excitation frequency $\omega_0$ while that of the latter refers to the Raman emission frequency $\omega$. Since $\gamma_E$ and $c_E$ have the same form of denominator, one can see that resonance in the Raman scattering field can occur in a similar fashion as in elastic scattering. When $\omega$ corresponds to a resonant frequency, resonance occurs and the Raman emission at this particular frequency will be selectively enhanced. Therefore, one can expect resonances in a Raman spectrum to occur at selected wavelengths independent of each other as have been observed in broad-band Raman spectra of droplets[3,7,8] and glass microspheres.[4–6]

## III. Evaporation of An Aqueous $NaNO_3$ Droplet Levitated in An Electrodynamic Balance

A conventional bihyperboloidal electrodynamic balance was used to trap and levitate a droplet stationary for the Raman experiment. Details of the apparatus which is illustrated in Fig. 1 have been reported elsewhere.[18] A droplet of sodium nitrate solution was charged and introduced into the balance. After it was dried at vacuum, water vapor from a thermostated water reservoir was introduced and the droplet equilibrated to a constant size. Then, as the pressure in the balance was slowly reduced, the droplet evaporated and the elastically scattered light exhibited several resonance peaks during this size change. Both the Raman spectra and the elastically scattered light were recorded as a function of time.

To illustrate the two types of resonances described above, the solution studied should contain at least one Raman active component, preferably two, so that

the scattering intensities for different Raman shifts can be compared. The Raman spectrum of a sodium nitrate solution exhibited a nitrate peak at about 1040 $cm^{-1}$ and a broad water peak at about 3200 to 4000 $cm^{-1}$. Another advantage of using a sodium nitrate droplet is that one can control the rate of evaporation easily. The rate of evacuation was manually adjusted using a needle valve so that appreciable change in the intensity of the elastically scattered light could be observed. The original size of the droplet was about 20 $\mu$m in diameter. The evaporation of water caused about a 12% reduction in weight, *i.e.,* a 4% reduction in particle size.

## IV. Elastic and Raman Scattering Intensity Profiles of An Evaporating $NaNO_3$ Droplet

Figure 2 shows the apparatus used to measure the Raman scattering from single particles. A Spectra Physics 2020 Argon ion laser at 488.0nm was used as the excitation source. It was operated at a nominal power of about 0.5W. The laser beam was focused on the particle by a lens with focal length 125cm. The spectra of 90° scattered light, containing the scattered laser light and the Raman nitrate and water peaks, were recorded by a Princeton Instrument IRY 700 optical multichannel analyzer (OMA). The OMA was operated at 20 °C with the photocathode cooled to about -25 °C by flowing chilled methanol. It was attached to a SPEX 340E monochromator with a dispersion of 10 nm/mm using a 300 gr/mm grating which has a spectral range sufficient to cover the laser scattered light and the Raman nitrate and water peaks. The OMA was controlled by a Princeton Instrument ST120 controller which was interfaced to an AT compatible computer. The measured Raman spectra were automatically

stored in a hard disk via direct memory access.

Since the laser scattered light was orders of magnitude more intense than the Raman signal, a series of long pass filters were employed to attenuate the intensity of the elastically scattered light until the laser light and the Raman signal fell into the same dynamic range of the OMA. By multiplexing the spectra using the OMA, the laser scattered light and the Raman emissions from the particle were monitored simultaneously in real time as the droplet evaporated. Because the dielectric filter used was very sensitive to optical alignments, light scattered from the particle was collimated by a *f/3* lens before passing through the filters. After the filters, it was focused on the slit of the monochromator by a *f/5.9* lens which matches the *f* number of the monochromator. To shorten the integration time of each Raman measurement, the slit of the monochromator was adjusted to 200$\mu$m. Beyond this value, the peak of the laser light only broadened without increasing its peak value. This slit width limits the spectral resolution to 14 - 19 $cm^{-1}$. The integration time employed was approximately 1.6 sec.

Figure 3 shows a typical scattering spectrum of a sodium nitrate droplet measured by the OMA. The peak at 0 $cm^{-1}$ is the elastically scattered Argon laser light which has been attenuated by a factor of $10^4$. The peaks at about 1040 and 1400 $cm^{-1}$ are the nitrate peaks. The strong 1040 $cm^{-1}$ peak was taken as the representative of the nitrate emissions. The minor peak at about 2100 $cm^{-1}$ was due to room light at 546.07 nm leaking into the optical detection system. Since water is broadbanded from 3200 to 3800 $cm^{-1}$, it is important to choose a representative wavenumber for the Raman emissions. Three intensity

profiles, located at 3308, 3449, and 3587 $cm^{-1}$ were examined. These correspond to the measured intensities at the half maximum on the left, at the maximum and at the half maximum on the right, as illustrated in Figure 3, respectively. Figure 4 shows the time dependence of the intensities at these three wavenumbers in the broadband water peak. Although the water peak shown in Figure 3 appears to exhibit resonances at various wavenumbers, it is clear from Figure 4 that any one of the three wavenumbers can be used to represent the Raman water peak in the intensity profile.

To study the resonance structures in elastic and inelastic scattering of the evaporating droplet, the time variation of peak counts of the Argon laser line at 0 $cm^{-1}$, the Raman nitrate peak at 1040 $cm^{-1}$, and the Raman water peak at 3449 $cm^{-1}$ are shown in Figure 5. Resonance structures in the Argon line, the Raman nitrate and water emissions exhibit behaviors that can be grouped in three different time regions: (1) 0 to 400 sec, (2) 400 to 1200 sec, and (3) 1200 to 1650 sec. To facilitate the explanation of different observations in these three regions, we will analyze the results of each region separately.

**(1) 0 to 400 sec**

There are three distinct major peaks in the elastic spectrum and the Raman nitrate spectrum as shown in Figure 6. The water intensity profile also exhibits resonance structures at the same time albeit to a lesser extent. Since the elastically scattered light and the Raman emissions of both the nitrate and water exhibit resonances simultaneously, these resonances can be attributed to the resonance of the Argon laser line itself.

**(2) 400 to 1200 sec**

The Raman intensity profiles of the nitrate and water peaks from 400 to 1200 seconds are shown in Figure 7. One can clearly observe that the nitrate and the water profiles have exactly the same structures. Also, the peaks here are much sharper than those three appearing in Figure 6. Simultaneous appearance of resonances of the nitrate and water Raman peak should be due to the internal resonance of the elastic scattered light. However, the resonance of the elastically scattered Argon laser light appeared at locations different from those of the Raman emissions. To illustrate this with a better resolution, Figure 8 shows the elastically scattered Argon light intensity profile and the Raman nitrate intensity profile only between 400 to 800 seconds. It is clear that resonances of the two intensity profiles occur at totally different locations, which seems to contradict the above criterion for concurrent appearance of the Raman nitrate and water resonances. We explain this observation with the nature of low order resonance peaks later.

**(3) 1200 to 1650 sec**

There are two distinct resonance peaks in the elastic spectrum but the corresponding peaks in the Raman emissions are much weaker as depicted in Figure 9. On the other hand, there are several small peaks in the nitrate spectrum occurring at about 1350 sec to 1475 sec. They may be due to selective resonance of the nitrate peak when the nitrate wavelength corresponds to a resonant wavelength of the droplet at a particular size.

Efforts to use Raman spectroscopy to follow chemical reactions within aerosol

particles depend on the relative intensities of different Raman lines and the elastically scattered light. It is therefore interesting to examine the Raman nitrate intensity and the Raman water intensity as a function of the Argon scattered intensity at various times. Figure 10a shows that the Raman nitrate vs Argon line plot exhibits a "$L$" shaped curve. Figures 10 b - d show the contributions of data from regions (1) 0 to 400 sec, (2) 400 to 1200 sec and (3) 1200 sec to 1650 sec. The three temporal regions in the above analysis contribute to different regions of the "$L$" shape plot. Figures 11 a - d show similar plots for water intensity vs Argon line intensity. Figure 12 depicts the nitrate peak intensity as a function of the water peak intensity. In light of observations in Figure 10 or Figure 11 individually, it might be somewhat surprising to see that all the data points collapse into a rather linear zone as shown in Figure 12. However, our analysis revealed that most of the resonance structures observed in this experiment were the result of resonance of the incident excitation light which caused enhancements of both the nitrate and water peaks to a similar extent. Therefore, a more or less linear relationship between the nitrate and the water peak intensities can be expected. The location of this zone might give information regarding the concentration of the droplet (mole ratio of nitrate to water), albeit with a limited precision.

As emphasized in Figures 7 and 8, we observed simultaneous resonance of the nitrate peak and the water peak without that occurring in the measured elastic intensity profile. This seems to contradict what we concluded earlier. Related phenomena have been reported by Qian and Chang.[19] They found a much higher density of resonance peaks than normally observed in elastic spectra in multiple order Stokes emission in stimulated Raman emissions from $CCl_4$

microspheres. Hill and Benner[20,21] explained this observation by the characteristics of low order resonance peaks in Mie scattering. We believe that our observation reported in this paper can also be explained in a similar manner.

## V. Low Order Resonance Structures in Mie Scattering

Using equations (7) and (8), when the denominator of the $\beta$'s ( or the $\gamma$'s) becomes zero, the field will exhibit resonance structures. Each resonance peak can be assigned with a mode number and an order number. The mode number indicates the number of maxima between 0 and 180 degrees in the phase function, the angular distribution of energy of the mode. The order number indicates the number of maxima in the radial dependence of the mode. Mathematically a resonance mode number represents the collection of poles of the $\beta$'s (or the $\gamma$'s) of a particular $l$. At each $l$, there is a series of poles for the $\beta$'s. Each pole of any particular $l$ is given an order number. The lower the order number, the sharper the resonance peak and also the more localized the energy in the particle is distributed near the surface. The sharpness of a resonance can be represented by $Q$, which is defined as the ratio of the resonant size parameter, $X_r$, and the full width at half maximum ($\Delta X_{1/2}$) of a resonance peak. The lower the order of a resonance peak is, the smaller the $\Delta X_{1/2}$ is and the higher its $Q$ is.

Recall that the Raman scattering coefficients, $c_M$ and $c_E$, are proportional to the internal local excitation field strength, which is linear in $\gamma_E$ and $\gamma_M$, the internal field coefficients at $\omega_0$. On the other hand, the external elastically

scattered field coefficients are $\beta_E$ and $\beta_M$. One should note that the signal registered by an OMA in an experiment was actually a time integrated intensity. In our evaporation experiment, the time in the intensity profiles can actually be replaced by the size parameter $X$. Therefore, for the case of a resonance peak, we are actually measuring the area of the peak which can be approximated by the product of peak intensity and $\Delta X_{1/2}$. Resonance structures with $Q > 10^5$ are not generally observed in elastic spectra because the external field coefficients $\beta_E$ and $\beta_M$ are only an order of unity even at resonance. Hence the integrated area under a low order resonance peak in the elastic spectra approaches zero as $Q$ becomes very large (*i.e.*, $\Delta X_{1/2} \mid \beta_E \mid^2$ and $\Delta X_{1/2} \mid \beta_M \mid^2$ go to zero). On the other hand, the internal field coefficients $\gamma_E$ and $\gamma_M$ can increase as $Q$ becomes large so that the product $\Delta X_{1/2} \mid \gamma_E \mid^2$ and $\Delta X_{1/2} \mid \gamma_M \mid^2$ can increase slowly to an order of about unity. This is basically due to the difference in the numerators of the $\beta$'s and the $\gamma$'s. Physically most of the energy in a high $Q$ or high quality resonance is confined within a particle instead of leaking out as scattered light. Therefore, Raman enhancements due to low order internal resonance of the excitation field can occur without resonance in the elastic spectra being measured. This explains why the nitrate and water resonances occurred simultaneously while resonance in the elastic spectra was not measured. The sharpness of the peaks in Figure 7 also supports this argument since they are much narrower than those observed in Figure 6, where both the nitrate peak and the elastically scattered light exhibit resonances.

## VI. Conclusions

By measuring simultaneously the elastically scattered light and the Raman emissions from an evaporating aqueous sodium nitrate droplet as a function of time, one can study the interactions of Mie scattering with Raman emissions for spherical particles. We found that resonances of the elastically scattered light, Raman nitrate peak and Raman water peak can occur in a concerted mode and can also occur independent of each other. These observations can be explained by Kerker's[13–15] model of inelastic scattering from microspheres and the behavior of low order resonance structures in Mie scattering. This type of measurement can be potentially used to test the validity of existing models of Raman emissions from microspheres. One application of this type of data would be quantitative determination of the chemical compositions of spherical particles. One could use the elastic spectra to obtain the refractive index and particle size of the droplet, and then use accurate models of Raman emissions from spherical particles with the known particle size and refractive index to determine the chemical composition of the particle.

## VII. Acknowledgment

This research was supported by the Caltech Consortium in Chemistry and Chemical Engineering; founding members: E. I. du Pont de Nemours and Company, Inc., Eastman Kodak Company, Minnesota Mining and Manufacturing Company, and Shell Development Company.

References

1. S. Arnold, "Spectroscopy of Single Levitated Micron Sized Particles," in P. W. Barber and R. K. Chang Ed., Optical Effects Associated with Small Particles (World Scientific Publishing Co., Singapore, 1988).

2. G. J. Rosasco, E. S. Etz, and W. A. Cassatt, "The Analysis of Discrete Fine Particles by Raman Spectroscopy," Applied Spectroscopy, **29 (5)**, 396 - 404 (1975).

3. R. E. Preston, T. R. Lettieri, and H. G. Semerjian, "Characterization of Single Levitated Droplets by Raman Spectroscopy," Langmuir, **1**, 365 - 367 (1985).

4. R. Thurn and W. Kiefer, "Observations of Structural Resonances in the Raman Spectra of Optically Levitated Dielectric Microspheres," J. of Raman Spectroscopy, **15 (6)**, 411-413 (1984).

5. R. Thurn and W. Kiefer, "Raman-Microsampling Technique Applying Optical Levitation by Radiation Pressure," Applied Spectroscopy, **38 (1)**, 78 - 83 (1984).

6. R. Thurn and W. Kiefer, "Structural Resonances Observed in the Raman Spectra of Optically Levitated Liquid Droplets," Applied Optics, **24 (10)**, 1515 -1519 (1985).

7. K. H. Fung and I. N. Tang, "Raman Scattering from Single Solution Droplets," Applied Optics, **27 (2)**, 206 -208 (1988).

8. K. H. Fung and I. N. Tang, "Raman Spectra of Singly Suspended Supersaturated Ammonium Bisulfate Droplets," Chemical Physics Letter, **147 (5)**, 509 - 513 (1988).

9. K. H. Fung and I. N. Tang, "Composition Analysis of Suspended

Aerosol Particles by Raman Spectroscopy : Sulfates and Nitrates," J. Coll. and Inter. Sci., **130 (1)**, 219 - 224 (1989).

10. I. N. Tang and K. H. Fung, "Characterization of Inorganic Salt Particles by Raman Spectroscopy," J. of Aerosol Sci., **20 (5)**, 609 -617 (1989).
11. R. E. Benner, P. W. Barber, J. F. Owen, and R. K. Chang, "Observation of Structure Resonances in the Fluorescence Spectra from Microspheres," Physical Review Letters, **44 (7)**, 475 - 478 (1980).
12. M. Kerker and S. D. Druger, "Raman and Fluorescent Scattering by Molecules Embedded in Spheres with Radii up to Several Multiples of the Wavelength," Applied Optics, **18 (8)**, 1172 - 1179 (1979).
13. M. Kerker, "Lorenz-Mie Scattering by Spheres : Some Newly Recognized Phenomena," Aerosl Sci. & Tech., 1 275 - 291 (1982).
14. P. J. McNulty, H. W. Chew and M. Kerker, "Inelastic Light Scattering," in W. H. Marlow, Ed., Aerosol Microphysics I: Particle Interaction (Springer - Verlag, Berlin, 1980)
15. H. Chew, P. J. McNulty, and M. Kerker, "Model for Raman and Fluorescent Scattering by Molecules Embedded in Small Particles," Physical Review A, **13 (1)**, 396 - 404 (1976).
16. J. D. Jackson, Classical Electrodynamics (Wiley, New York, 1962)
17. A. R. Edmonds, Angular Momentum in Quantum Mechanics (Princeton U. Press, Princeton, N. J., 1957).
18. G. Sageev, R. C. Flagan, J. H. Seinfeld and S. Arnold, "Condensation Rate of Water on Aqueous Droplets in the Transition Regime," J. of Coll. & Interf. Sci., **113(2)**, 421 - 429, 1986.
19. S.-X. Qian and R. K. Chang, "Multi-order Stokes Emissions from

Micrometer Sized Droplets," Phys. Rev. Lett., **56**, 926 (1986).

20. S. C. Hill and R. E. Benner, "Morphology-dependent Resonances Associated with Stimulated Processes in Microspheres," J. Opt. Soc. Am. B., **3 (11)**, 1509 -1514 (1986).

21. S. C. Hill and R. E. Benner, "Morphology-dependent Resonances," in P. W. Barber and R. K. Chang Ed., Optical Effects Associated with Small Particles (World Scientific Publishing Co., Singapore, 1988).

**List of Figure Captions**

Figure 1: Electrodynamic balance

Figure 2: Raman spectroscopy of single particles using an OMA

Figure 3: An example of Raman spectrum of an aqueous sodium nitrate droplet measured by an OMA

Figure 4: Raman water intensity profiles at 3308 $cm^{-1}$, 3449 $cm^{-1}$, and 3587 $cm^{-1}$

Figure 5: Intensity profiles of the elastically scattered Argon line and Raman emissions of the nitrate and the water peaks of an evaporating sodium nitrate droplet

Figure 6: Scattering intensity profiles from 0 to 400 seconds

Figure 7: Scattering intensity profiles of nitrate and water peaks from 400 to 1200 seconds

Figure 8: Scattering intensity profiles of Argon line and nitrate peaks from 400 to 800 seconds

Figure 9: Scattering intensity profiles from 1200 to 1650 seconds

Figure 10: Raman nitrate scattering intensity as a function of scattered Argon line intensity

Figure 11: Raman water scattering intensity as a function of scattered Argon line intensity

Figure 12: Raman nitrate intensity as a function of Raman water scattering intensity

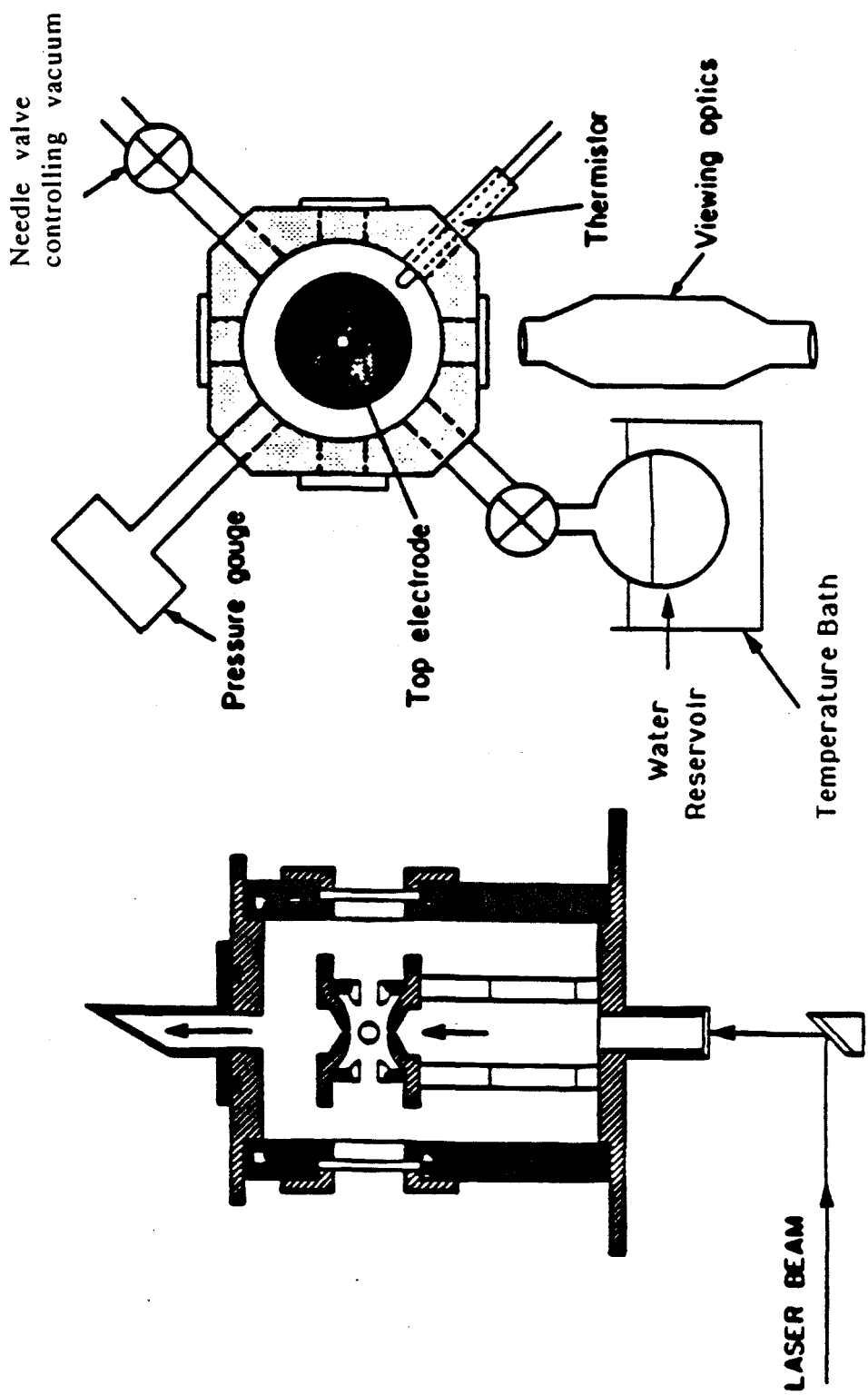


Figure 1: Electrodynamic balance

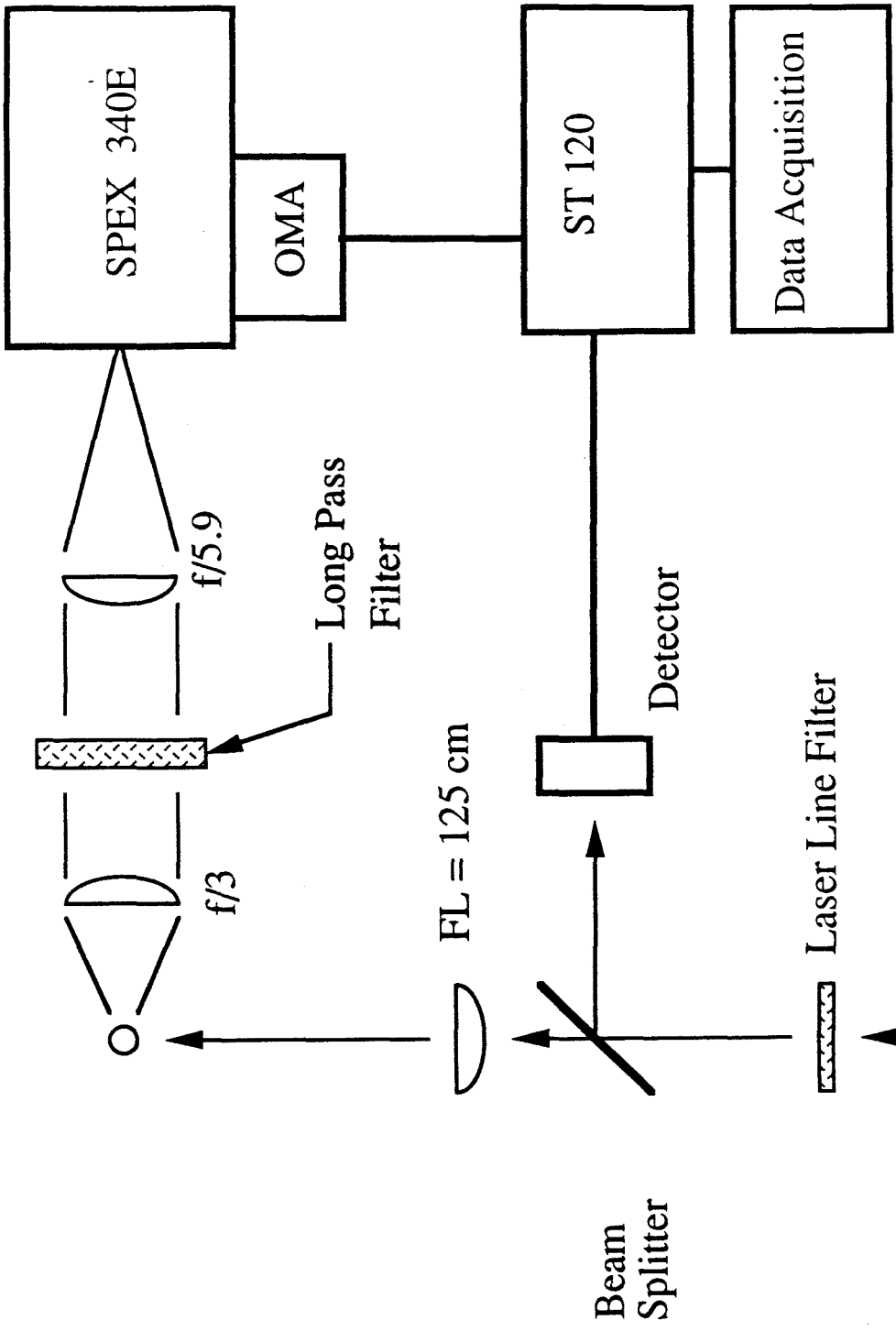


Figure 2 : Raman spectroscopy of single particles using an OMA

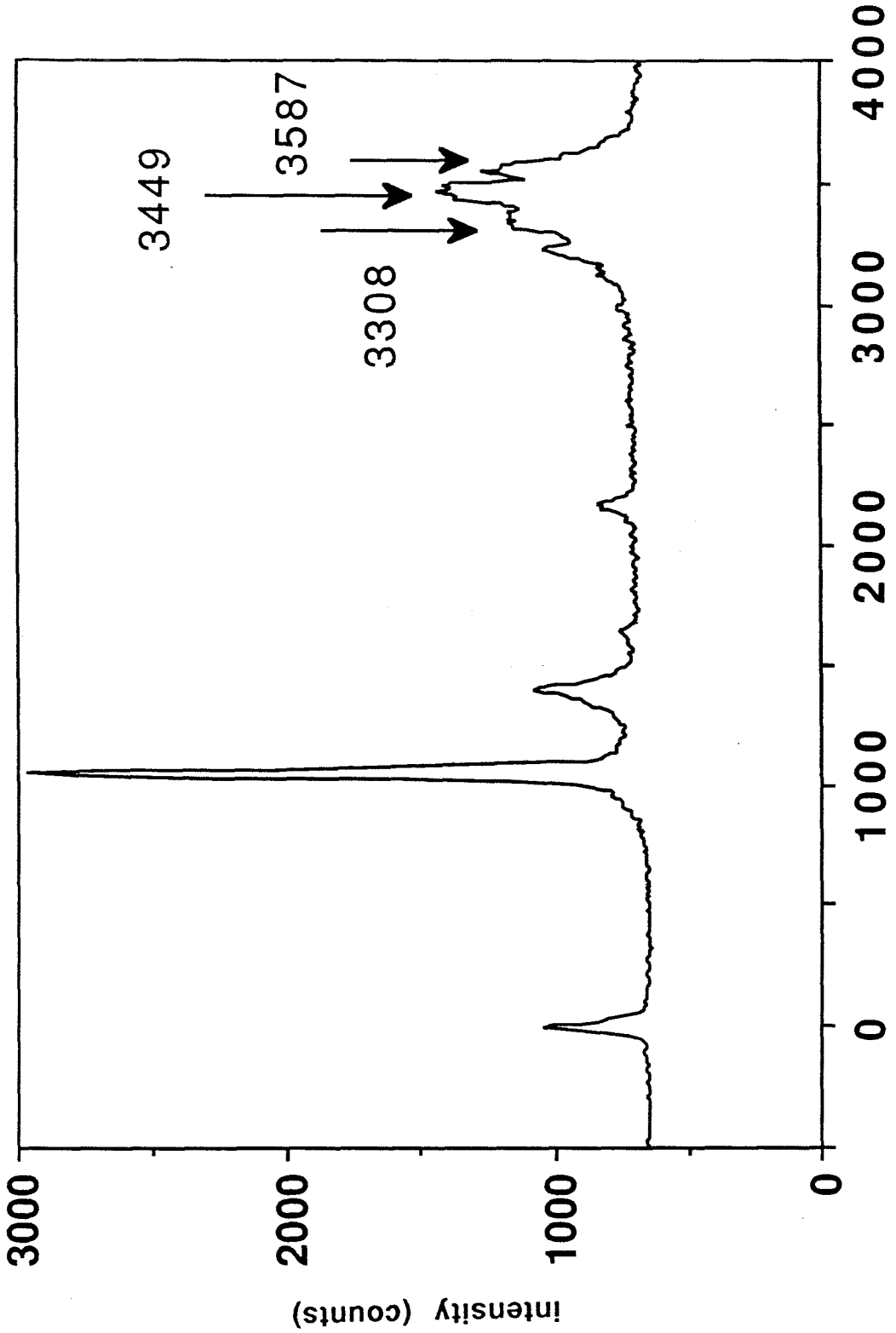


Figure 3: An example of Raman spectrum of an aqueous sodium nitrate droplet measured by an OMA.

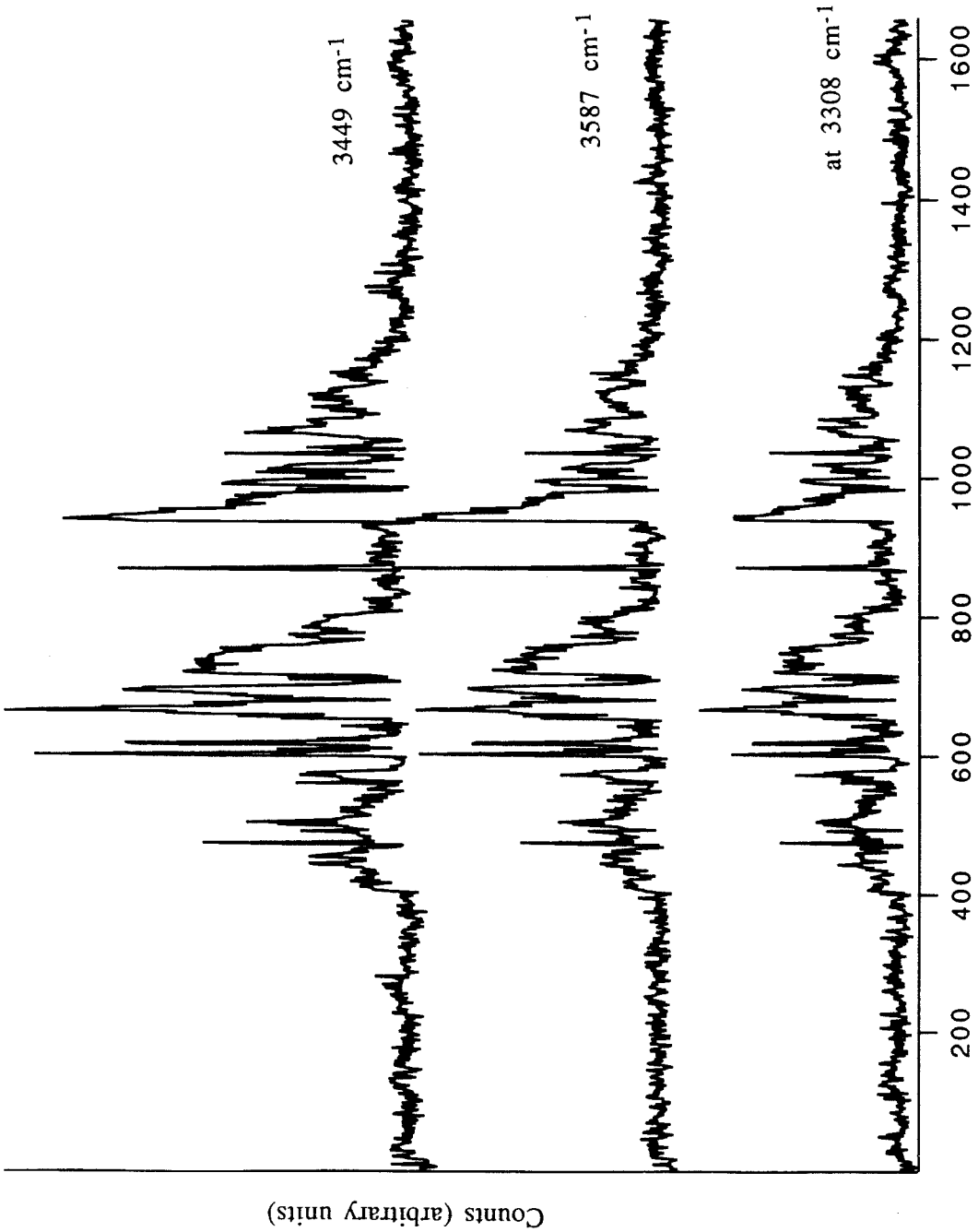


Figure 4 : Raman water intensity profiles at 3308 $cm^{-1}$, 3449 $cm^{-1}$, and 3587 $cm^{-1}$

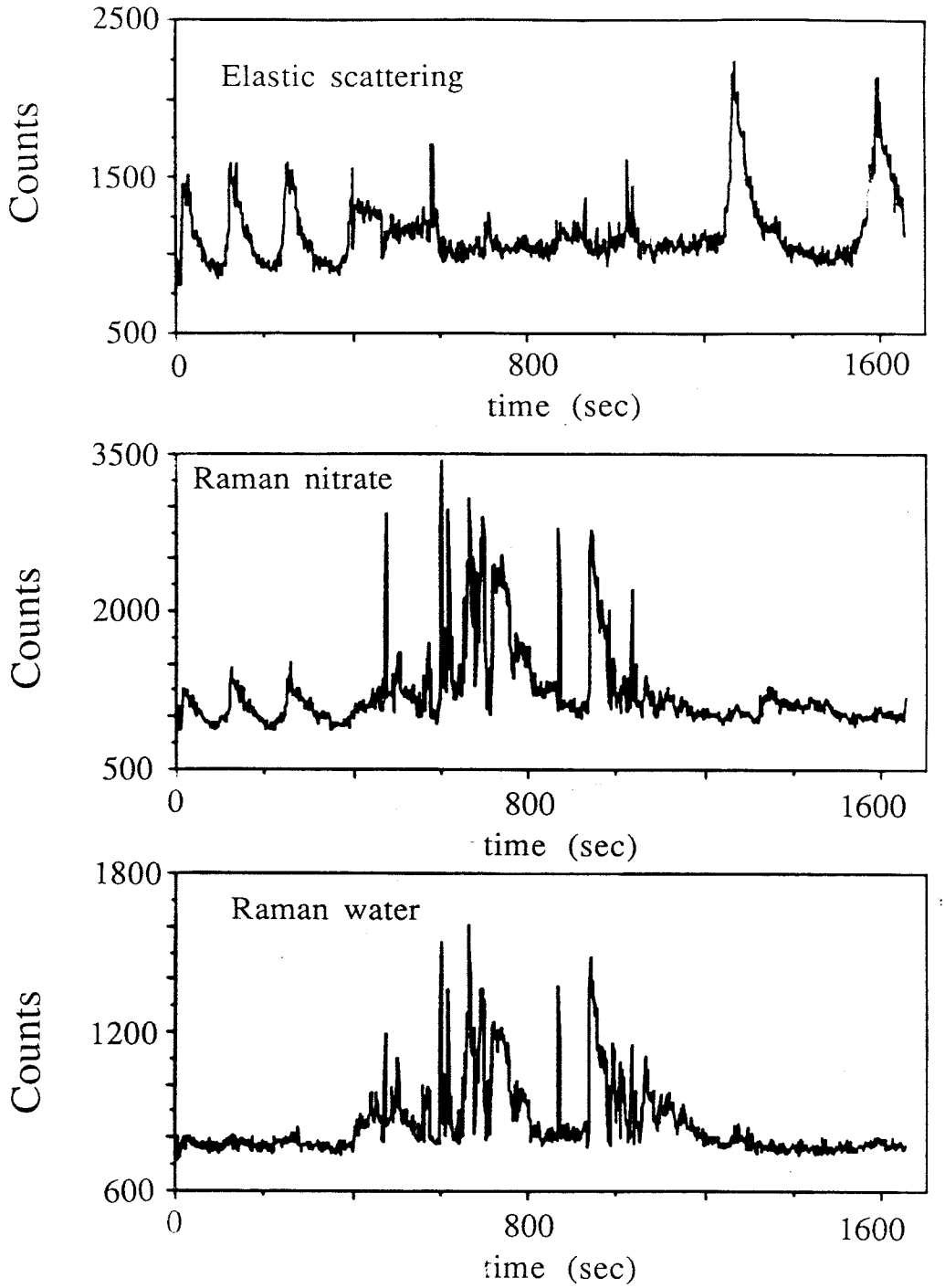


Figure 5 : Intensity profiles of the elastically scattered Argon line and Raman emissions of the nitrate and the water peaks of an evaporating sodium nitrate droplet

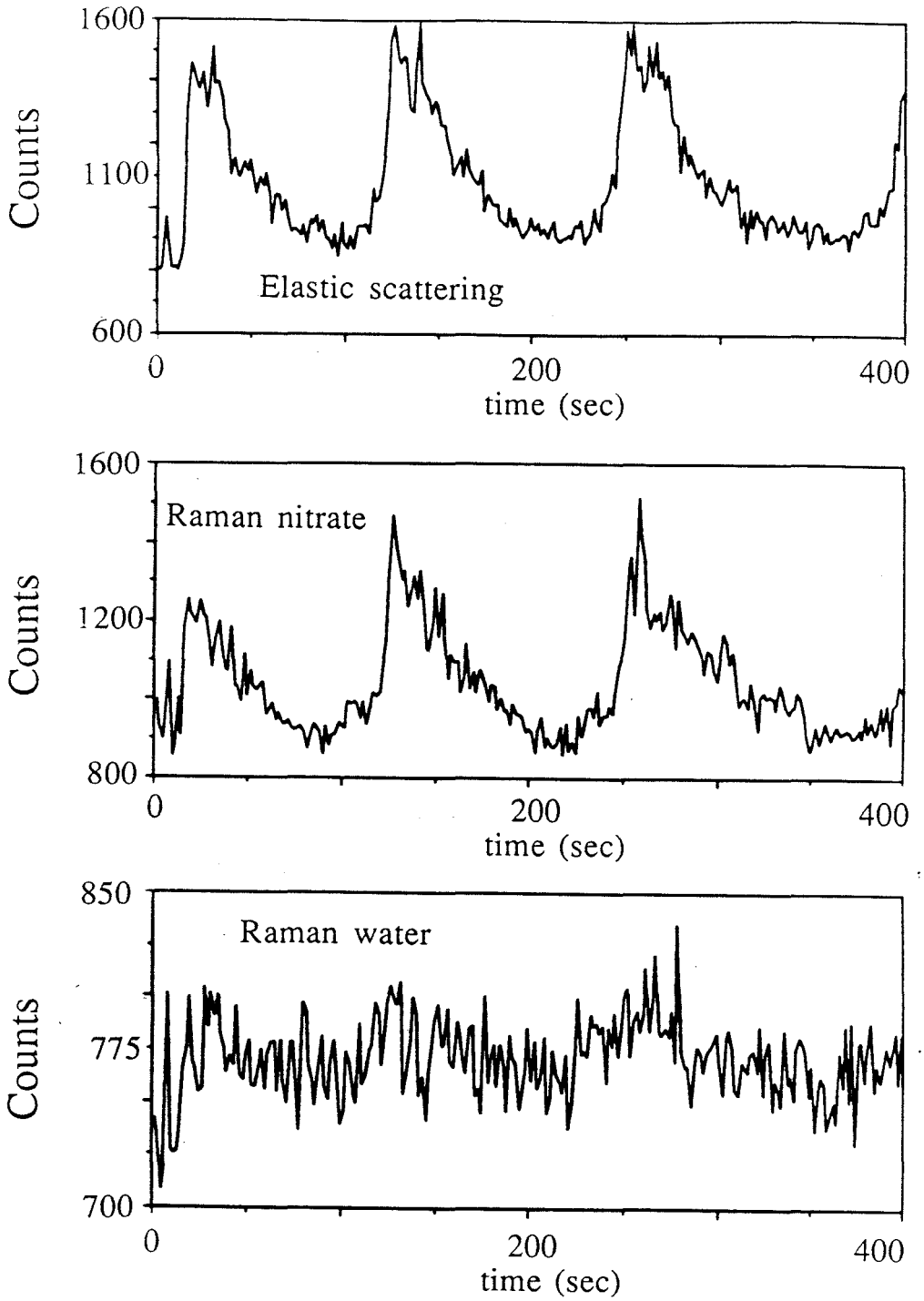


**Figure 6 : Scattering intensity profiles from 0 to 400 seconds**

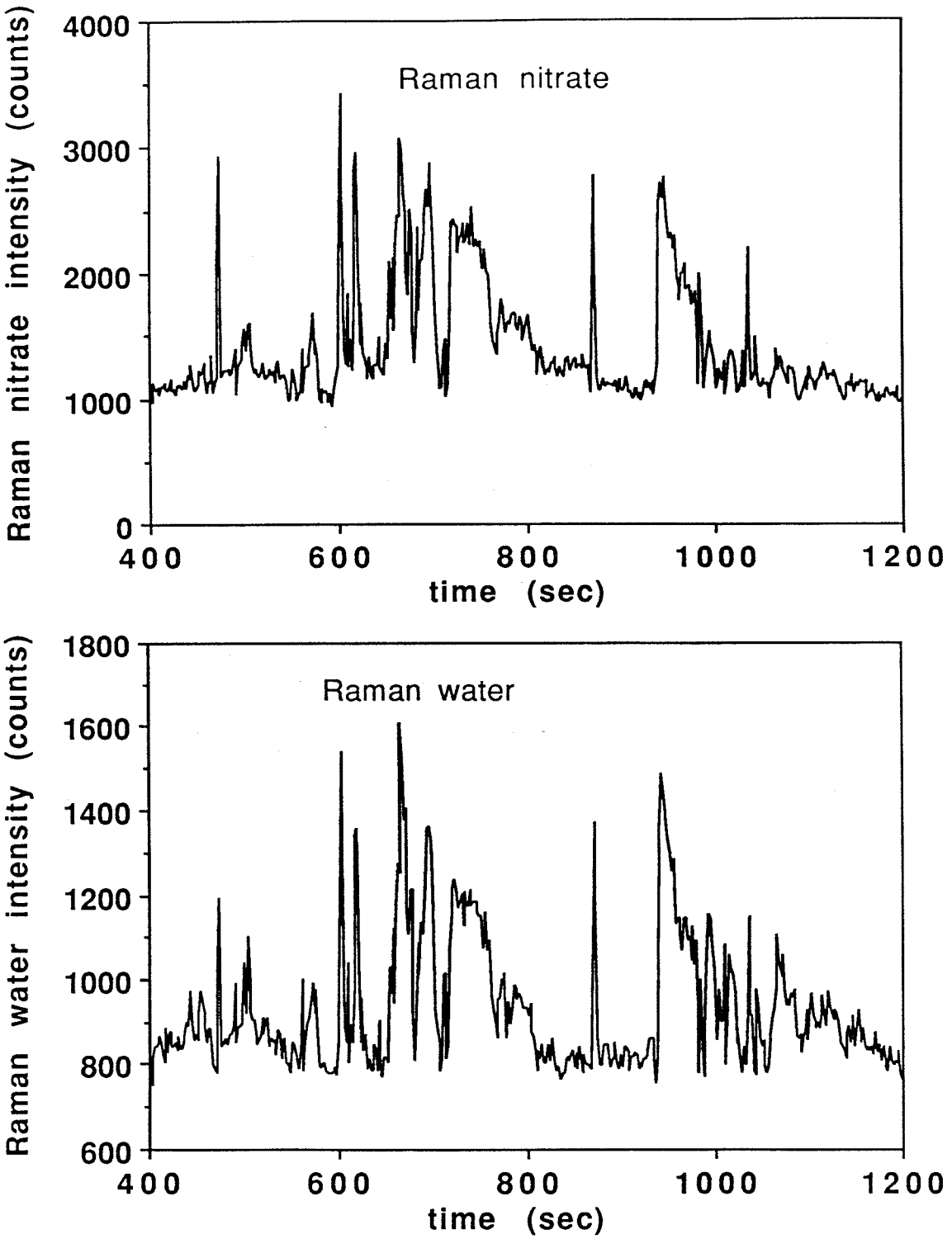


Figure 7 : Scattering intensity profiles of nitrate and water peaks from 400 to 1200 seconds

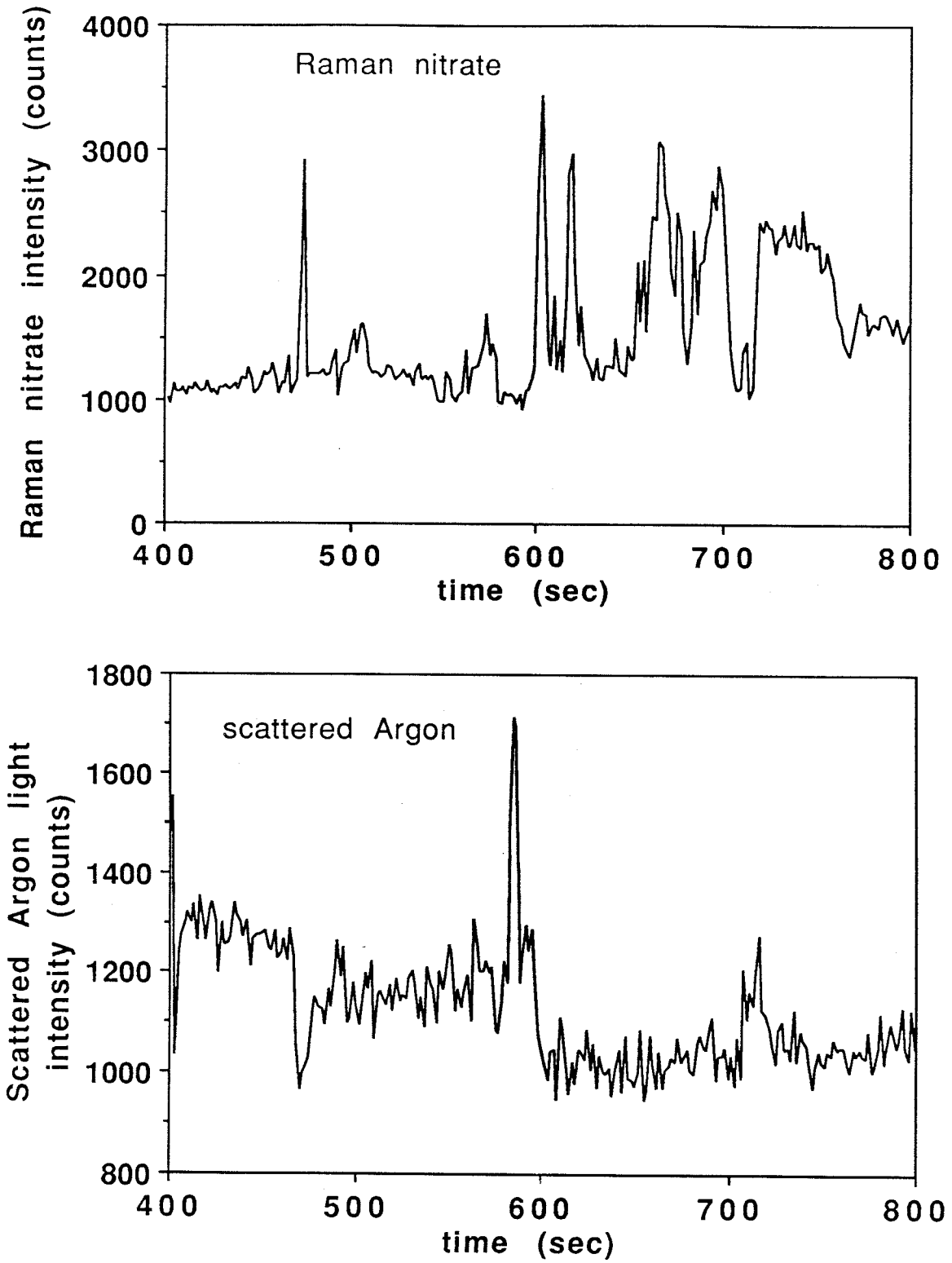


Figure 8 : Scattering intensity profiles of Argon line and nitrate peaks from 400 to 800 seconds

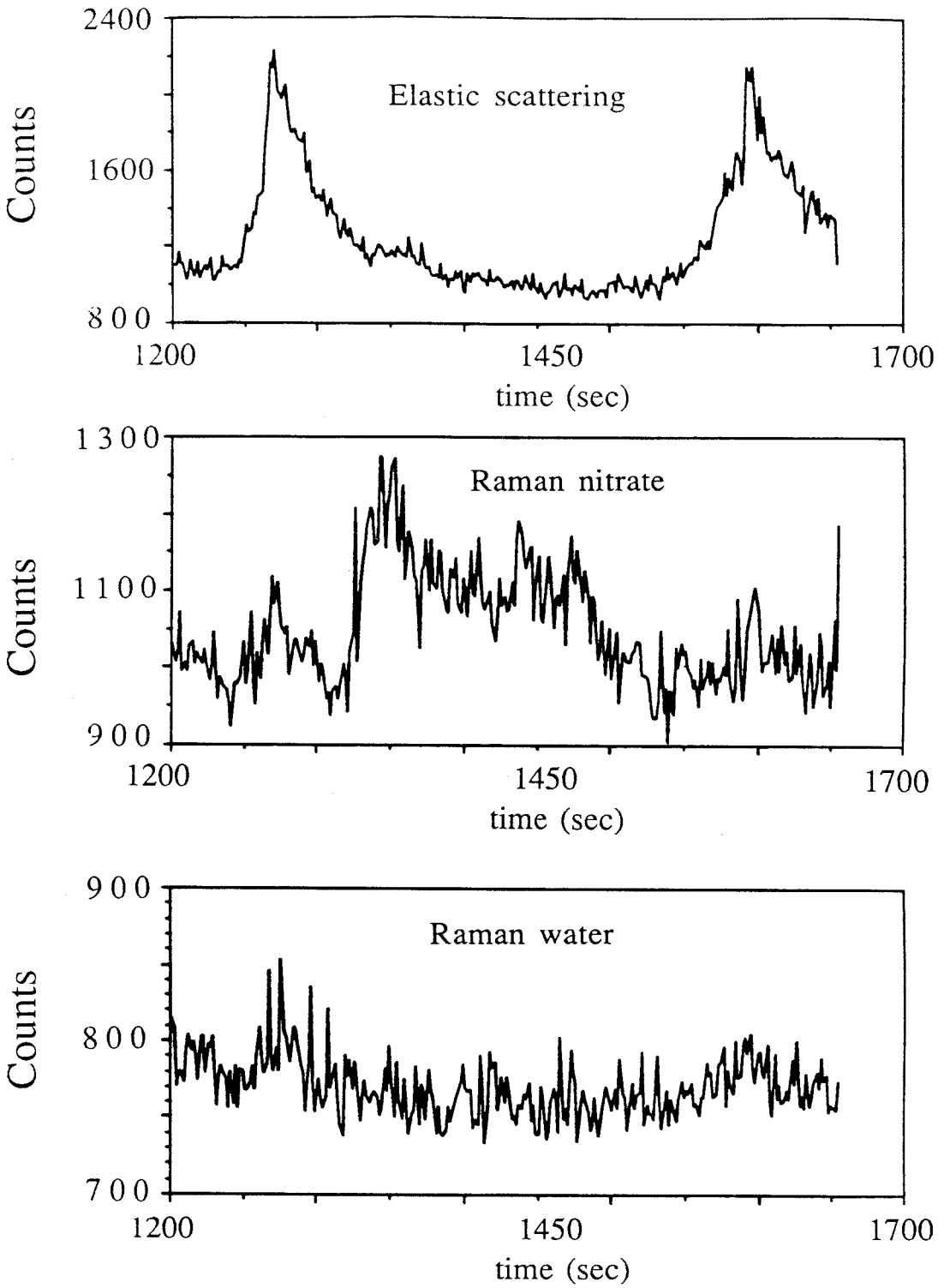


Figure 9 : Scattering intensity profiles from 1200 to 1650 seconds

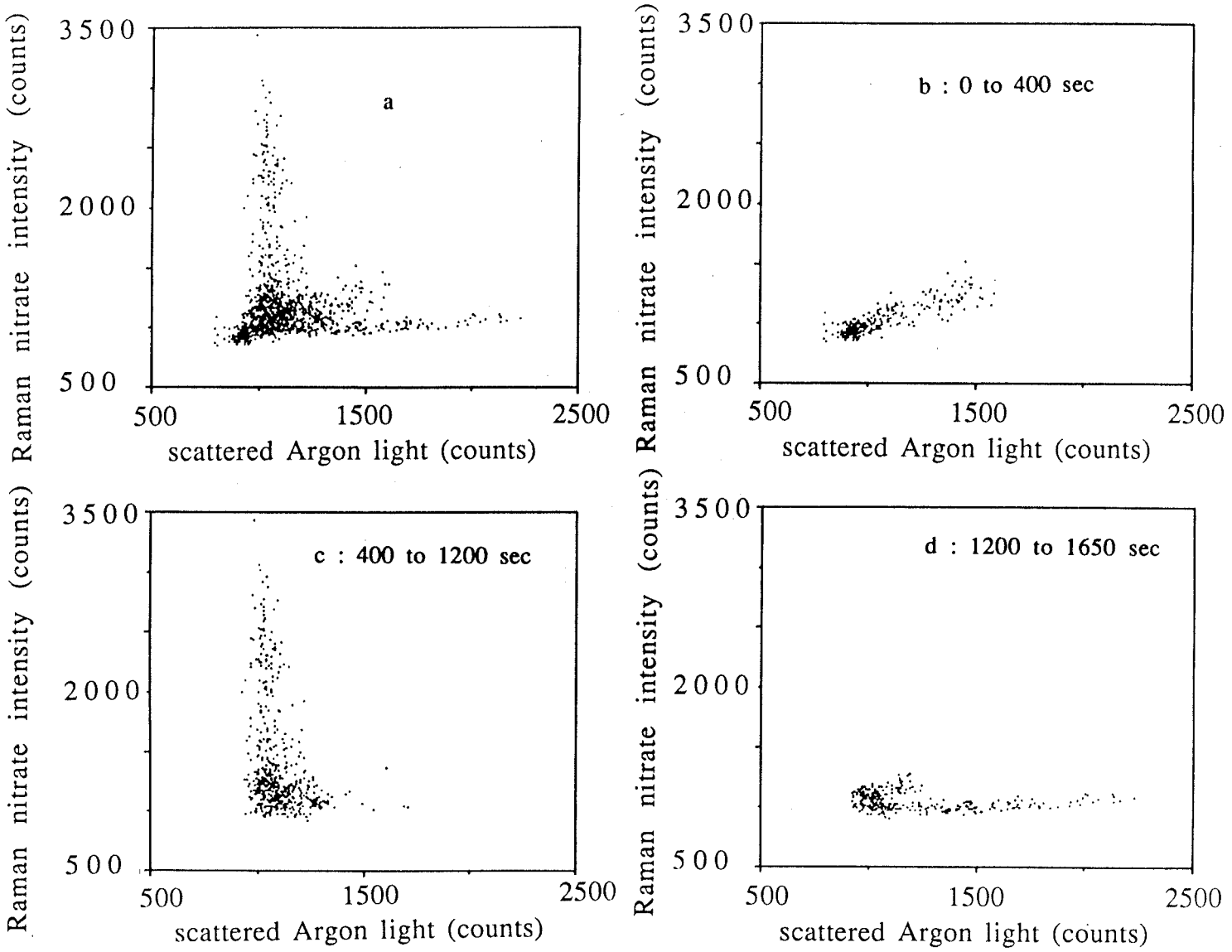


Figure 10 : Raman nitrate scattering intensity as a function of scattered Argon line intensity

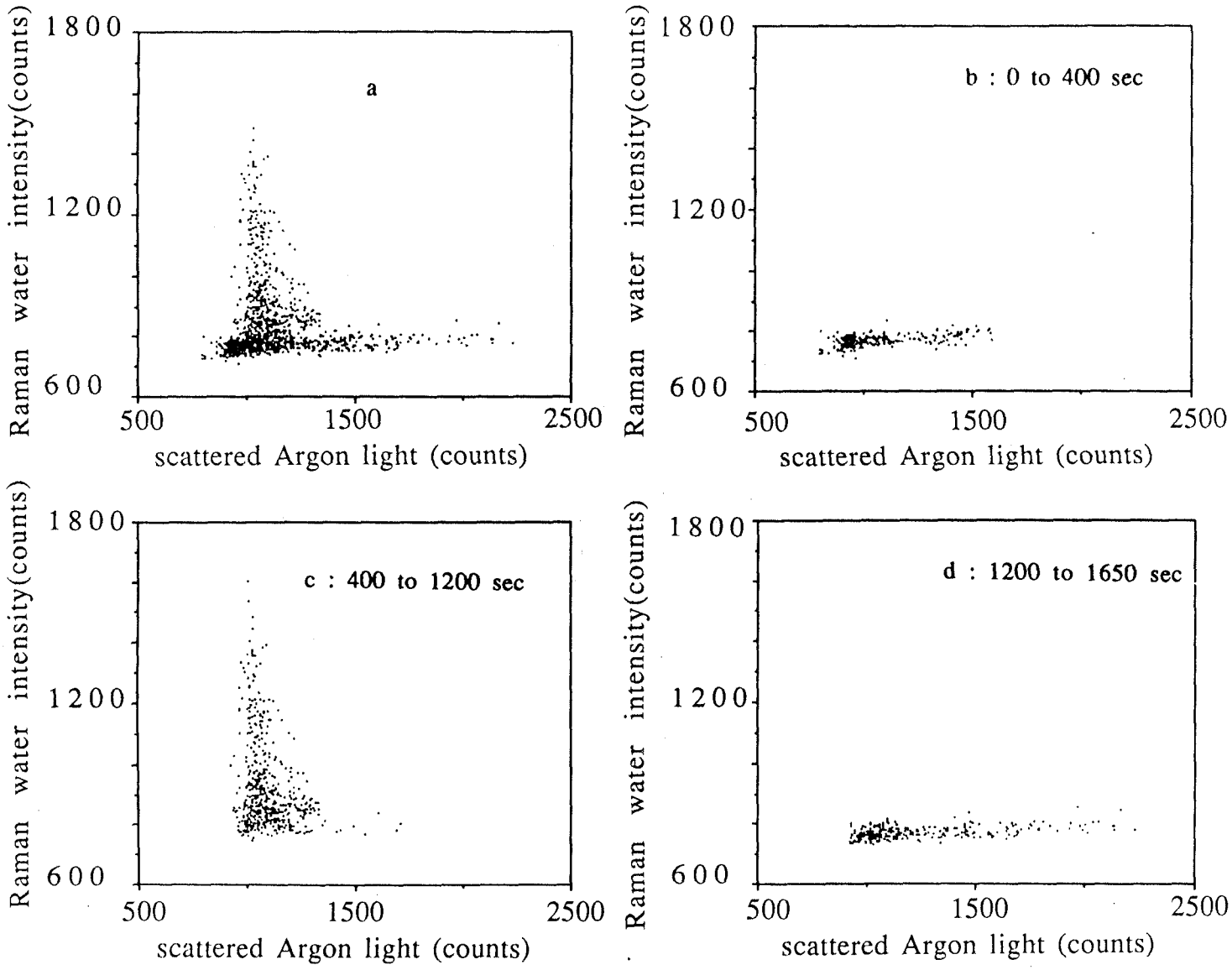


**Figure 11 : Raman water scattering intensity as a function of scattered Argon line intensity**

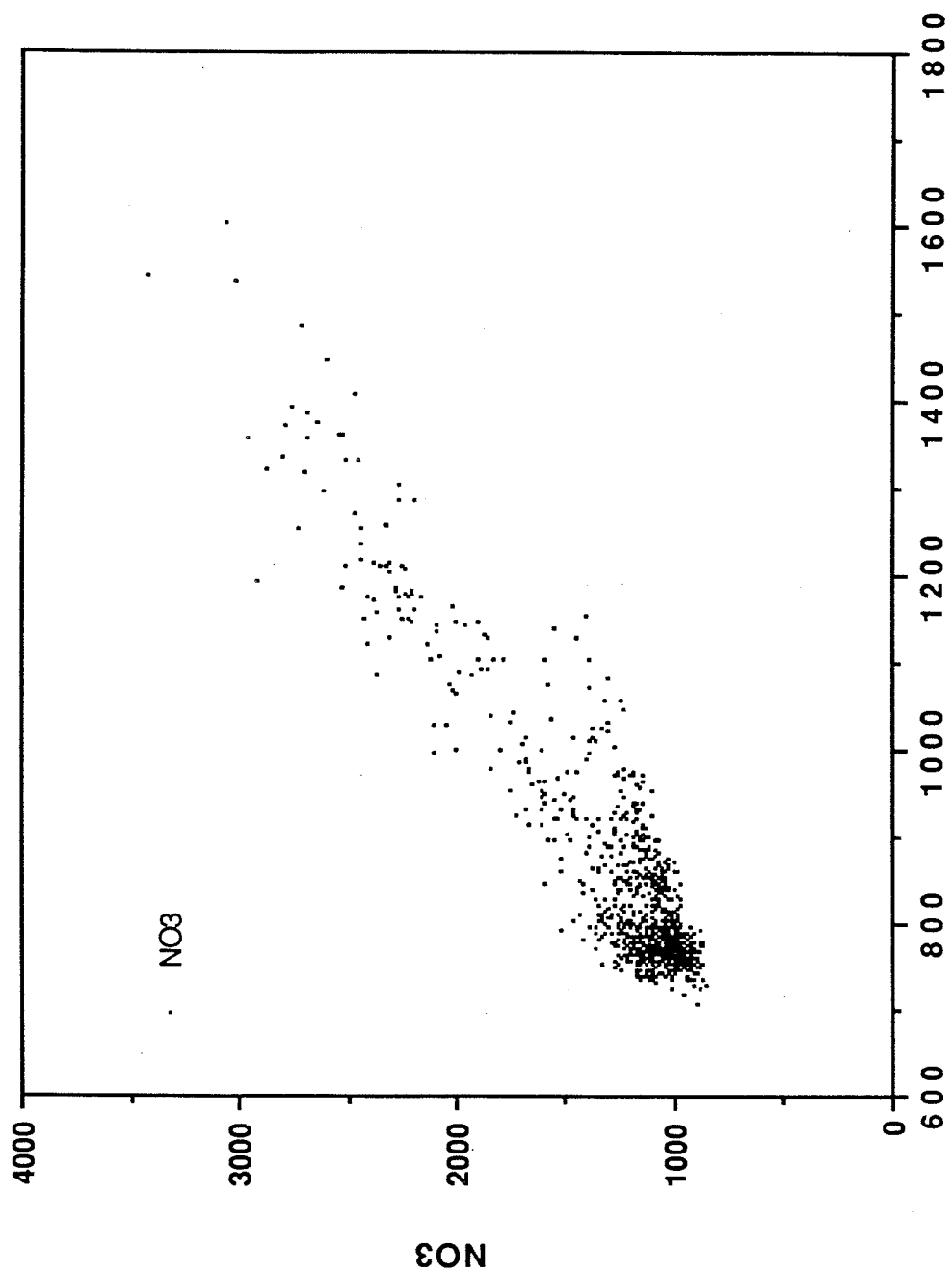


Figure 12 : Raman nitrate scattering intensity as a function of Raman water scattering intensity

**Chapter 3**

# WATER ACTIVITIES OF $NH_4NO_3/(NH_4)_2SO_4$ SOLUTIONS★

Chak K. Chan, Richard C. Flagan and John H. Seinfeld

Department of Chemical Engineering

California Institute of Technology

Pasadena, CA 91125

★ submitted to *Atmospheric Environment*

**Abstract**

Water activities for mixed ammonium nitrate/ammonium sulfate solutions at relative humidities of 0.35-0.75 were measured using a spherical void electrodynamic balance. The concentrations of singly levitated droplets of nitrate to sulfate mole ratio of $n$=1/5, 1/3, 1/2, 1, 2, and 4 in equilibrium with an ambient environment of prescribed relative humidity were measured. To avoid uncertainty in determining the composition of the solid particles, solution properties were determined relative to the known properties at about 80% relative humidity. The concentration of this reference state was estimated by three models of mixed electrolyte solutions, the Zdanovskii-Stokes-Robinson (ZSR), the Kusik and Meissner (KM), and the Pitzer models. The measured total mass fraction of solute of the mixed solutions differed by less than 0.5% when different models were used to calculate the reference state concentration. The water activity data were obtained at ionic strengths as high as 108 molal and used to evaluate predictions from these three models. For $n$=1/5 and 1/3, deviations of model predictions from experimental data are within 2%. Generally, predictions of the ZSR model are most consistent with our data. Maximum deviations occur at $n$=2; 6% for ZSR, 8% for KM, and 5% for Pitzer. The deviations can be attributed to binary and ternary solute-solute interactions that the ZSR, KM, and elementary version of the Pitzer models do not consider. However, no simple characterization of the interaction parameters is possible; they seem to be strong functions of the fractional ionic strength of the solute and the total ionic strength of the solutions.

## Introduction

The thermodynamics of the $NH_4NO_3-(NH_4)_2SO_4-H_2O$ system are important to understanding the properties of atmospheric aerosols. Of central importance is the effect of ambient relative humidity on the equilibrium composition of droplets of this system. In addition, ammonium nitrate is a volatile salt and ultimately leaves a droplet in the form of gaseous ammonia and nitric acid. Compositional data as a function of relative humidity are essential to understanding the effect of $(NH_4)_2SO_4$ on the loss of $NH_4NO_3$ from a mixed solution droplet.

Water activity data are valuable to the understanding of aerosol behavior at low relative humidity. Although water activities of individual single component aqueous solutions have been measured, data for mixed aqueous solutions are very limited. Stelson and Seinfeld(1981) pointed out that atmospheric aerosols could have ionic strengths exceeding 20 M. Tang *et al.*(1981) measured the water activity of bulk aqueous $NH_4NO_3/(NH_4)_2SO_4$ solutions up to $I_{max}$=19 M and 24 M at nitrate to sulfate ratios ($n$) of 1/3 and 2, respectively. Emons and Hahns (1970) also measured the activity of various $NH_4NO_3/(NH_4)_2SO_4$ mixtures as a function of temperature. A number of thermodynamic models of mixed electrolyte solutions are available to estimate water activity. Generally, these models are most appropriate at concentrations less than a few molal. Their validity for specific solute-solute pairs at concentrations exceeding this level needs to be verified experimentally. Unfortunately, water activity data at high supersaturation are difficult to

obtain in bulk samples because of nucleation on foreign surfaces.

Supersaturated solutions can be studied by levitation of solution droplets. Among the various methods of particle levitation, electrodynamic(Wuerker *et al.* 1959; Davis 1987), optical(Ashkin *et al.* 1977), magnetic(Beams 1950), and acoustic(Lee *et al.* 1982), the use of the electrodynamic balance is the most popular for the study of solution thermochemistry. Richardson *et al.* (1984ab) and Kurtz *et al.*(1984) measured the water activity of $(NH_4)_2SO_4$ and various lithium halide solutions. Water activity of other electrolyte solutions were also studied by Tang *et al.*(1984, 1986) and Cohen *et al.*(1987ab). Since micron-sized droplets can be freely levitated in a controlled environment, droplets can be studied at supersaturation ratios up to the point of homogeneous nucleation. Furthermore, the equilibration time of small droplets is much shorter than that for corresponding bulk samples. By knowing the ratio of the mass of a solution droplet in equilibrium at a prescribed ambient relative humidity to that of the dried solid salt particle, the salt concentration in the droplet can be determined. This requires that the composition of the dry particle be precisely known. The solid particle may contain water of hydration or liquid water trapped within a salt shell during crystallization. Cohen *et al.*(1987ab) found that the solid particle formed by drying a levitated droplet may not be the most thermodynamically stable form, *i.e.*, the number of waters of hydration may differ from that predicted thermodynamically. For some highly concentrated salt solutions, uncertainties in the dry state composition could lead to significant errors in the estimated solution concentration at high solute mass

fraction. For some of the salts they studied, Cohen *et al.*(1987ab) assumed a water to salt mole ratio of the dried state that best fit the literature water activity data at high relative humidity. Thus, water activity estimates at low relative humidity were based upon the bulk sample data at higher relative humidity. A more direct approach is to use the data at high relative humidity as a reference state to calculate the hypothetical pure solid salt mass. The concentration of the solution droplets at lower relative humidity can then be determined.

In this paper, we describe measurements of the water activity of aqueous ammonium nitrate/ammonium sulfate solutions at six nitrate to sulfate mole ratios ranging from 0.2 to 4.0. To avoid uncertainty in the determination of the composition of the solid particles, we will employ a wet state at high relative humidity as a reference state. Since even at high relative humidity, water activity - composition data for mixed $NH_4NO_3/(NH_4)_2SO_4$ solutions are still very limited, thermodynamic model predictions are required to estimate the composition of the reference state. Three different models of mixed electrolyte solutions will be used to predict the concentration of the mixed solutions at high relative humidity, and to compare with the data at lower relative humidity. These models selected require only water activity data of individual single electrolyte solutions. The validity and limitations of these models will be discussed.

**Measurements of water activities and concentrations of solution droplets**

A spherical void electrodynamic levitator (SVEL) was used to trap and levitate single solution droplets. The design of the balance was very similar to that described by Arnold and Folan(1987). Davis(1987) and Bar-Ziv and Sarofim(1991) have reviewed the fundamentals and applications of the conventional bihyperboloidal electrodynamic balance. The SVEL is one of many designs of the electrodynamic balance. Generally, an electrodynamic balance has a ring electrode between two endcap electrodes. DC and AC potentials are applied to the endcaps and the ring electrodes, respectively. The AC field provides a focussing force towards the center of the balance. In the SVEL, the inner surfaces of the electrodes are designed to form a spherical void. The electrodes are separated by Mylar insulation pieces 0.004 in thick and the spherical void has a diameter of 3/4 in. A particle is balanced when its own weight is counteracted by the force it experiences from the DC field. Therefore, relative mass measurements can be made from the DC potential required to balance the particle.

In the measurement of the water activity of levitated droplets, a flow system was set up to control and monitor the dew point of the stream going into the balance, as depicted by Figure 1. The ambient temperature was measured by a temperature probe of the dew point meter. High purity nitrogen at 70 kPa was used as a carrier gas for water vapor. The dew point of the stream was controlled by varying the ratio of the stream going to the bubbler and that bypassing it. The flow rate to the dew point meter was about 1 l

$min^{-1}$, whereas that to the balance was about 3 ml $min^{-1}$. The SVEL volume of about 4 $cm^3$ produced a residence time of 10 s in most of the experiments. The flow rate through the chamber was high enough to produce significant drag on the particle, so the balancing voltage was measured after momentarily stopping the flow. The DC balancing voltage was measured at 3 min intervals. Equilibration of the particle mass required about 20 min at each relative humidity. The temperature of the SVEL was stabilized to $\pm 0.5^{\circ}C$.

The chemical potential of water in the vapor phase is equal to that of the liquid at equilibrium,

$$\mu^{\circ}_{w,l} + RT\ ln\ a_w = \mu^{\circ}_{w,v} + RT\ ln\ \frac{p_w}{p_w^{sat}}\ , \qquad (1)$$

where $\mu^{\circ}_{w,l}$ and $\mu^{\circ}_{w,v}$ are the standard state chemical potentials of water in the liquid and vapor phases. $R$ is the gas constant and $T$ is the absolute temperature. $p_w$ is the water vapor partial pressure and $p_w^{sat}$ is the saturated water vapor pressure at temperature $T$. Ideal gas behavior is assumed and the influence of surface tension on the vapor pressure (the Kelvin effect) is neglected because the droplets used here are about 30 $\mu$m in diameter. Since the standard state chemical potentials are equal, equation (1) reduces to

$$a_w = \frac{p_w}{p_w^{sat}} = rh\ . \qquad (2)$$

Thus, the water activity of a solution droplet in equilibrium with water vapor can be determined simply by measuring the ambient dew point and

temperature. The DC field needed to balance the droplet at various relative humidities were measured. Data at high relative humidity (80%) were used for reference. By using bulk sample data or estimates derived with various mixing rules, the DC field required to balance the mass of the salt alone can be calculated. Using this hypothetical DC value, the concentration of the droplet at any relative humidity can then be obtained.

Six stock solutions of different nitrate to sulfate mole ratios of $n$=4, 2, 1, 1/2, 1/3, and 1/5 were used to generate droplets of the corresponding mole ratios. Three models of multicomponent electrolyte solutions were evaluated, the Zdanovskii-Stokes-Robinson (ZSR), the Kusik and Meissner (KM), and the Pitzer models (Stokes and Robinson 1966; Kusik and Meissner 1978; Pitzer and Kim 1974). Since these models require water activity data of the individual single electrolyte solutions, water activity measurements were also made for the individual nitrate and sulfate solutions.

**Models of water activity of mixed electrolyte solutions**

We measured water activity for a range of solution compositions, extending to ionic strength over 100 molal. The range of ionic strengths measured for the single electrolyte solutions and $NH_4NO_3/(NH_4)_2SO_4$ solutions are listed in Tables 1 and 2. Cohen *et al.*(1987b) measured the water activity of NaCl/KCl, NaBr/KBr and $NaCl/(NH_4)_2SO_4$ solution mixtures using the electrodynamic balance. They compared their predictions with the ZSR, the Reilly-Wood-Robinson (RWR), and Pitzer models. These models do not

account for co-operative interactions between ions, e.g., between $NO_3^-$ and $SO_4^{2-}$. Despite this simplification, the model predictions were in good agreement with the water activity data for the solutions studied. We will follow their analysis with the exception of using the Kusik – Meissner (KM) instead of the RWR model; the KM model is actually a special case of the more general RWR model. Stelson and Seinfeld(1982) used the KM model to predict the solute activity coefficients and water activity of the $NH_4NO_3/(NH_4)_2SO_4$ system. Their predictions were consistent with water activity measurements at high relative humidity of Tang *et al.*(1981). Since these models require water activity data of individual $NH_4NO_3$ and $(NH_4)_2SO_4$ solutions, we measured the concentration dependence of $a_w$ for $NH_4NO_3$ and $(NH_4)_2SO_4$ solutions.

Figures 2 and 3 show the mass fraction of solute as a function of water activity for $NH_4NO_3$ and $(NH_4)_2SO_4$ solutions, respectively. The data represent the mass fractions of solute calculated from a reference state at lower concentration. Literature bulk water activity data were used to estimate the solute concentration in the solution at the reference state (Hamer and Wu (1972), Stokes and Robinson (1966)). For $NH_4NO_3$, no water activity data at high concentrations were found that could be compared with our data. In the case of $(NH_4)_2SO_4$, Cohen *et al.*(1987ab) measured the water activity of single $(NH_4)_2SO_4$ droplets using the electrodynamic balance. We used their relative humidity and raw balancing voltage data to calculate the mass fraction of solute. Their data are consistent with ours and with bulk sample data.

In the ZSR model, which is one of the simplest mixing rules, the

molality of component $i$ ($m_i$) in a solution mixture having a water activity of $a_w$ can be calculated by (Stokes and Robinson 1966);

$$\sum_i \frac{m_i}{m_{o,i}(a_w)} = 1 \ , \tag{3}$$

where $m_{o,i}$ is the molality of the single electrolyte solution of component $i$ for which the water activity, $a_w$, equals that of the solution mixture. Since the molality of $NH_4NO_3$ solutions could be as high as 100 M at low relative humidity, the accuracy of the molality at low relative humidity is very sensitive to that of the reference solution at higher relative humidity. One needs to obtain as accurate a relationship as possible between concentration and water activity. Instead of obtaining a $m$(molality) vs. $a_w$ relationship, we determined a polynomial fit of mass fraction of solute ($mfs$) vs. $a_w$, which is less sensitive to the uncertainty in the reference state properties. The coefficients of the polynomial fit are listed in Table 1. $(NH_4)_2SO_4$ crystallizes at a higher water activity and lower ionic strength than $NH_4NO_3$. The data for $(NH_4)_2SO_4$ will set the limits of application of $a_{w,min} = 0.4748$ for the ZSR and $I_{max} = 53.66$ for the KM and Pitzer models, respectively. No water activity data for $(NH_4)_2SO_4$ beyond this limit are available. However, most of the mixed solution droplets we studied crystallized at a lower relative humidity than $a_{w,min}$. Among the three mixing rules we considered, the predictions from the ZSR model are most consistent with our data, even at a relative humidity lower than $a_{w,min}$.

The Kusik and Meissner (1978) model was derived from Bronsted's theory of specific ion interactions. The water activity, $a_w$, is given as a

function of total solution ionic strength, $I$, by

$$ln\ a_w = \left(\frac{2+Y}{3}\right) Y\ ln\ a^o_{w12} + \left(\frac{2+Y}{2}\right) Y\ ln\ a^o_{w14} - \frac{YM_wI}{6000}(1 - Y)\ , \qquad (4)$$

where $M_w$ is the molecular weight of water, and $Y$ is the ionic strength fraction of nitrate as defined by

$$Y = \frac{[NH_4NO_3]}{3[(NH_4)_2SO_4] + [NH_4NO_3]}\ , \qquad (5)$$

and where $a^o_{w12}$ and $a^o_{w14}$ are the water activities of individual $NH_4NO_3$ and $(NH_4)_2SO_4$ aqueous solutions at total ionic strength, $I$, respectively. Similar to the ZSR model, the KM model requires data on $a_w$ vs. ionic strength for the single electrolyte solutions. As mentioned earlier, we found that the $a_w$ vs. *mfs* relationship is more accurate for the single electrolyte data. Coefficients of the polynomial fits of $a_w$ vs. *mfs* are listed in Table 1. Since the KM model requires $a_w$ data as a function of the total ionic strength, the limit of the applicability of the model was restricted by the $I_{max}$ of $(NH_4)_2SO_4$, instead of $a_{w,min}$. Generally, this limit corresponds to a lower water activity than $a_{w,min}$.

The full version of the Pitzer model requires parameters describing the binary interactions among different ions of the same sign ($NO_3^- - SO_4^{2-}$ interactions) and ternary interactions among different ions not all of the same sign ($NO_3^- - NH_4^+ - SO_4^{2-}$ interactions). To the first approximation, only the binary solute-solvent and cation-anion interactions, as reflected in the

concentration dependence of $a_w$, are accounted for in the elementary model. In the Pitzer model, the osmotic coefficient, $\phi$, of a mixture of electrolyte solutions can be calculated by (Pitzer and Kim 1974)

$$(\phi - 1)\sum_i m_i = 2If^{\phi} + 2\sum_c \sum_a m_c m_a \left[ B_{ca}^{\phi} + \frac{(\sum mz)}{(z_c z_a)^{1/2}} C_{ca}^{\phi} \right] + \ldots \qquad (6)$$

where

$$B_{ca}^{\phi} = \beta_{ca}^{(0)} + \beta_{ca}^{(1)} \exp(-\alpha I^{1/2}) \qquad (7)$$

$$(\sum mz) = \sum_c m_c z_c = \sum_a m_a |z_a| \qquad (8)$$

$$f^{\phi} = -A_{\phi} \left[ \frac{I^{1/2}}{1.0 + 1.2I^{1/2}} \right] \qquad (9)$$

and where $A_{\phi}$ = -0.392 for water at 25$^o$ C, and $\alpha$ = 2.0. The Pitzer parameters, $\beta_{ca}^{(0)}$, $\beta_{ca}^{(1)}$, and $C_{ca}^{\phi}$, are for the single electrolyte solutions of cation $c$ with charge $z_c$ and anion $a$ with charge $z_a$. The summation $\sum_i m_i$ is over all ionic species. The parameters for $(NH_4)_2SO_4$ and $NH_4NO_3$ at high relative humidity can be obtained from Pitzer and Mayorga(16). However, for low water activity data, new sets of parameters were required to fit the data. For single electrolyte solutions, Pitzer parameters, $\beta_{ca}^{(0)}$, $\beta_{ca}^{(1)}$, and $C_{ca}^{\phi}$ are defined by

$$\phi - 1 = |z_c z_a| f^{\phi} + m\left(\frac{2\nu_c \nu_a}{\nu}\right) B_{ca}{}^{\phi} + m^2 \frac{2(\nu_c \nu_a)^{3/2}}{\nu} C_{ca}{}^{\phi}, \qquad (10)$$

where $B_{ca}{}^{\phi}$ is defined as in equation (7). $\nu_c$ and $\nu_a$ are numbers of ions in the formula and $\nu = \nu_c + \nu_a$.

Data for $NH_4NO_3$ and $(NH_4)_2SO_4$ solutions were fitted with the above equation to obtain the corresponding Pitzer parameters. Table 1 lists the Pitzer parameters from the literature and from our data. Figures 2 and 3 show the calculated *mfs* as a function of the water activity for $NH_4NO_3$ and $(NH_4)_2SO_4$, respectively, using the modified Pitzer parameters. For comparison, predictions using the unmodified literature Pitzer parameters derived from bulk sample studies are also shown (Pitzer and Mayorga 1973). For $(NH_4)_2SO_4$, even the unmodified Pitzer parameters work quite well. But for $NH_4NO_3$, the new set of Pitzer parameters are needed to describe the concentration at low relative humidity.

**Evaporation of ammonium nitrate from solutions**

A potential problem associated with measuring the water activity of ammonium nitrate/ammonium sulfate salt solutions is the volatility of ammonium nitrate. Richardson and Hightower(1987, 1988) measured the evaporation rate of solid ammonium nitrate and mixed ammonium nitrate/ammonium sulfate dry particles at high vacuum. In our water activity measurements at atmospheric pressure, four to six hours were generally required to obtain a complete set of data for each particle. We noted no significant loss of mass over this period. In all water activity measurements, there was at least one particle for which the relative humidity was increased from about 50% to 75% and then decreased until it crystallized. The concentration of the droplet at 50% was the same before and after the relative humidity was increased to 75%. Also, all the particles studied at each nitrate/sulfate mole ratio exhibited

consistent water activity data. Therefore, we believe that water activity data were not influenced by transient evaporation.

**Water activity data and model predications**

Since solution droplets at high relative humidity were used as a reference state, the composition of the solution droplets at the chosen nitrate to sulfate mole ratio at the reference relative humidity was required. The only relevant data are those of Tang *et al.*(1981) who measured absolute water vapor pressure of bulk samples at nitrate/sulfate mole ratios of $n$=2 and 1/3 and of Emons and Hahn(1970) who measured the water activity of various $NH_4NO_3/(NH_4)_2SO_4$ mixtures as a function of temperature. Unfortunately, we could not directly use the data of Emons and Hahn since the mole ratios they used differed from those studied here. Since data are not available for all of the mole ratios studied, the concentration of the reference state for each particle were estimated using the thermodynamic models which should be quite accurate at this dilute state. The total mass fraction of solute calculated using reference state compositions estimated with the three different models differed by less than 0.5%. Henceforth, the reference state properties will be calculated using the ZSR model. Figures 4 to 9 show the total mass fraction of solute as a function of water activity for various values of $n$. 3 to 4 particles were studied at each $n$; the solid points represent particles after crystallization of the droplets. Some of these solid particles apparently still contained water because the measured *mfs* values were significantly less than 1.0. This exemplifies the uncertainty introduced when solution concentrations are calculated with reference to the

solid particle. In most cases, different particles having the same $n$ crystallized at different supersaturation ratios. One exception was at $n$=2, where nucleation occurred at a relative humidity of $0.385 \pm 0.05$ for the three particles studied. It should be noted that in bulk sample studies ammonium nitrate and ammonium sulfate solutions form a stable solid salt mixture at a stoichiometric ratio of 2:1 after crystallization (Silcock 1979). There was no definite trend of the crystallization water activity. This may merely be a manifestation of the random nature of nucleation. Direct predictions from the three models are also shown for comparison. For $n$=2 and 1/3, data from Tang *et al.*(1981) are also shown. They are in general agreement with our data and with predictions of the three models. Since the total ionic strength is customarily used to describe the KM and Pitzer models, the corresponding $I$ values are also indicated in the figures. The ZSR model was limited by the $a_{w,min}$ (=0.4748) of the $(NH_4)_2SO_4$ solution data. The cases of the KM and Pitzer models are similar, except that they are limited by the maximum total ionic strength of the solution $I_{max}$ (=53.66). The ranges of application of these models are also indicated in the figures. Predictions beyond these ranges assume that the water activity data of $(NH_4)_2SO_4$ exhibit the same trend as described by the $mfs - a_w$ polynomial fits and the Pitzer parameters listed in Table 1. Table 2 lists the coefficients of polynomial fits in the form of $mfs$ vs. $a_w$ at each $n$. The ranges of $a_w$ and $I$ studied are also shown.

There are two major challenges to mixing rules: 1) performance at high concentrations and 2) performance in the presence of strong interactions among electrolytes. Indicative of this interaction is the fractional ionic strength of

nitrate as defined by $Y$(Eq. (5)). When $Y$=0.5, the two solutes contribute equally to the ionic strength of the solution. If the strength of electrolyte-electrolyte interaction is proportional to the ionic strength of the individual electrolyte solution, one would expect maximum interactions at $Y$=0.5. In Figures 10, 11, and 12, the percentage error in *mfs* as a function of $n$ at $a_w$ =0.7, 0.6, 0.5, and 0.4 for the 3 models are shown. The $mfs_{meas}$ for each selected $a_w$ at each $n$ are calculated from the corresponding polynomial fits of the actual data listed in Table 2, whereas $mfs_{cal}$ are calculated directly from the models. We will discuss the model performance with reference to these figures and Figures 4 - 9 which show the *mfs* vs. $a_w$ data at each $n$.

The ZSR model predictions match experimental observations within 6% over the entire range of $a_w$ studied. Of the models examined, the ZSR model is most consistent with our data. Its predictions beyond $a_{w,min}$ generally exhibited the same trend as the data and therefore could also be used as estimates of composition at lower water activity. In Figure 10, predictions at $a_w$ = 0.7 are accurate to within 1%. The deviations of prediction from experimental data increases as $a_w$ decreases to 0.5. The deviations decrease again as $a_w$ decreases further to 0.4, which is contrary to what one would expect. As the concentration of the solute increases, one would expect the model predictions to become less accurate. However, it should be noted that $a_w$ = 0.4 is beyond the range of application of the model ($a_{w,min}$=0.4748). Maximum deviations at $a_w$=0.4 are about 4%, which compares to those of the KM and the Pitzer models. The predictions at $n$= 1/5, 1/3, and 1/2 are accurate to 2%. The deviation increases to a maximum of 6% at $n$=2 ($Y$=0.4)

and decreases again at $n$=4. We will discuss this behavior in the next section.

The KM model is least consistent with our data although its predictions are within 2% of the data at $n$=1/3 and $n$=1/5. At $a_w$ above 0.7, its predictions are the same as those of the ZSR model; it begins to underestimate water activity below $a_w$=0.7 at which model predictions are accurate to 1%. As shown in Figure 11, the deviation increases as $a_w$ decreases until it peaks at $a_w$=0.5. Again, we believe that the better accuracy at $a_w$=0.4 than at $a_w$=0.5 is not meaningful because the model has been applied beyond its range of application. Similar to the case of ZSR, maximum deviations occur at $Y$=0.4, which is about 8% in the KM model.

Predictions from the Pitzer model are similar to those of the ZSR model for values of $I$ less than $I_{max}$, except for $n$=2 and $n$=4. Recall that the Pitzer model requires parameters for the $NH_4NO_3$ and $(NH_4)_2SO_4$ solutions. Qualitatively, the Pitzer fit of the $NH_4NO_3$ solution is not as good as that of $(NH_4)_2SO_4$ as shown in Figures 2 and 3. In the ZSR model, 6th degree polynomial fits are used and are more accurate than the case of the Pitzer fit to describe the water activity data of $NH_4NO_3$ and $(NH_4)_2SO_4$ solutions. Therefore, the predictions of the Pitzer mixing model deviate from those of the ZSR model at high $a_w$ as $n$ increases. The predictions above $I_{max}$ are very poor and therefore percentage deviations at $a_w$=0.4 are not shown in Figure 12. The unmodified Pitzer parameters for $(NH_4)_2SO_4$ solutions are quite satisfactory; the fact that predictions above $I_{max}$ are so poor reflects the sensitivity of the model to the parameters used for single components. The predictions at $a_w$=0.7

are within 3%, which increases to 5% at $a_w$=0.5. Its predictions are not as accurate as those of the ZSR model but are superior to those of the KM model. Similar to the ZSR and KM models, the predictions of $n$=1/5 and $n$=1/3 are very accurate to within 2%. Deviations peak at $Y$=0.4 again.

Based on the performance of the three models, we conclude that the ZSR model provides the best estimates of the water activity of mixed $NH_4NO_3$ /$(NH_4)_2SO_4$ solutions. Not only are its predictions the most accurate within the application range of the model, they are superior to those of the KM and Pitzer models above $I_{max}$. However, the ZSR model does not embody a formalism for solute activity coefficients that are useful for predictions of chemical equilibrium. The ZSR model is a relatively empirical model which does not allow for improvements, such as accounting of solute ion interactions. On the other hand, the Pitzer model predicts the solute activity coefficients and can be extended through additional terms. Therefore, on the basis of strictly predicting water activities, the ZSR model is superior to the other two, but for a model that incorporates more basic aspects of the system, the Pitzer model is preferred.

**Interactions between the solute ionic species**

In the last section, we found that the maximum deviations for all three models occur at $Y$=0.4 (or $n$=2). This observation can be attributed to the interactions between individual electrolytes. All three models considered here require only solute-solvent and cation-anion interactions of the individual

electrolytes to describe the effect of composition on water activity. It is anticipated that these models would not perform well in the presence of significant multicomponent solute-solute interactions. Because of the high ionic strength achieved in the $NH_4NO_3-(NH_4)_2SO_4-H_2O$ system, we explored the contributions of multicomponent solute-solute interactions. The Pitzer model as presented in equation (6) is incomplete. The omitted terms are contributions of the binary interactions of different ions of the same sign and ternary interactions of different ions not all at the same sign. We will compare the simple version of the Pitzer model presented in equation (6) to the full Pitzer model, which incorporates multicomponent solute-solute interaction. The ratio of the measured water activity and that predicted by equation (6) is indicative of the multicomponent solute-solute interactions. We will follow the analyses of Pitzer and Kim (1974) to determine the interaction parameters. The dependence of the interaction parameter on $n$ and $I$ will then be discussed.

For the system of $NH_4NO_3-(NH_4)_2SO_4-H_2O$, the osmotic coefficient in the full Pitzer model differs from that in the simple model by (Pitzer and Kim 1974);

$$\Delta\phi = \phi_{full} - \phi_{simple} = 2\left(\sum_i m_i\right)^{-1} m_N m_S \left(\theta_{NS} + I\frac{\partial\theta_{NS}}{\partial I} + (m_A)\psi_{ANS}\right), \qquad (11)$$

where $\phi_{full}$ and $\phi_{simple}$ denote osmotic coefficients calculated from the full Pitzer model and from Equation (6), respectively; $A$, $N$, and $S$ stand for $NH_4^+$, $NO_3^-$, and $SO_4^{2-}$. $\theta_{NS}$ and $\psi_{ANS}$ are parameters describing the binary interactions of $NO_3^-$/ $SO_4^{2-}$ ions and ternary interactions of $NH_4^+/NO_3^-/SO_4^{2-}$

ions, respectively. It is their dependence on $n$ and $I$ that we will investigate from our data and the predictions from Equation (6). The osmotic coefficient can be related to the water activity by

$$\phi = - \frac{1000}{M_w \sum m_i} ln\ a_w\ , \tag{12}$$

Equation (11) can then be transformed to

$$- \frac{1000\ ln(a_{w,meas}/a_{w,simple})}{2M_w m_N m_S} = \left( \theta_{NS} + I\frac{\partial \theta_{NS}}{\partial I} + (m_A)\ \psi_{ANS} \right), \tag{13}$$

where $a_{w,meas} = a_{w,full}$, assuming the full Pitzer model is a perfect predictor of the $a_w$ data.

Pitzer and Kim (1974) found that the interaction parameters $\theta$ and $\psi$ are constants for a number electrolyte pairs at $I$ below 10 M. We seek to determine if the water activity of $NH_4NO_3/(NH_4)_2SO_4$ solutions at high ionic strengths can be completely described using constant $\theta_{NS}$ and $\psi_{ANS}$ and the Pitzer parameters of the individual electrolyte solutions. If $\theta_{NS}$ is independent of $I$, equation (13) can be rewritten in the form of

$$P(n,I) = \theta_{NS} + Q(n,I)\psi_{ANS}\ , \tag{14}$$

where $$P(n,I) = - \frac{1000\ ln(a_{w,meas}/a_{w,simple})}{2M_w m_N m_S} \tag{15}$$

and $Q(n,I) = m_A$. If both $\theta_{NS}$ and $\psi_{ANS}$ are constants, a linear relationship

between $P(n,I)$ and $Q(n,I)$ should result. $\theta_{NS}$ and $\psi_{ANS}$ can then be determined from the intercept and slope of that relationship.

To explore the relationship between $P(n,I)$ and $Q(n,I)$, the polynomial fits through the *mfs* vs. $a_w$ data were used to calculate $P(n,I)$ and $Q(n,I)$ for various $n$. Figure 13 characterizes $\theta_{NS}$ and $\psi_{ANS}$ in the form of $P(n,I)$ vs. $Q(n,I)$. Our data of $n$=1/3 and $n$=1/5 resemble predictions from the simple Pitzer model; they are not shown because the deviations are not significant to represent the contributions of solute-solute interactions. Also, the values of $P(n,I)$ and $Q(n,I)$ are limited by $I_{max}$=53.66 and the lowest $I$ we studied at each $n$. For any $n$, $P(n,I)$ is not linearly related to $Q(n,I)$, indicating that $\theta_{NS}$ and $\psi_{ANS}$ may be strong functions of $n$ and $I$. We can identify 3 different groups of behavior, $n$=1 and 1/2, $n$=4, and $n$=2. The behavior at $n$=2 can be interpreted as a combination of those at $n$=1, 1/2, and $n$=4. In Figures 10-12, we found that maximum deviations for the ZSR, KM and simple version of Pitzer models occurred at $n$=2 ($Y$=0.4). This suggests that $\theta_{NS}$ and $\psi_{ANS}$ may be strong functions of $Y$. We expect $\theta_{NS}$ to peak at $Y$=0.5 at which point both electrolytes contribute equally to the ionic strength of the solution. The maximum deviation occurring at $Y$=0.4 (not 0.5) can be explained by the preferential interaction of $NH_4^+ - NO_3^-$ over $NH_4^+ - SO_4^{2-}$ in their contributions to $\psi_{ANS}$. The exact dependence of $\theta_{NS}$ and $\psi_{ANS}$ on $Y$ and $I$ are not known. The inability to characterize $\theta_{NS}$ and $\psi_{ANS}$ quantitatively hinders the use of the full Pitzer model to predict water activities of $NH_4NO_3/(NH_4)_2SO_4$ solutions. Therefore, application of the Pitzer is limited to Equation (6) which considers only individual single electrolyte solution

properties.

## Conclusions

The water activity as a function of solute concentration of mixed $NH_4NO_3$/ $(NH_4)_2SO_4$ solutions at nitrate/sulfate mole ratios of $n$=4, 2, 1, 1/2, 1/3, and 1/5 has been measured using an electrodynamic balance. To avoid the uncertainty associated with the composition of the solid particles formed by crystallization, droplets at high relative humidity were used as reference states. Three mixing rule models were used to estimate the concentration of the reference and they all gave very similar results. The water activity data were also used to evaluate these models, especially at high ionic strengths. The range of application of the models is limited by the availability of water activity vs. ionic strength data of $(NH_4)_2SO_4$ solutions. For the ZSR model, the limit is $a_{w,min}$ = 0.4748, below which no water activity data of $(NH_4)_2SO_4$ are available. For the KM and Pitzer models, the corresponding limit is $I_{max}$ = 53.66 molal.

The ZSR model performed the best among the three models we tested; its predictions are within 6%. Above $a_{w,min}$, its predictions are quite satisfactory whereas predictions of the KM and Pitzer models above $I_{max}$ do not agree with the data. The ZSR model, however, does not include a formalism for solute activity coefficients which are necessary for modeling of chemical equilibrium. In this light, the Pitzer model is recommended if basic thermodynamic understanding of the system is desired. The simple Pitzer

model using only information from single electrolyte solutions predicts *mfs* to within 5%, although it is not as accurate as the ZSR model in some cases. Predictions from these three models are accurate to 2% with respect to the experimentally determined *mfs* for mole ratios ($n$) of 1/3 and 1/5. As the mole ratio becomes higher, the models become less accurate until $n$=2 or equivalently at a fractional ionic strength of nitrate of 0.4. At $n$=4, the deviation of model predictions from experimental data decreases. Deviations between model and data are probably due to solute-solute binary and ternary interactions that are not considered. Using the full description of the Pitzer theory, the binary and ternary interaction parameters of the $NH_4NO_3/(NH_4)_2SO_4$ system are found to be dependent on the mole ratio, the fractional ionic strength of nitrate, and the total ionic strength of the solution. The relationship among the interaction parameters and solution properties are apparently very complex, and no simple characterization of the interaction parameters appears to hold.

**Acknowledgment**

This work was supported by National Science Foundation Grant ATM-9003186.

References

Ashkin A. and Dziedzic J. M. (1977) Feedback stabilization of optically levitated particles. *Appl. Phys. Lett.* **30**, 202-204.

Arnold S. and Folan L. M. (1987) Spherical void electrodynamic levitator. *Rev. Sci. Instrum.* **58(9)**, 1732-1735.

Bar-Ziv E. and Sarofim A. F. (1991) The electrodynamic chamber: a tool for studying high temperature kinetics involving liquid and solid particles. *Prog. Energy Combust. Sci.* **17**, 1-65.

Beams J. W. (1950) Magnetic suspension for small rotors. *Rev. Sci. Instrum.* **21(2)**, 182-184.

Cohen M. D., Flagan R. C. and Seinfeld J. H. (1987) Studies of concentrated electrolyte solutions using the electrodynamic balance. 1. Water activities for single-electrolyte solutions. *J. Phys. Chem.* **91**, 4563-4574.

Cohen M. D., Flagan R. C. and Seinfeld J. H. (1987) Studies of concentrated electrolyte solutions using the electrodynamic balance. 2. Water activities for mixed electrolyte solutions. *J. Phys. Chem.* **91**, 4575-4582.

Davis E. J. (1987) Single aerocolloidal particle instrumentation and measurement. *Surface and Colloid Science* **14**, E. Matijevic (Ed.), Plenum Press, NY.

Emons V. H. and Hahn W. (1970) Dampfdruckmessungen im system ammonnitrat-ammonsulfat-wasser. *Wissenschaftl. Zeitschr.* **12, Heft2**, 129-132.

Hamer W. J. and Wu Y. (1972) Osmotic coefficients and mean activity coefficients of uni-univalent electrolytes in water at 25°C. *J. Phys. Chem.*

*Ref. Data* **1(4)**, 1047-1099.

Hightower R. L. and Richardson C. B. (1988) Evaporation of ammonium nitrate particles containing ammonium sulfate. *Atmos. Environ.* **22(11)**, 2587-2591.

Kurtz C. A. and Richardson C. B. (1984) Measurement of phase changes in a microscopic lithium iodide particle levitated in water vapor. *Chem. Phys. Lett.* **109(2)**, 190-194

Kusik C. L. and Meissner H. P. (1978) Electrolyte activity coefficients in inorganic processing. *AICHE Symp.* **173**, 14-20.

Lee M. C. and Feng I. (1982) Acoustic levitating apparatus for submillimeter samples. *Rev. Sci. Instrum.* **53**, 854-859.

Pitzer K. S. and Kim J. J. (1974) Thermodynamics of electrolytes. IV. Activity and osmotic coefficients for mixed electrolytes. *J. Am. Chem. Soc.* **96(18)**, 5701-5717.

Pitzer K. S. and Mayorga (1973) Thermodynamics of electrolytes. II. Activity and osmotic coefficients for strong electrolytes with one or both ions univalent. *J. Phys. Chem.* **77(19)**, 2300-2308.

Richardson C. B. and Hightower R. L. (1987) Evaporation of ammonium nitrate particles. *Atmos. Environ.* **21(4)**, 971-975.

Richardson C. B. and Kurtz C. A. (1984) A novel isopiestic measurement of water activity in concentrated and supersaturated lithium halide solutions. *J. Am. Chem. Soc.* **106**, 6615-6618.

Richardson C. B. and Spann (1984) Measurement of the water cycle in a levitated ammonium sulfate particle. *J. Aerosol Sci.* **15(5)**, 563-571.

Robinson R. A. and Stokes R. H. (1959) *Electrolyte solutions.* 2nd ed., Butterworths, London.

Seinfeld J. H. (1986) *Atmospheric Chemistry and Physics of Air Pollution.* John Wiley & Sons, New York.

Stelson A. W. and Seinfeld J. H. (1981) Chemical mass accounting of urban aerosol. *Environ. Sci. Technol.* **15,** 671-679.

Stelson A. W. and Seinfeld J. H. (1982) Thermodynamic prediction of the water activity, $NH_4NO_3$ dissociation constant, density and refractive index for the $NH_4NO_3-(NH_4)_2SO_4-H_2O$ system at 25°C. *Atmos. Environ.* **15(10),** 2507-2514.

Silcock H. L. (1979) *Solubilities of inorganic and organic compounds.* Vol. 3, part 2, 157-159, Pergamon Press, NY.

Stokes R. H. and Robinson R. A. (1966) Interactions in aqueous nonelectrolyte solutions. I. Solute-solvent equilibria. *J. Phys. Chem.* **70,** 2126-2131.

Tang I. N. and Munkelwitz H. R. (1984) An investigation of solute nucleation in levitated solution droplets. *J. Coll. Interf. Sci.* **98,** 430-438.

Tang I. N., Wong W. T. and Munkelwitz H. R. (1981) The relative importance of atmospheric sulfates and nitrates in visibility reduction. *Atmos. Environ.* **15(12),** 2463-2471.

Tang I. N., Munkelwitz H. R. and Wang N. (1986) Water activity measurements with single suspended droplets, the NaCl-$H_2O$ and HCl-$H_2O$ systems. *J. Coll. Interf. Sci.* **114(2),** 409-415.

Wuerker R. F., Shelton H. and Langmuir R. V. (1959) Electrodynamic containment of charged particles. *J. Appl. Phys.* **30(2),** 342-349.

**List of Figures**

Table 1 Correlations Between Water Activity ($a_w$) and Mass Fraction of Solute ($mfs$) for $NH_4NO_3$-$H_2O$ and $(NH_4)_2SO_4$-$H_2O$ Solutions

| | $NH_4NO_3$-$H_2O$ | $(NH_4)_2SO_4$-$H_2O$ |
|---|---|---|
| ZSR model | $mfs = 0.2906 + 6.83665a_w - 26.9093a_w^2 + 46.6983a_w^3 - 38.803a_w^4 + 11.8837a_w^5$ | $mfs = 2.27515 - 11.147a_w + 36.3369a_w^2 - 64.2134a_w^3 + 56.8341a_w^4 - 20.0953a_w^5$ |
| KM model | $a_w = 0.997692-0.308705mfs - 0.809162mfs^2 + 2.87184mfs^3 - 4.80375mfs^4 + 2.18933mfs^5$ | $a_w = 1.0004 - 0.295351mfs - 0.113992mfs^2 + 1.55769mfs^3 - 8.17712mfs^4 + 6.98261mfs^5$ |
| Pitzer model (modified fit) | $\beta^o = -0.00726224$<br>$\beta^1 = -1.68858$<br>$C^\phi = 3.5217e\text{-}5$ | $\beta^o = 0.046465$<br>$\beta^1 = -0.54196$<br>$C^\phi = -0.0012683$ |
| Pitzer model (unmodified fit) | $\beta^o = -0.0154$<br>$\beta^1 = 0.112$<br>$C^\phi = -0.0003$ | $\beta^o = 0.04088$<br>$\beta^1 = 0.6585$<br>$C^\phi = -0.00116$ |
| Range of data | $a_{w,min} = 0.2904$<br>$I_{max} = 112.82$ *molal*<br>$mfs_{max} = 0.9003$ | $a_{w,min} = 0.4748$<br>$I_{max} = 53.66$ *molal*<br>$mfs_{max} = 0.7028$ |

Table 2 : Correlation of Experimental Data on Water Activity($a_w$) and Total Mass Fraction of Solute (*mfs*) for $NH_4NO_3$-$(NH_4)_2SO_4$-$H_2O$ Solutions at 298K in the Form: $mfs = K_0 + K_1 a_w + K_2 a_w^2 + .....$

| $n^*$ | $K_0$ | $K_1$ | $K_2$ | $K_3$ | $K_4$ | $K_5$ | $a_w$ *measured* | *I measured(molal)* |
|---|---|---|---|---|---|---|---|---|
| 4 | 1.96806 | -8.89387 | 30.2184 | -52.7183 | 43.3316 | -13.7017 | 0.3566-0.7416 | 16.91-105.4 |
| 2 | 8.15067 | -68.2755 | 255.253 | -472.832 | 429.489 | -153.574 | 0.3892-0.7462 | 16.77-95.76 |
| 1 | 1.32102 | -2.29929 | 3.70363 | -1.61799 | -4.23649 | 3.52529 | 0.3535-0.7704 | 16.83-108.5 |
| 1/2 | 1.03017 | 0.908123 | 2.48450 | -6.82038 | 7.55714 | -3.25772 | 0.3171-0.7408 | 20.45-108.4 |
| 1/3 | 7.69587 | -56.6105 | 185.478 | -303.385 | 244.992 | -78.4443 | 0.4406-0.7837 | 16.75-60.36 |
| 1/5 | -6.03519 | 63.8971 | -233.696 | 418.542 | -370.3947 | 130.001 | 0.3855-0.7648 | 19.76-68.51 |

*$n$ = mole ratio of nitrate to sulfate

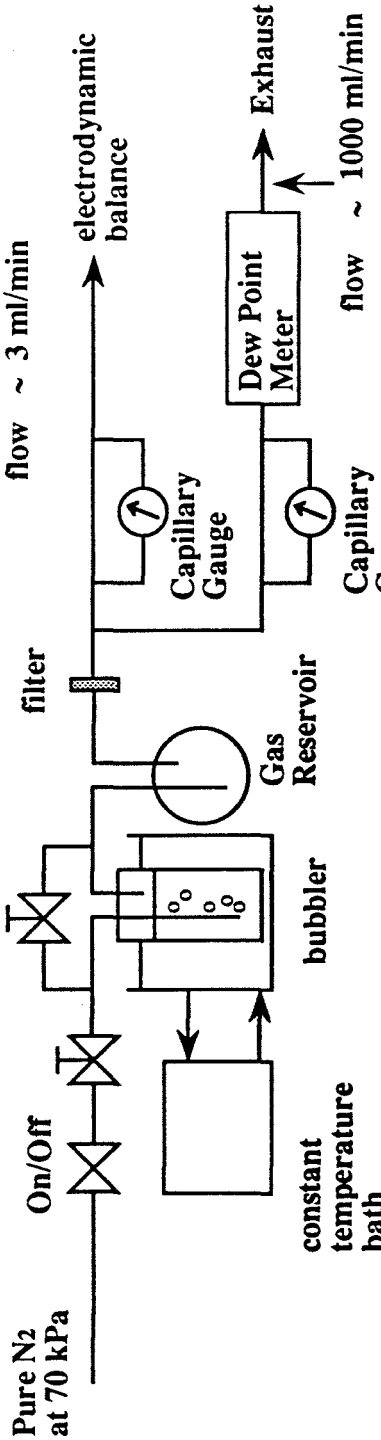


**Figure 1: Control and measurement of relative humidity for the ambient environment of the electrodynamic balance**

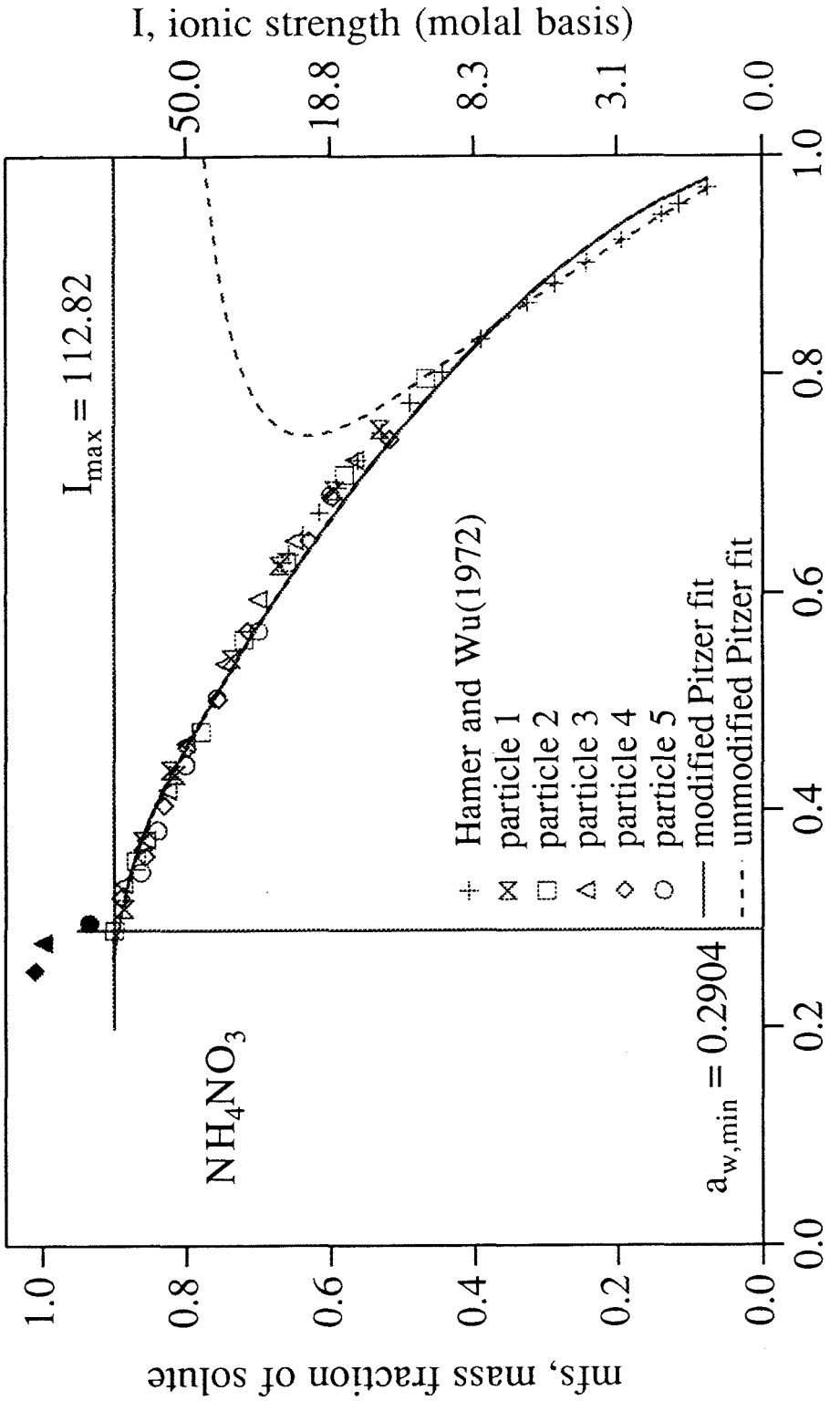


Figure 2: Water activity data for ammonium nitrate solutions

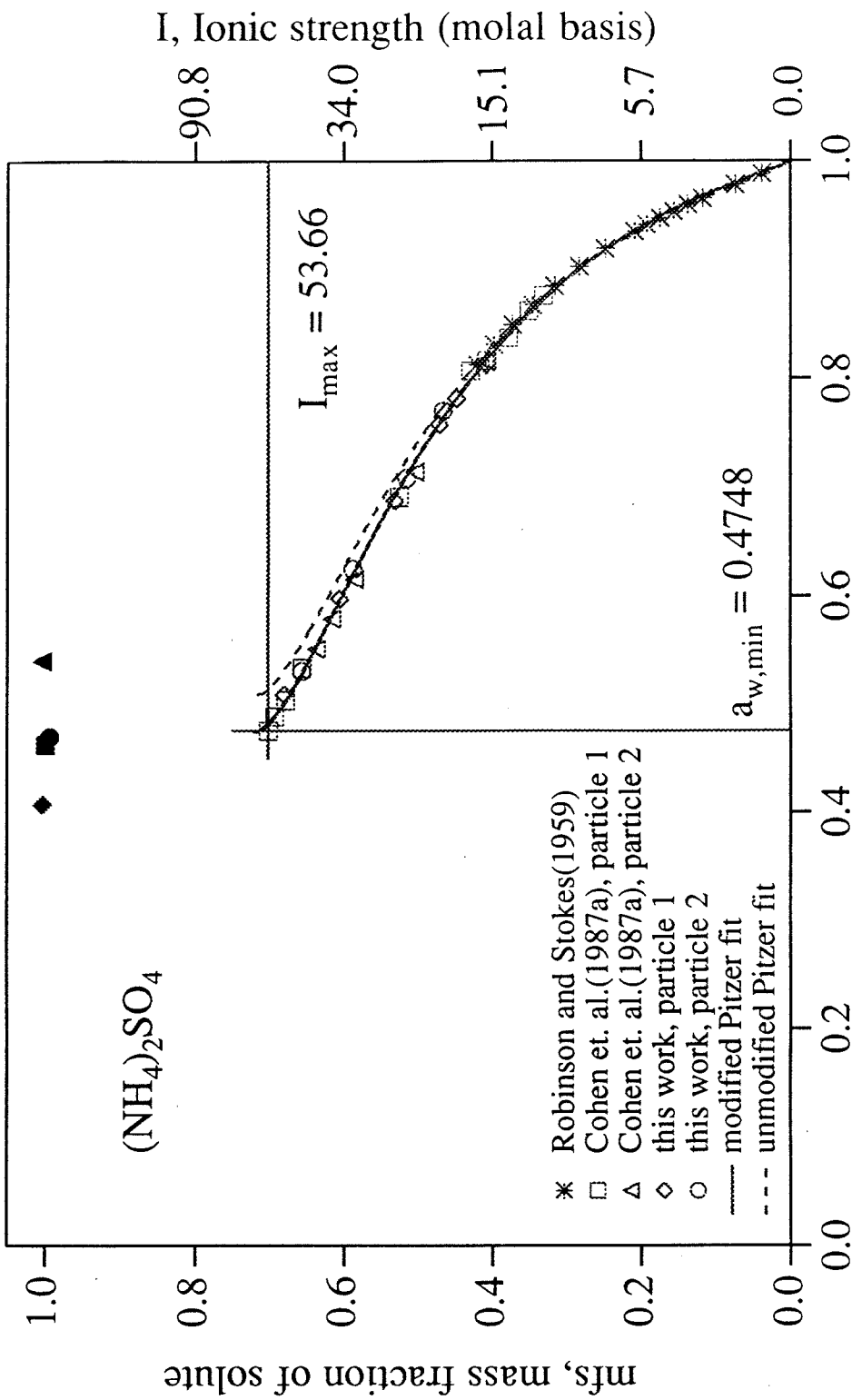


Figure 3: Water activity data for ammonium sulfate solutions

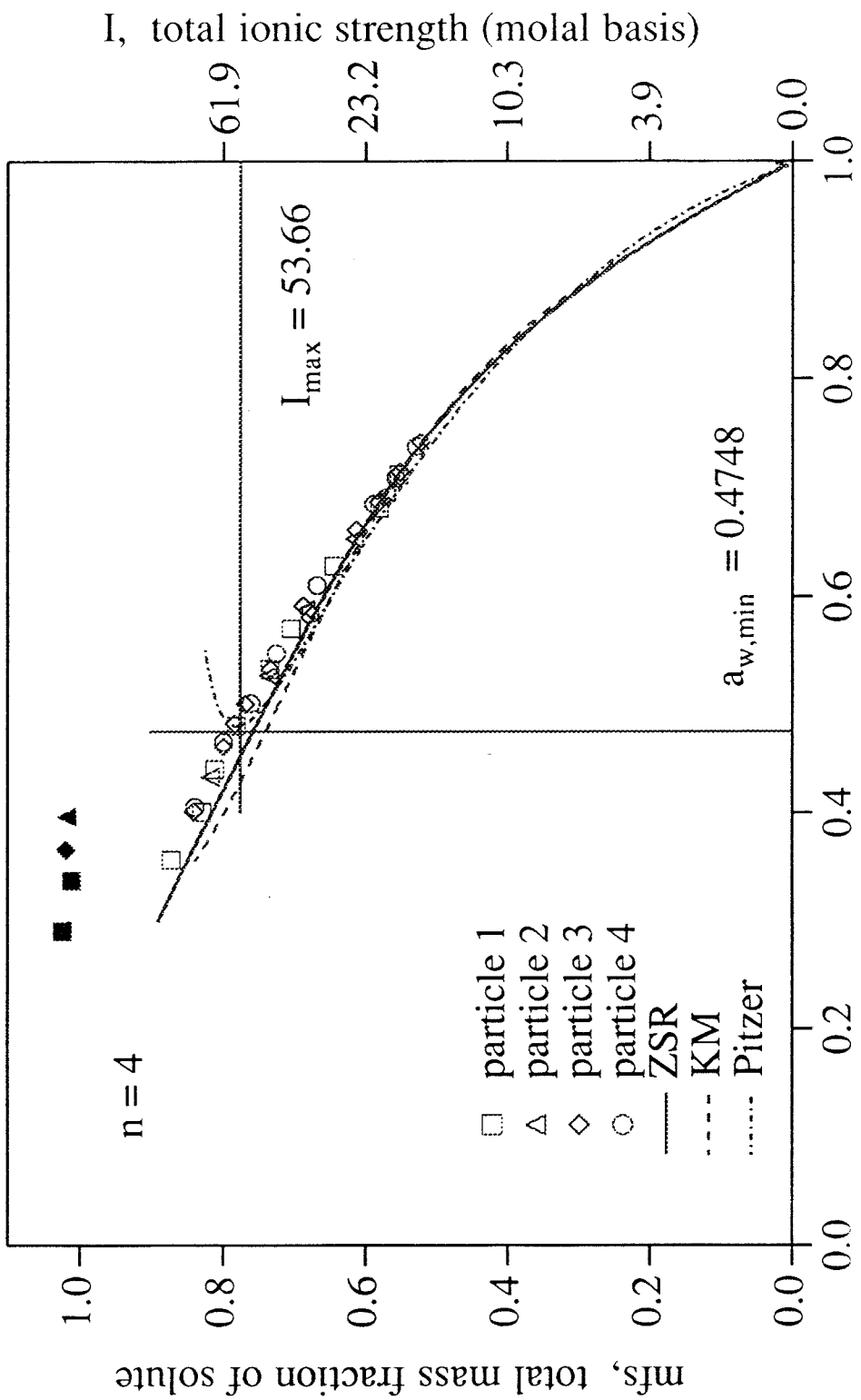


Figure 4: Water activity data for mixed solutions of nitrate/sulfate mole ratio of 4

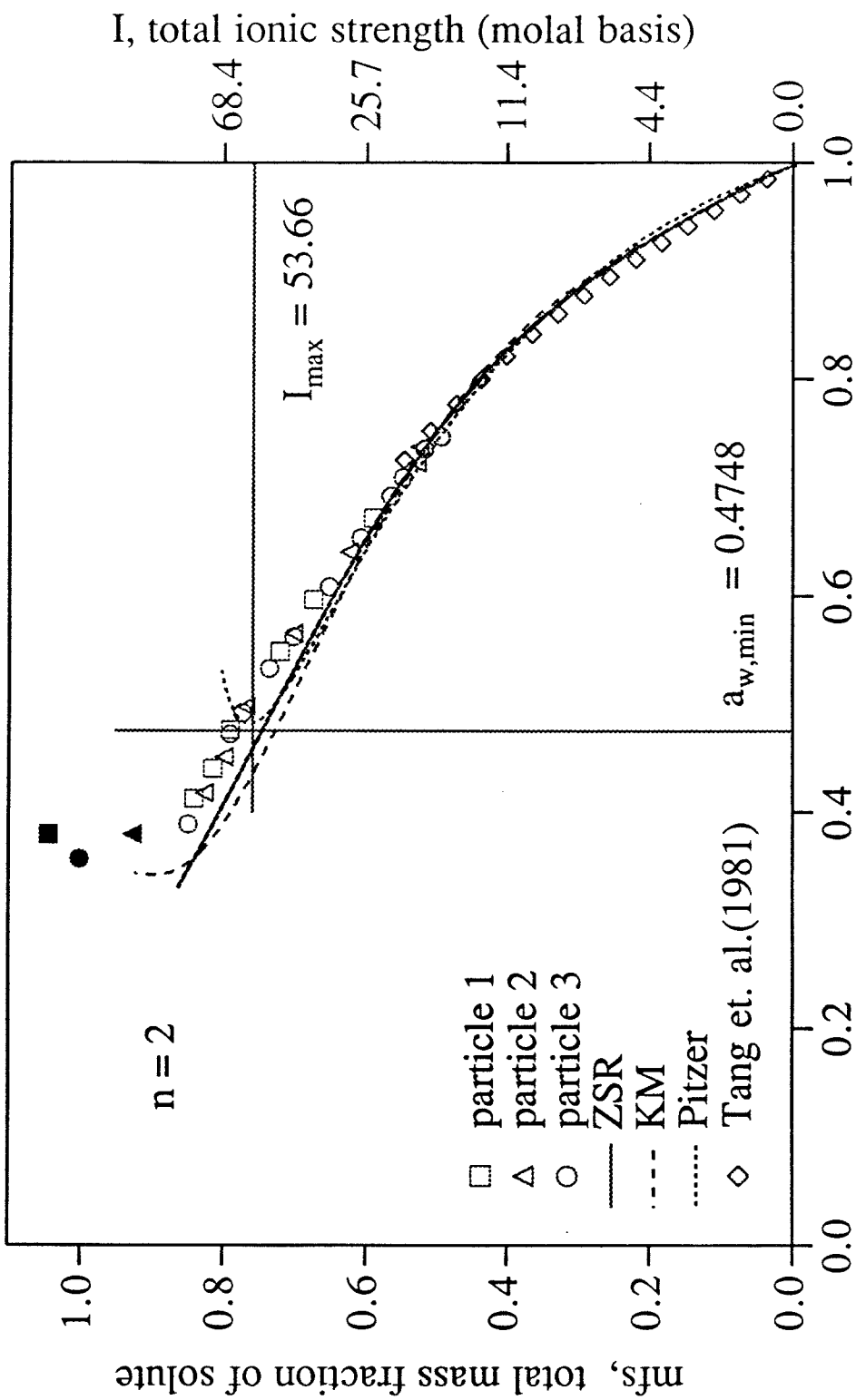


Figure 5: Water activity data for mixed solutions of nitrate/sulfate mole ratio of 2

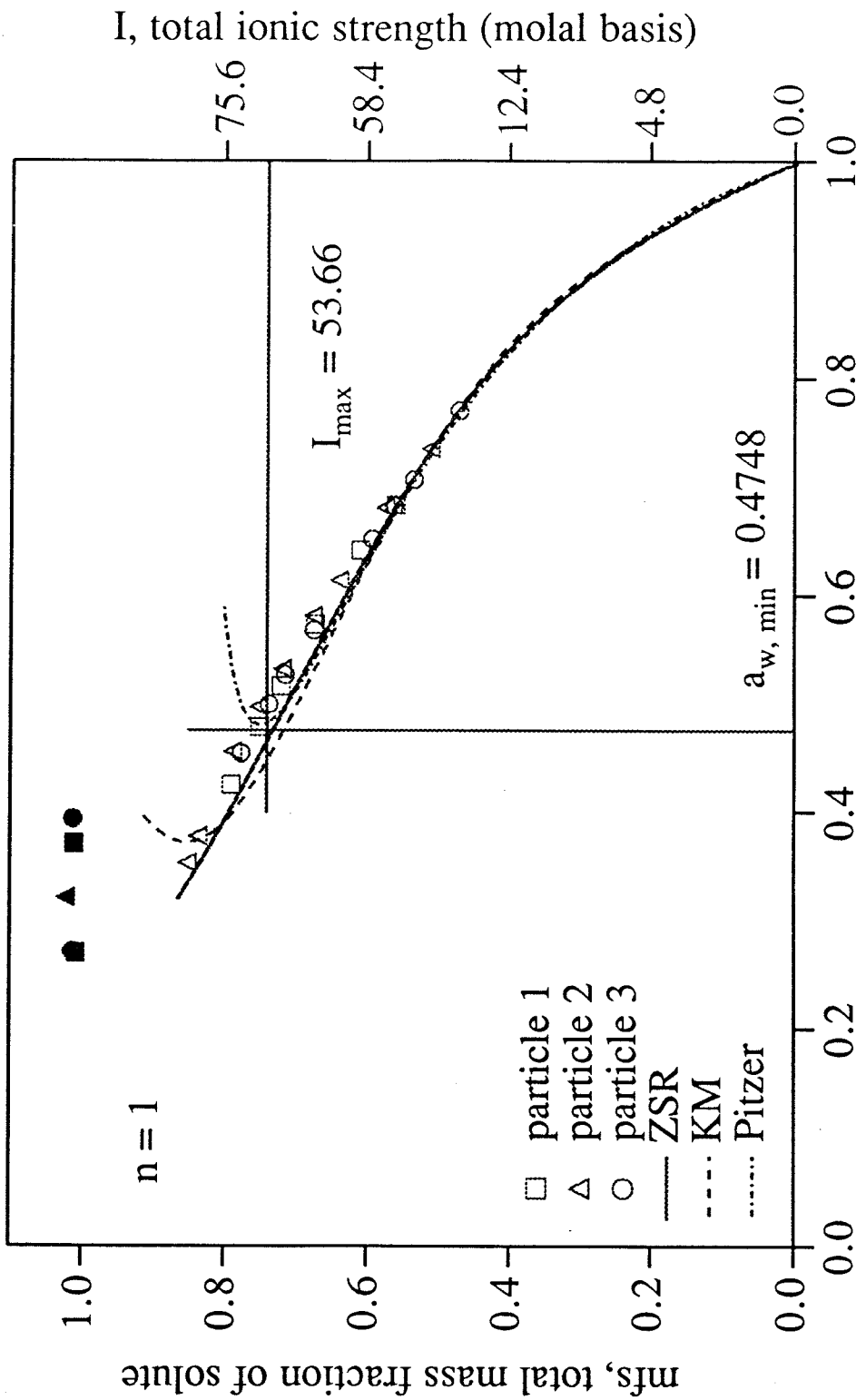


Figure 6: Water activity data for mixed solutions of nitrate/sulfate mole ratio of 1

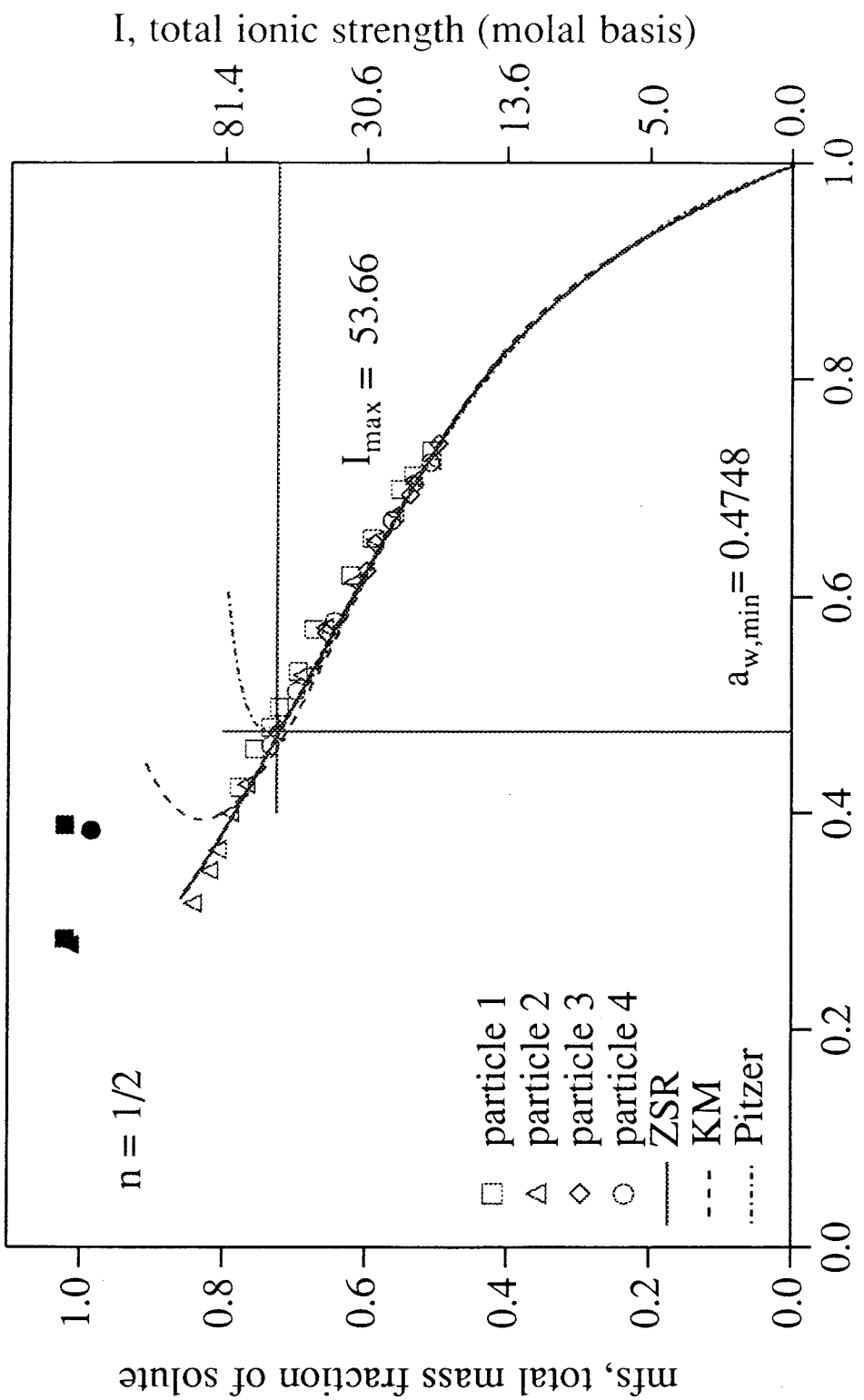


Figure 7: Water activity data for mixed solutions of nitrate/sulfate mole ratio of 1/2

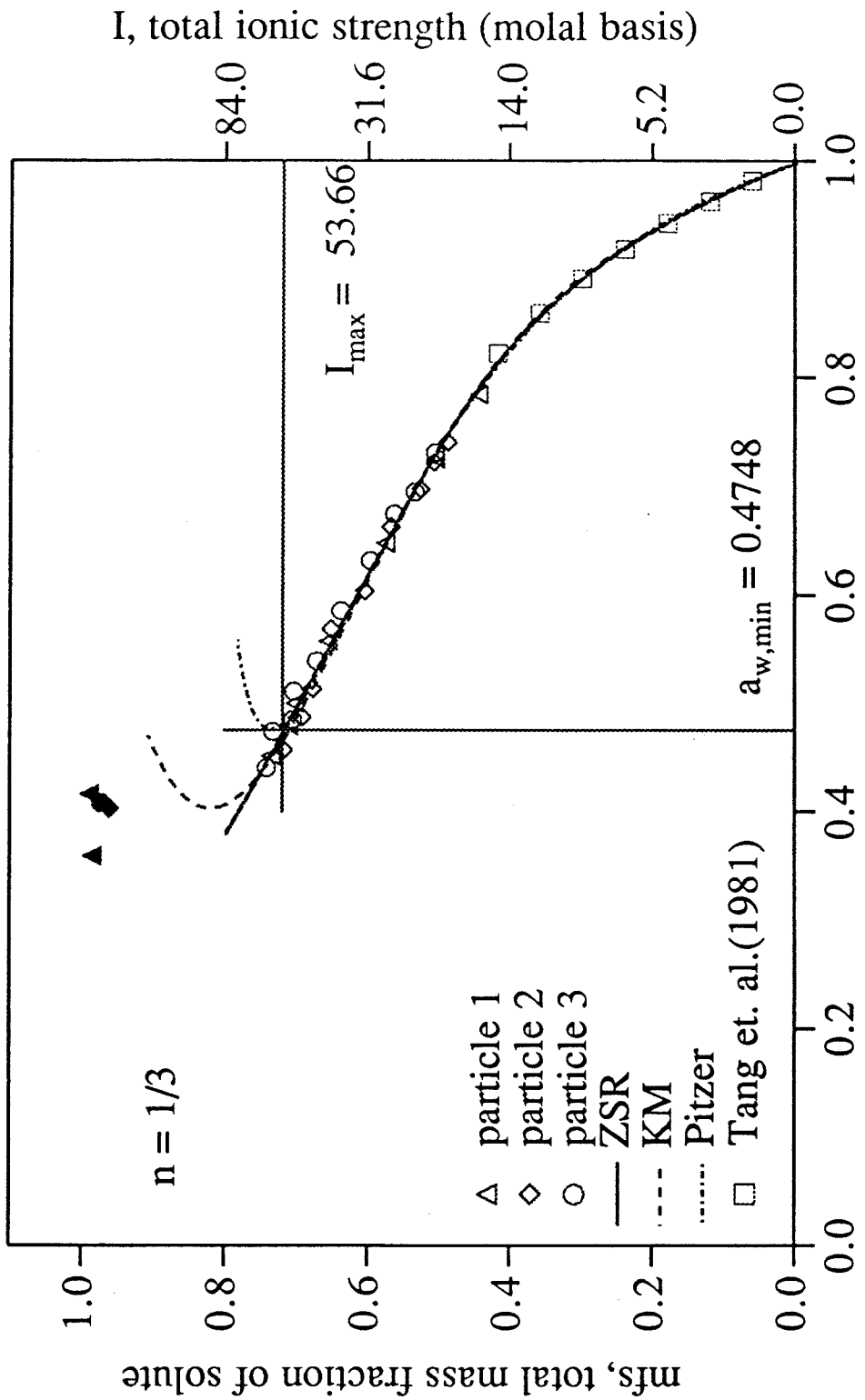


Figure 8: Water activity data for mixed solutions of nitrate/sulfate mole ratio of 1/3

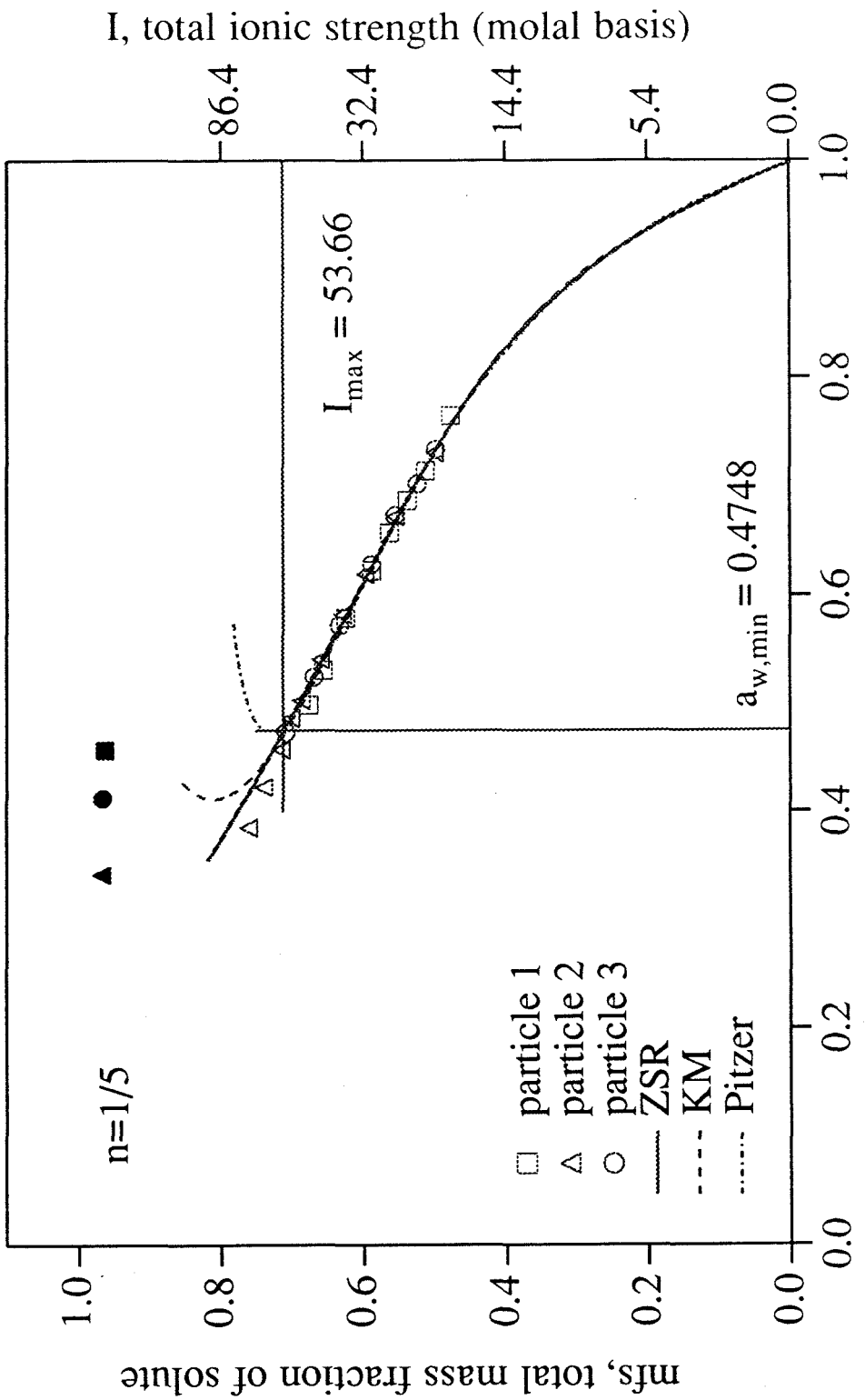


Figure 9: Water activity data for mixed solutions of nitrate/sulfate mole ratio of 1/5

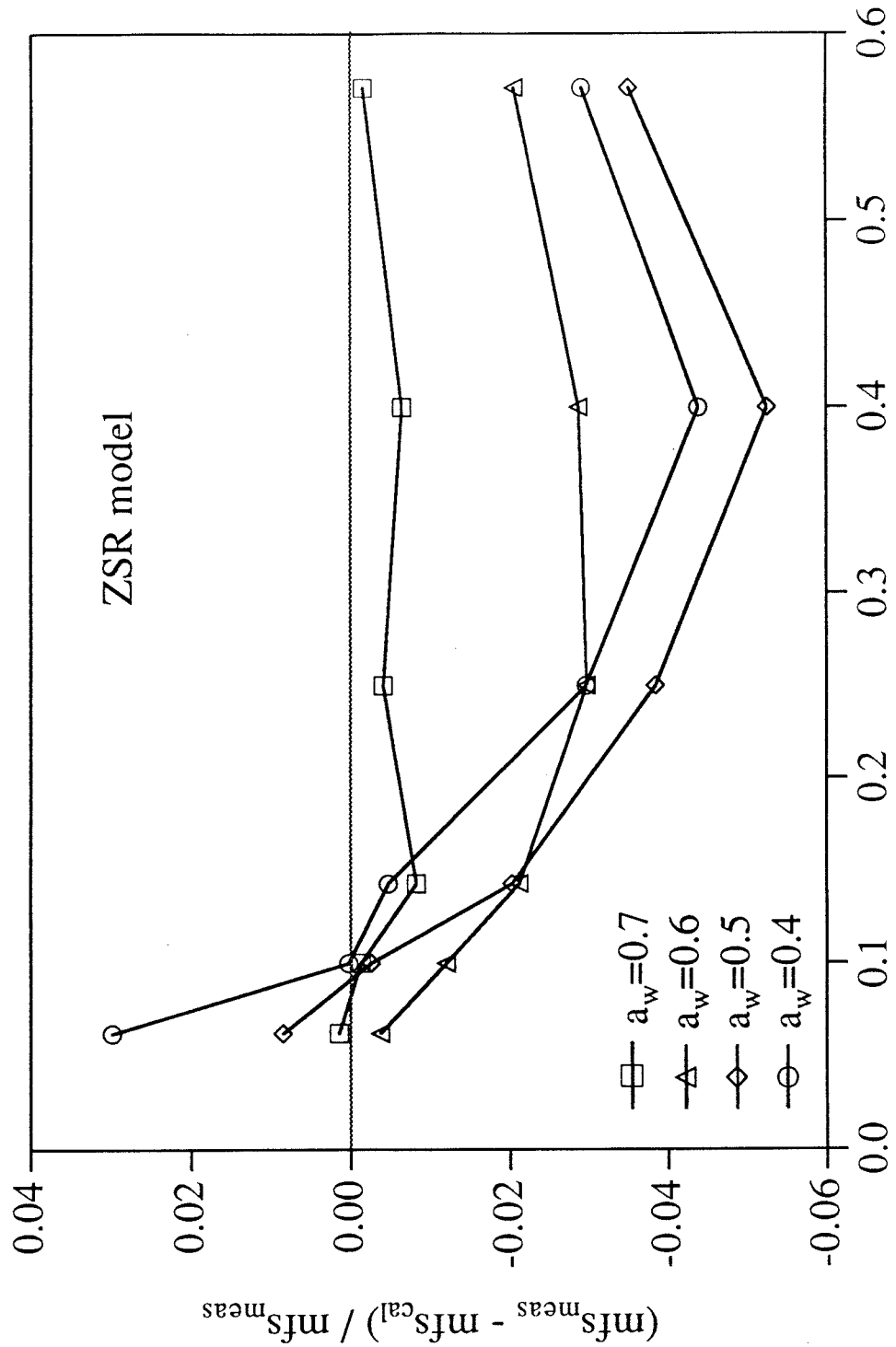


Figure 10: Relative deviations in mfs of the ZSR model from experimental data

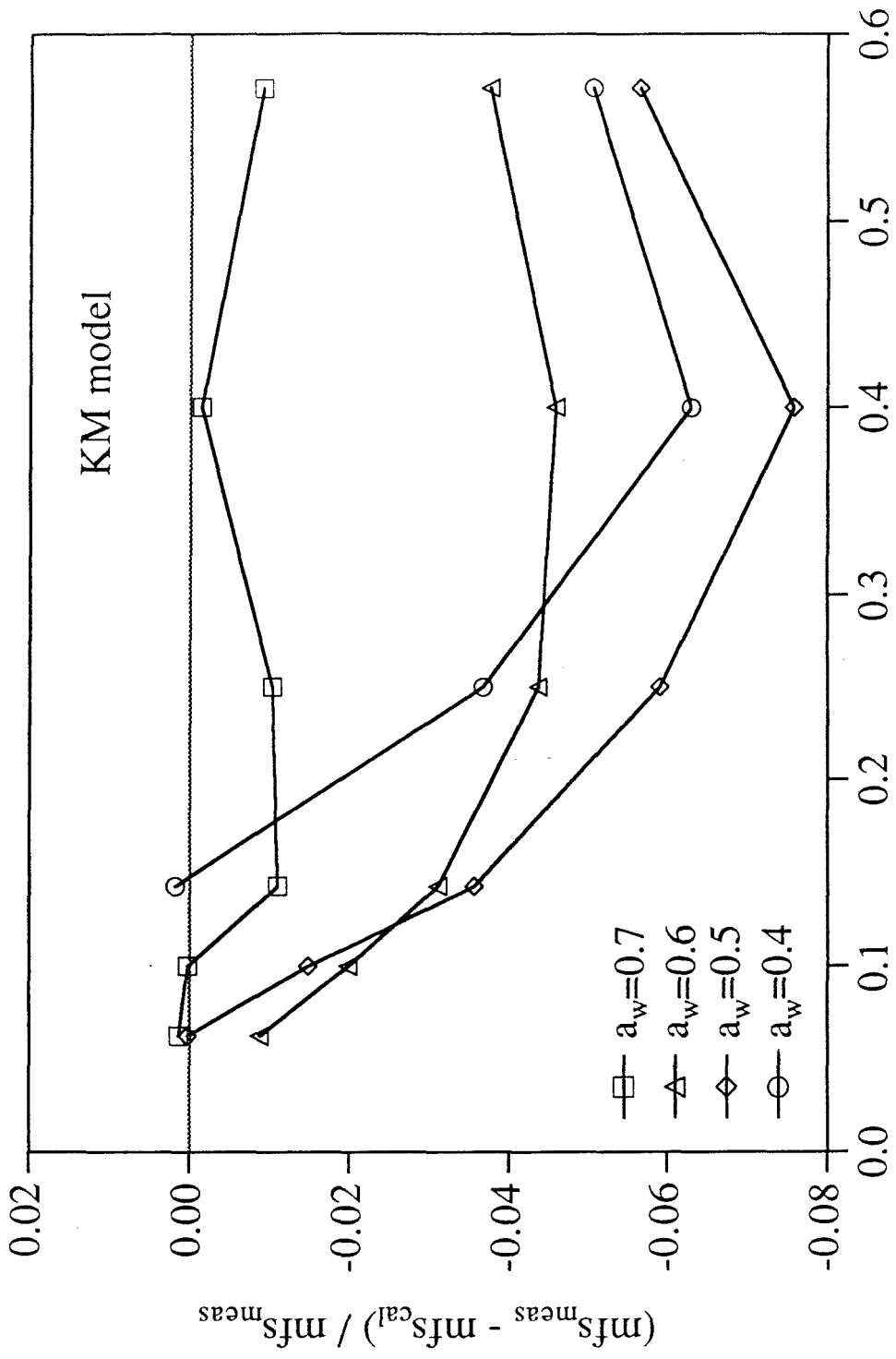


Figure 11: Relative deviations in mfs of the KM model from experimental data

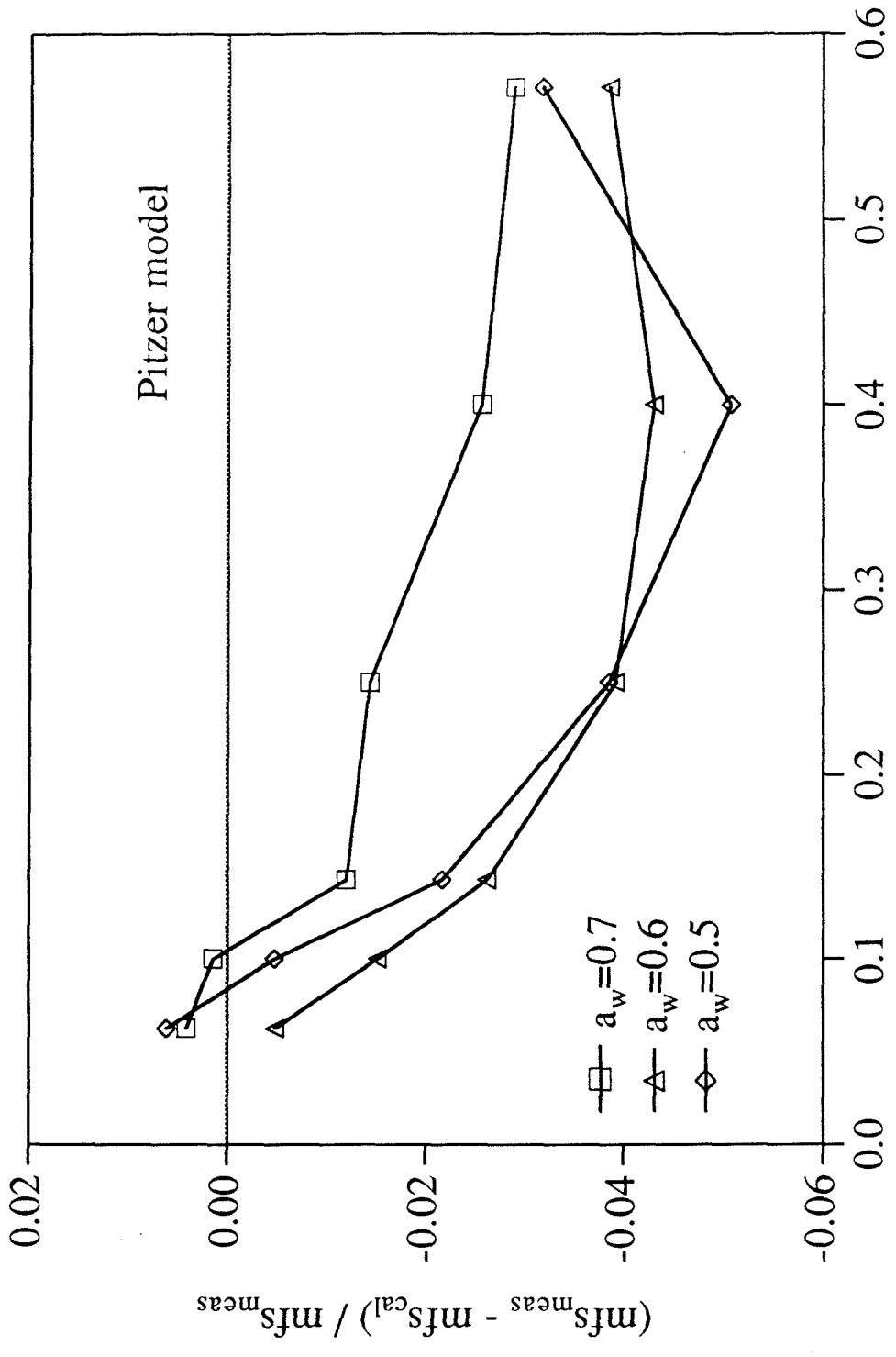


Figure 12: Relative deviations in mfs of the Pitzer model from experimental data

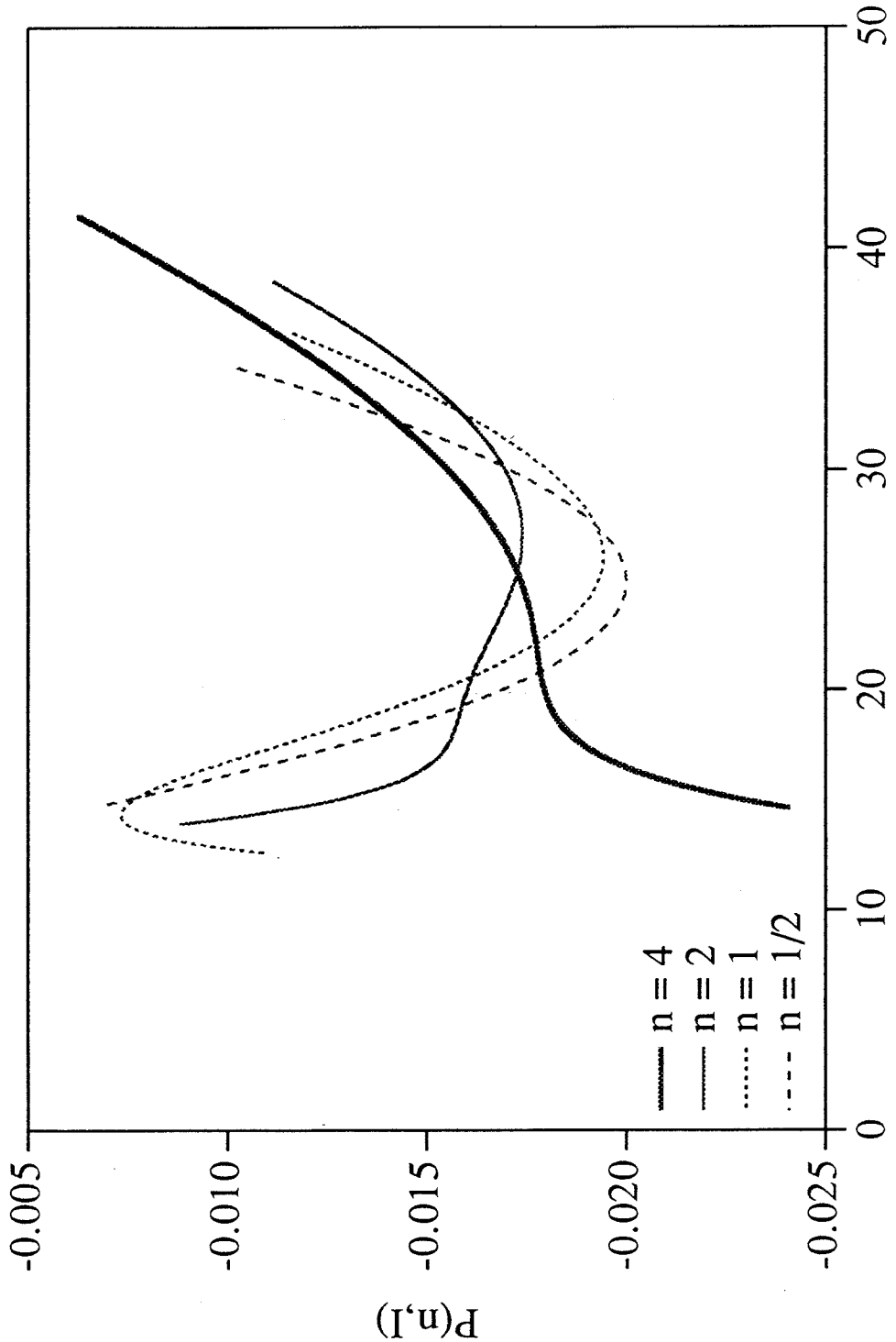


Figure 13: Characterization of the binary and ternary solute - solute interaction parameters of the full Pitzer model

# Chapter 4

# Conclusions

The electrodynamic balance is a very unique and versatile device to study single particles. *In-situ* measurements of particles in a well characterized and controlled environment are possible. Supersaturated solutions can also be studied. In this research, its applications in studying light scattering, water activities and evaporation kinetics of single droplets are demonstrated. In particular, we have looked into the Raman scattering of microspheres, with an aim of studying reactions occurring in microdroplets. Different types of size dependent optical resonance structures were identified in elastic and Raman scattering. The strongest Raman signal received was due to internal resonance of the excitation beam, giving similar enhancements to all Raman emissions. The intensity ratio of various Raman active components can then be used as a probe to semi-quantitatively characterize droplet compositions.

The electrodynamic balance is also well suited for studying the compositional effects of water activity of aqueous droplets. An atmospherically important system of $NH_4NO_3/(NH_4)_2SO_4/H_2O$ was studied. The compositional water activity data would be useful for future modeling of the thermodynamic and transport properties of atmospheric aerosols. They were also used to evaluate the performance of three commonly used mixed electrolyte models: the Zdanovskii-Strokes-Robinson model, the Kusik and Meissner model, and the Pitzer model. They all predict droplet concentrations in mass fractions to a few percents error within the range where water activity data of single electrolytes are available. These error margins are probably much smaller than the

uncertainty in field measurements of compositions of atmospheric aerosol particles. This suggests that these three models might be used for estimation of the compositional dependence of more complex atmospheric aerosol droplets on ambient relative humidity.

Evaporation/Condensation study of droplets is another major application of the electrodynamic balance. We studied the drying of various ceramic precursor solution droplets and devised an approach to study rapid evaporation of droplets in a time scale of a few seconds. These studies made use of an electro-optical system to follow the mass change of the droplet. Light scattering for *in-situ* size determination is another alternative. However, it requires more complicated and detailed curve fitting procedures and therefore is not used. However, for extremely slow evaporation process, *e.g.*, evaporation of $NH_4NO_3$ from its aqueous solution, light scattering (Mie resonance) technique may be employed since only a minute change in particle size is sufficient to give enough change in light scattering intensity whereas at least 10% change in mass is required to give accurate measurement for evaporation studies.

This research has demonstrated the versatility and uniqueness of the electrodynamic balance in the studies of aerosol particles. However, the electrodynamic balance has its own limitations. Unlike bulk sample studies where one can transfer the sample collected on filters to various equipments for further characterizations (*e.g.*, TEM analysis), there are limitations on the types of analyses one can apply on a levitated particle in an electrodynamic balance. A major contribution of the electrodynamic balance would be to study a variety of chemical reactions occurring in droplets. Raman spectroscopy

apparently is only good as a semi-quantitative tool because of the complication of Mie resonances. In my opinion, further research and courageous attempts to find a good method to accurately and efficiently determine the chemical compositions of droplets are warranted.

Appendix 1

**Quantitative determination of chemical composition of droplets using Raman Spectroscopy**

In the quantitative determination of chemical compositions of a spherical droplet using Raman spectroscopy, resonance structures can complicate the analyses of the measured Raman spectra in various ways as described in Chapter 2. One of the important conclusions was that the strongest signal measured were due to internal resonance of the excitation source, giving similar Raman enhancements of the nitrate and the water peaks. Therefore, the Raman nitrate intensity was roughly linear to the Raman water intensity of an evaporating droplet.

To determine the absolute concentration of a $NaNO_3$ droplet, one needs to investigate if the Raman nitrate/water signal ratio can be correlated to the nitrate/water mole ratio of the droplet. A "calibration" curve of $NaNO_3$ solution was obtained by measuring the Raman spectra of a $NaNO_3$ droplet at various concentrations. The concentration of the droplet was varied by changing the ambient relative humidity and was determined by measuring the DC balancing voltages. The integration time of each spectrum was 10 seconds. Figure A1.1 shows the Raman spectra of the droplet at concentrations below and above saturation. The spectra of the dried $NaNO_3$ particle and bulk water are also shown for comparisons. Qualitatively, the ratio of the nitrate peak at 1040 $cm^{-1}$ and water peak at 3200 to 3600 $cm^{-1}$ increases with solution concentration. Figure A1.2 plots the compositional dependence of the measured Raman nitrate/water ratio of two different droplets. The Raman nitrate/water

ratio is roughly proportional to the molality of the droplet. It should be noted that the concentration of saturated $NaNO_3$ solution at room temperature is about 10 M. The isolation of the droplet from any foreign surface suppressed any heterogeneous nucleation of the droplet and therefore a high supersaturation ratio of around 2.5 was achieved.

As a result of laser heating of the droplet, a minute amount of water evaporated from the droplet during the Raman measurement at each concentration. The mass change before and after each measurement was smaller than 1%. However, the corresponding size change was large enough to cause Raman scattering to exhibit resonance behaviors. In every Raman scan, the Raman scattering signal measured was an integrated signal of a slowly evaporating droplet as observed in Chapter 2. This integrated intensity was mainly attributed to the Raman emissions caused by the internal resonance of the excitation beam. Similar intensity enhancements occurred in all Raman emissions. Therefore, the Raman nitrate/water intensity ratio of each spectrum scan was an indicative of the concentration of the droplet and was linearly related to the molality. The Raman nitrate/water ratio can be used to determine the concentration of a sodium nitrate droplet albeit at a low accuracy. Reactions involving orders of magnitude change in concentration can be studied with Raman spectroscopy using the Raman peak ratios to determine concentrations.

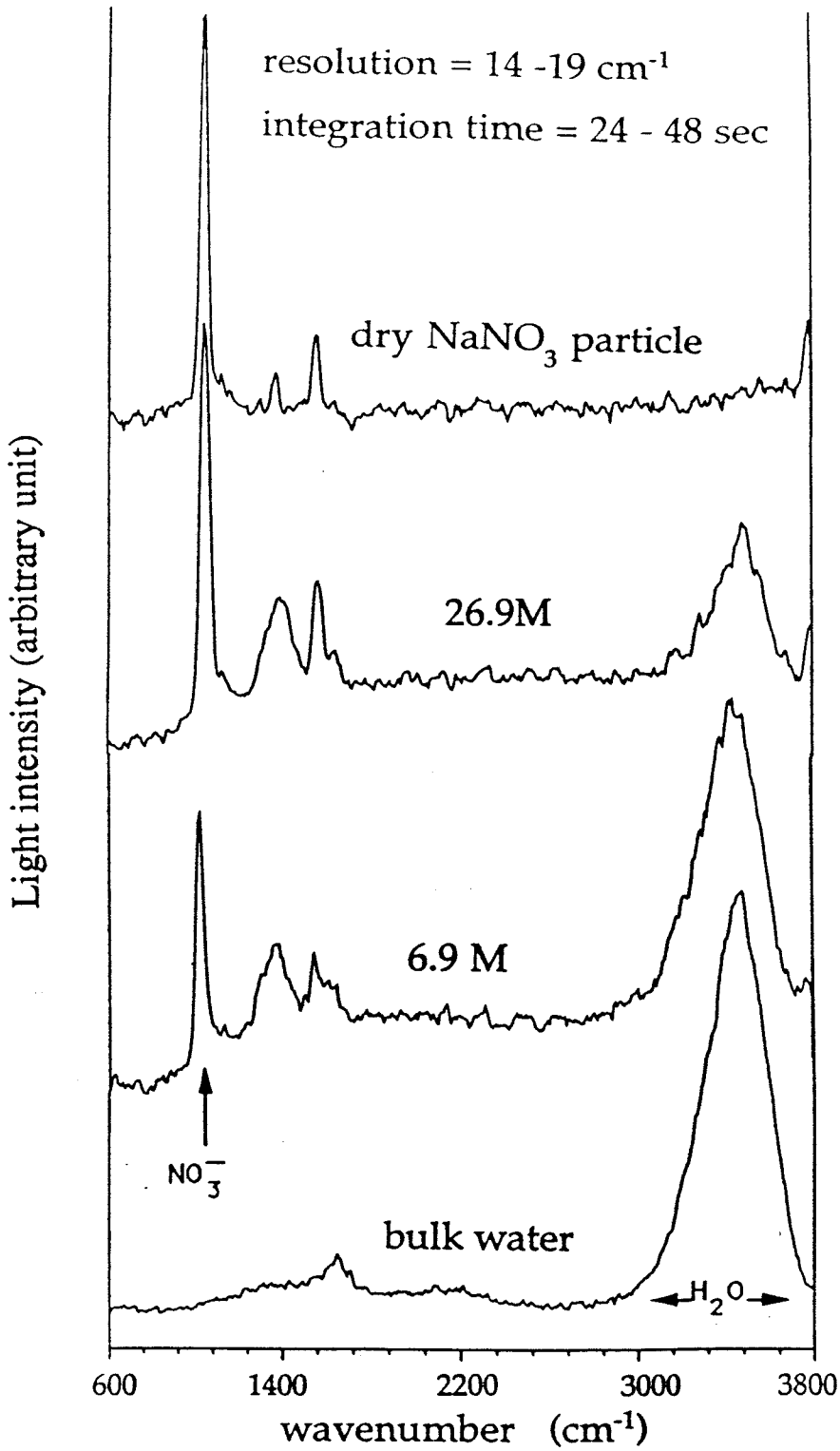


Figure A1.1: Raman spectra of a $NaNO_3$ droplet at various concentrations

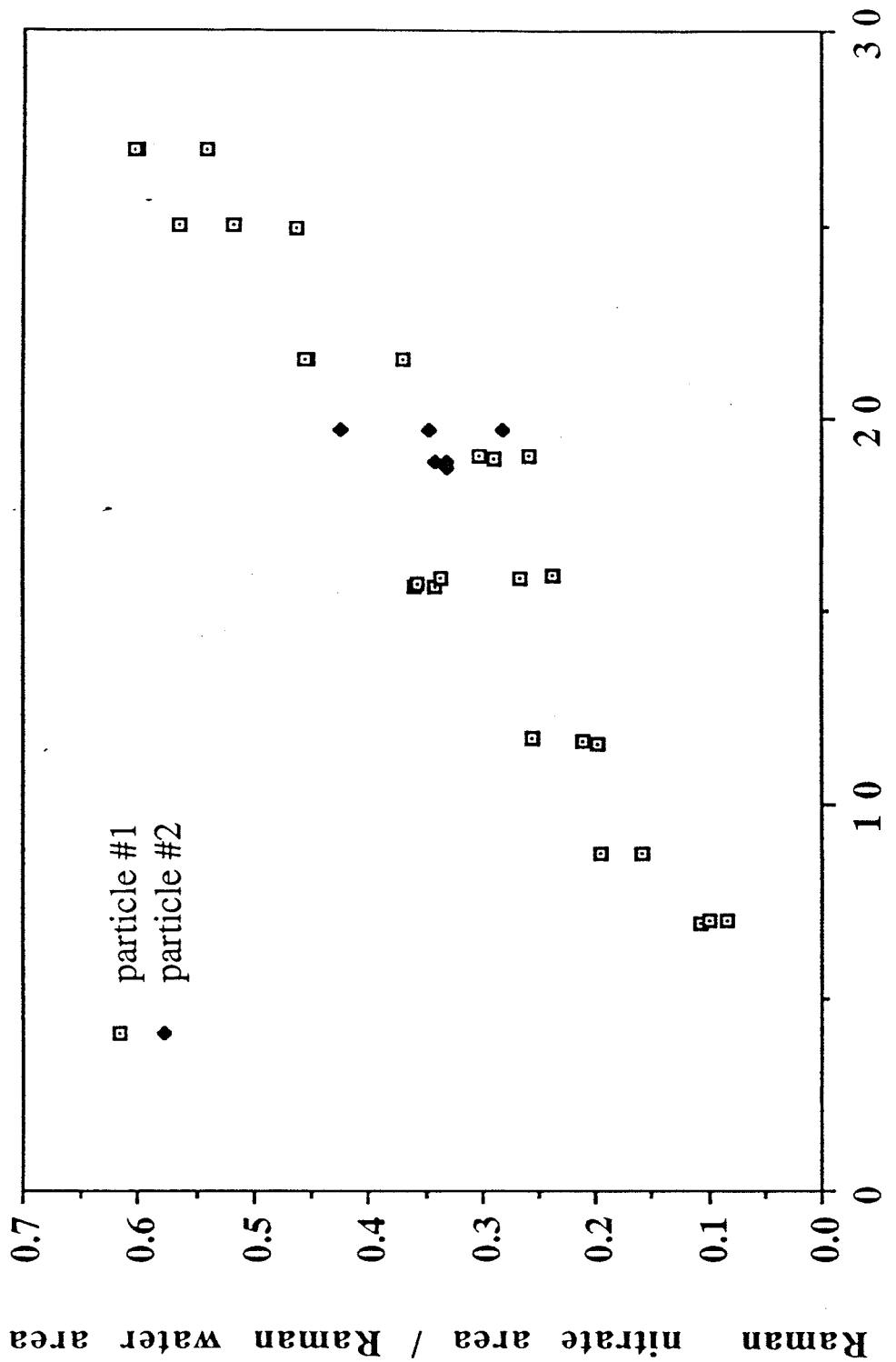


Figure A1.2: Quantitative Chemical Characterization of $NaNO_3$ droplets using Raman Spectroscopy

Appendix 2:

**The design of the Spherical Void Electrodynamic Levitator(SVEL)**

In this section, we will describe in detail the design of the Spherical Void Electrodynamic Levitator(SVEL) used in the measurements of water activities of mixed $NH_4NO_3/(NH_4)_2SO_4$ aqueous droplets in Chapter 3. The design of the SVEL is similar to that described by Arnold and Folan (1978). Similar to the conventional electrodynamic balance used in the light scattering experiment in Chapter 2, the SVEL consists of two endcaps and a ring electrode as depicted in Figure A2.1. DC potentials are applied to the endcaps whereas AC field is applied to the ring. The electrodes form a spherical void and are separated by Mylar pieces of thickness 0.004". The ability to trap a charge particle is a function of the angle $\theta$. When $\theta$ equals to $\cos^{-1}(1/\sqrt{3})$, the focusing force on the particle at the center is the greatest. The balance has 4 optical windows and 4 flow access openings on the ring. On the top electrode, an opening is made for droplet injection. An identical opening is also made at the bottom electrode for optical and flow access. This SVEL is designed to reduce the time to establish a new ambient environment of a levitated particle. The void has a diameter of 3/4" which gives a residence time of about 10 sec when gas flows through at a rate of 0.4 ml/sec as used in the water activity experiment in Chapter 3. Gas flowed into the spherical void from the bottom electrode and left through the top electrode. The openings of the ring electrode were not used and therefore blocked in our experiments. Teflon fittings were used to avoid electric shocks. Since the AC applied on the ring could be as high as 1000 Volts, a Lucite box was used to cover the balance. Temperature control was attempted by surrounding the SVEL with copper coils in which water at 25°C flowed through.

To further avoid any temperature drift due to wind current, the whole setup was enclosed in a Lucite box. Temperature was stabilized to ± 0.5°C.

The field equations due to the AC potential on the ring were determined by Arnold and Folan (1987). They also stated that the DC field at the center of the spherical void was $-V_o/a$, where $2V_o$ and $a$ were the potential difference across the endcap electrodes and the radius of the spherical void, respectively. In the following, we will derive the field equations due to the DC potential applied on the endcap electrodes and calculate the DC potential at the center of the spherical void.

The potential inside the spherical void is governed by Laplace's equation

$$\nabla^2 V = 0 \tag{A2.1}$$

subject to the boundary conditions depicted in Figure A2.1 and the finiteness of $V$ at the center of the spherical void. The solution can be expressed in spherical coordinates as

$$V = \sum_{n=0}^{\infty} A_n \left(\frac{r}{a}\right)^n P_n(x) \ , \tag{A2.2}$$

where $x = cos\ \theta$ and $P_n$ is the Lengendre's polynomials of first kind at order $n$. The boundary conditions can be described by

$$f(x) = \begin{cases} +V_o & \text{at } x > 1/\sqrt{3} \\ 0 & \text{at } |x| > -1/\sqrt{3} \\ -V_o & \text{at } -1/\sqrt{3} > x \end{cases} . \tag{A2.3}$$

Since $f(x)$ is piecewise continuous, it can be also expressed as

$$f(x) = \sum_{n=0}^{\infty} A_n P_n(x) \; . \tag{A2.4}$$

The value of the coefficient $A_n$ can be obtained by multiplying both sides of Eq. (A2.4) by $P_n(x)$ and integrate from $x=-1$ to $x=1$. Using the orthogonal properties of $P_n(x)$, one obtains

$$A_n = \begin{array}{ll} (2n+1)\, V_o B_n & \text{when } n = \text{odd} \\ 0 & \text{when } n = \text{even,} \end{array} \tag{A2.5}$$

where $B_n = \int_{1/\sqrt{3}}^{1} P_n(x)\, dx$. Substituting $A_n$ into Equation A2.2,

$$V = V_o \sum_{n=1}^{\infty}{}' (2n+1) \mathrm{B}_n \left(\frac{r}{a}\right)^n P_n(x) \; . \tag{A2.6}$$

The prime in the above summation means that only odd terms are taken. The electric field is related to the potential by

$$E = - \nabla V \; . \tag{A2.7}$$

The vertical component of the DC field in the spherical void is then

$$E_z = (x^2 - 1) \frac{V_o}{r} \sum_{n=1}^{\infty}{}' (2n+1)\, B_n \left(\frac{r}{a}\right)^n \frac{dP_n(x)}{dx}$$

$$- \; x V_o \sum_{n=1}^{\infty}{}' (2n+1)\, \frac{n}{a} \left(\frac{r}{a}\right)^{n-1} P_n(x) \; . \tag{A2.8}$$

At the center of the balance where $x=1$ and $r=0$,

$$E_z = \frac{3 V_o B_1}{a} P_1(1) \qquad \text{(A2.9)}$$
$$= - \frac{V_o}{a} \ .$$

Since there are openings for optical and flow access on the electrodes, the actual field strength should be

$$E_z = - c \frac{V_o}{a} \ , \qquad \text{(A2.10)}$$

where $c$ is a geometric constant of the spherical void and needs to be calibrated experimentally if absolute mass of the particle are required. $c$ was not determined since only the relative mass (concentration) was required in our studies of the compositional dependence of water activity of $NH_4NO_3/(NH_4)_2SO_4$ solutions in Chapter 3.

**Reference**

Arnold S. and Folan L. M. "Spherical void electrodynamic levitator," Rev. Sci. Instrum. 58(9), 1732-1735, 1987.

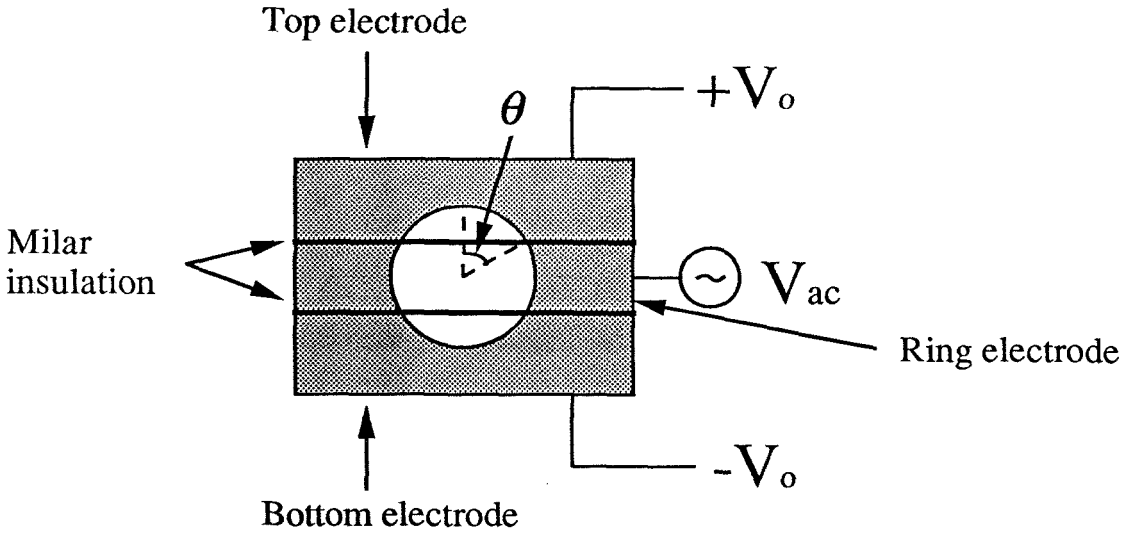


a: Geometric configuration of the SVEL

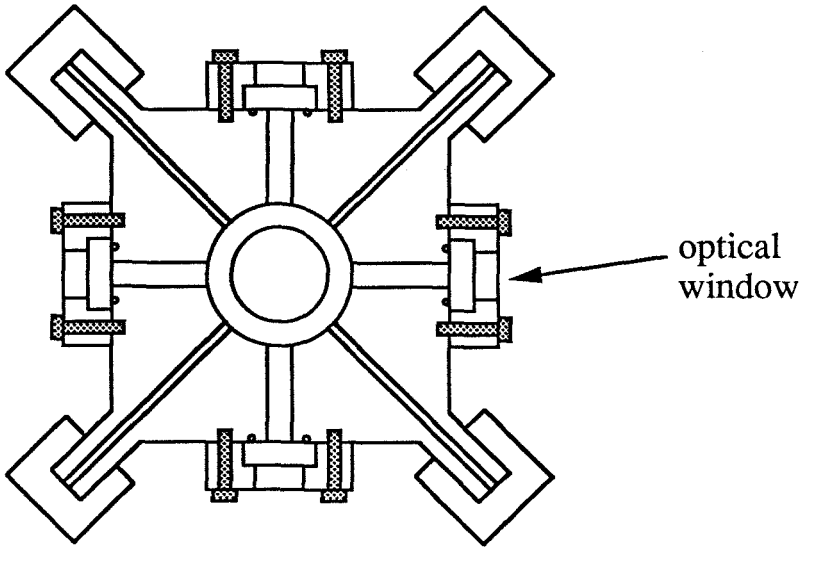


b: top view of the ring electrode of the SVEL

Figure A2.1: *Design of the Spherical Void Electrodynamic Levitator (SVEL)*

## Appendix 3

## Raw data of the measurements of water activities of $NH_4NO_3/(NH_4)_2SO_4$ solutions

In the studies of water activities of $NH_4NO_3/(NH_4)_2SO_4$ solutions reported in Chapter 3, the total mass fraction of solute ($mfs$) of droplets at equilibrium with the ambient relative humidity ($rh$) was required. The ambient relative humidity was monitored by measuring the dew point ($T_{DP}$) of the gas flowing into the spherical void electrodynamic levitator and the ambient temperature ($T$) using a dew point meter (EG&G model 911). The calibration of the dew point and the ambient temperature measurements are

$$T_{DP}(^{\circ}C) = -44.445 + 11.089 DP(v) \qquad \text{(A3.1)}$$

$$T(^{\circ}C) = 9.99\, T_{amb}(v) - 39.55 \ , \qquad \text{(A3.2)}$$

where $DP(v)$ and $T_{amb}(v)$ are the voltage readings for the dew point and the ambient temperature, respectively, from the same dew point meter. The relative humidity ($rh$) is the ratio of the system water vapor to the saturated water vapor pressure at the ambient temperature $T$,

$$rh \equiv \frac{P_{H_2O}}{P^{sat}_{H_2O}(T)} = \frac{P^{sat}_{H_2O}(T_{DP})}{P^{sat}_{H_2O}(T)} \ . \qquad \text{(A3.3)}$$

The temperature dependence of the saturated water vapor pressure can be described by the Antoine's equation,

$$lnP^{sat}_{H_2O}(T) = -\frac{5313.88}{273.15 + T} + 20.988 \quad (mmHg)\ . \tag{A3.4}$$

By combining Equations (A3.1) to (A3.4), the relative humidity can be obtained using the measured readings of $DP(v)$ and $T_{amb}(v)$.

To avoid the uncertainty in the composition of the dried particle formed from crystallization of a mixed droplet, a droplet at high relative humidity was used as a reference to determine the *mfs* at each concentration. The *DC* voltage would be required to balance a completely water free dried solute particle, $DC_{dry}$, was calculated from the *DC* balancing voltage and the concentration of the reference droplet. The *mfs* of a droplet at each concentration was determined by its *DC* balancing voltage

$$DC_{dry} = DC_{ref} \bullet mfs_{ref} \tag{A3.5}$$

$$mfs = \frac{DC_{dry}}{DC_{meas}}\ , \tag{A3.6}$$

where $DC_{ref}$ and $DC_{meas}$ are the balancing voltage of a droplet at the reference concentration and at the concentration of interest, respectively. The reference concentration ($mfs_{ref}$) was estimated by the Zdanovskii-Stokes-Robinson (ZSR) model.

In Tables A3.1 to A3.8, the raw data of dew point reading ($DP(v)$), the ambient temperature reading ($T_{amb}(v)$), and the balancing voltage ($DC(v)$) of $NH_4NO_3$/ $(NH_4)_2SO_4$ droplets at various nitrate/sulfate mole ratio ($n$) are tabulated. The calculated *rh* and *mfs* and the physical states of these particles (dry or wet) are

also indicated. Since the ZSR model requires water activity of single electrolyte solutions, the corresponding data for $NH_4NO_3$ and $(NH_4)_2SO_4$ solutions are also presented. The data of the reference concentration of each particle are shown in bold face. No accurate size measurement of individual droplets was made. However, they were all in the range of 20 to 40 $\mu$m in diameter when viewed using the optical microscope.

**Table A3.1: Raw data of water activity measurements of ammonium nitrate solutions**

particle 1

| Point | DP(v) | Tamb(v) | DC(v) | rh | mfs | dry/wet |
|---|---|---|---|---|---|---|
| 1 | 5.769 | 6.447 | 22.614 | 0.7228 | 0.5659 | w |
| 2 | 5.624 | 6.460 | 19.686 | 0.6488 | 0.6501 | w |
| 3 | 5.489 | 6.447 | 18.269 | 0.5949 | 0.7005 | w |
| 4 | 5.344 | 6.453 | 17.140 | 0.5351 | 0.7469 | w |
| 5 | 5.137 | 6.448 | 15.973 | 0.4627 | 0.8013 | w |
| 6 | 5.001 | 6.446 | 15.507 | 0.4197 | 0.8253 | w |
| 7 | 4.845 | 6.447 | 14.962 | 0.3741 | 0.8554 | w |
| 8 | 4.697 | 6.456 | 14.425 | 0.3330 | 0.8872 | w |
| **9** | **5.806** | **6.487** | **22.909** | **0.7289** | **0.5587** | w |
| 10 | 4.448 | 6.440 | 12.634 | 0.2789 | 0.9980 | d |

particle 2

| Point | DP(v) | Tamb(v) | DC(v) | rh | mfs | dry/wet |
|---|---|---|---|---|---|---|
| **1** | **5.881** | **6.443** | **40.220** | **0.7823** | **0.4767** | w |
| 2 | 5.811 | 6.453 | 37.030 | 0.7413 | 0.5177 | w |
| 3 | 5.611 | 6.444 | 30.413 | 0.6491 | 0.6304 | w |
| 4 | 5.256 | 6.452 | 25.361 | 0.5028 | 0.7559 | w |
| 5 | 4.792 | 6.453 | 22.400 | 0.3584 | 0.8559 | w |
| 6 | 4.959 | 6.452 | 23.090 | 0.4056 | 0.8303 | w |
| 7 | 5.134 | 6.461 | 23.981 | 0.4581 | 0.7994 | w |
| 8 | 5.435 | 6.468 | 26.794 | 0.5656 | 0.7155 | w |
| 9 | 5.716 | 6.468 | 32.090 | 0.6882 | 0.5974 | w |
| 10 | 4.664 | 6.481 | 21.515 | 0.3204 | 0.8911 | w |
| 11 | 4.353 | 6.481 | 18.995 | 0.2530 | 1.0093 | d |

particle 3

| Point | DP(v) | Tamb(v) | DC(v) | rh | mfs | dry/wet |
|---|---|---|---|---|---|---|
| **1** | **5.890** | **6.448** | **24.436** | **0.7662** | **0.5010** | w |
| 2 | 5.734 | 6.483 | 20.413 | 0.6906 | 0.5997 | w |
| 3 | 5.295 | 6.496 | 16.142 | 0.5036 | 0.7584 | w |
| 4 | 5.110 | 6.489 | 15.281 | 0.4428 | 0.8011 | w |
| 5 | 4.915 | 6.493 | 14.574 | 0.3832 | 0.8400 | w |
| 6 | 4.775 | 6.500 | 14.190 | 0.3441 | 0.8627 | w |
| 7 | 4.574 | 6.492 | 13.093 | 0.2974 | 0.9349 | d |

**Table A3.2:**
**Raw data of water activity measurements of ammonium sulfate solutions**

particle 1

| Point | DP(v) | Tamb(v) | DC(v) | rh | mfs | dry/wet |
|---|---|---|---|---|---|---|
| **1** | **5.906** | **6.415** | **22.699** | **0.8092** | **0.4246** | w |
| 2 | 5.855 | 6.416 | 21.478 | 0.7811 | 0.4488 | w |
| 3 | 5.800 | 6.405 | 20.429 | 0.7572 | 0.4718 | w |
| 4 | 5.660 | 6.405 | 18.127 | 0.6874 | 0.5317 | w |
| 5 | 5.465 | 6.413 | 15.902 | 0.5970 | 0.6061 | w |
| 6 | 5.230 | 6.402 | 14.1350 | 0.5086 | 0.6819 | w |
| 7 | 4.929 | 6.408 | 9.600 | 0.4073 | 1.0040 | d |

particle 2

| Point | DP(v) | Tamb(v) | DC(v) | rh | mfs | dry/wet |
|---|---|---|---|---|---|---|
| **1** | **5.902** | **6.420** | **27.709** | **0.8046** | **0.4299** | w |
| 2 | 5.829 | 6.410 | 25.530 | 0.7701 | 0.4666 | w |
| 3 | 5.711 | 6.415 | 23.101 | 0.7079 | 0.5157 | w |
| 4 | 5.533 | 6.416 | 20.246 | 0.6251 | 0.5884 | w |
| 5 | 5.311 | 6.429 | 18.110 | 0.5302 | 0.6578 | w |
| 6 | 5.137 | 6.423 | 11.975 | 0.4697 | 0.9948 | d |

**Table A3.3:**
**Raw data of water activity measurements of $NH_4NO_3/(NH_4)_2SO_4$ solutions at n=4**

particle 1

| point | DP(v) | Tamb(v) | DC(v) | rh | total mfs | dry/wet |
|---|---|---|---|---|---|---|
| **1** | **5.890** | **6.478** | **40.580** | **0.7708** | **0.4837** | w |
| 2 | 5.782 | 6.486 | 35.500 | 0.7125 | 0.5529 | w |
| 3 | 5.722 | 6.490 | 33.320 | 0.6820 | 0.5812 | w |
| 4 | 5.611 | 6.500 | 30.428 | 0.6278 | 0.6451 | w |
| 5 | 5.373 | 6.496 | 26.699 | 0.5324 | 0.7352 | w |
| 6 | 5.230 | 6.497 | 25.123 | 0.4805 | 0.7813 | w |
| 7 | 5.113 | 6.503 | 24.181 | 0.4401 | 0.8118 | w |
| 8 | 5.479 | 6.506 | 27.814 | 0.5703 | 0.7057 | w |
| 9 | 4.831 | 6.510 | 22.511 | 0.3566 | 0.8720 | w |
| 10 | 4.757 | 6.512 | 19.413 | 0.3371 | 1.0110 | d |
| 11 | 4.567 | 6.520 | 19.159 | 0.2910 | 1.0240 | d |

particle 2

| point | DP(v) | Tamb(v) | DC(v) | rh | total mfs | dry/wet |
|---|---|---|---|---|---|---|
| **1** | **5.838** | **6.491** | **25.001** | **0.7382** | **0.5247** | w |
| 2 | 5.760 | 6.500 | 22.996 | 0.6960 | 0.5705 | w |
| 3 | 5.670 | 6.502 | 21.292 | 0.6533 | 0.6161 | w |
| 4 | 5.521 | 6.504 | 19.155 | 0.5881 | 0.6848 | w |
| 5 | 5.369 | 6.509 | 17.795 | 0.5268 | 0.7372 | w |
| 6 | 5.100 | 6.513 | 16.817 | 0.4335 | 0.8173 | w |
| 7 | 5.107 | 6.521 | 16.051 | 0.3964 | 1.0180 | d |

particle 3

| point | DP(v) | Tamb(v) | DC(v) | rh | total mfs | dry/wet |
|---|---|---|---|---|---|---|
| **1** | **5.895** | **6.483** | **17.777** | **0.7712** | **0.4833** | w |
| 2 | 5.680 | 6.494 | 14.008 | 0.6609 | 0.6133 | w |
| 3 | 5.378 | 6.499 | 11.697 | 0.5333 | 0.7345 | w |
| 4 | 5.169 | 6.493 | 10.741 | 0.4610 | 0.7999 | w |
| 5 | 5.290 | 6.503 | 11.180 | 0.4998 | 0.7685 | w |
| 6 | 5.523 | 6.497 | 12.478 | 0.5914 | 0.6885 | w |
| 7 | 5.740 | 6.500 | 14.736 | 0.6865 | 0.5830 | w |
| 8 | 5.795 | 6.496 | 15.568 | 0.7146 | 0.5519 | w |
| 9 | 5.843 | 6.489 | 16.452 | 0.7416 | 0.5222 | w |
| 10 | 4.982 | 16.497 | 10.221 | 0.4015 | 0.8406 | w |
| 11 | 5.232 | 6.495 | 10.955 | 0.4817 | 0.7842 | w |
| 12 | 4.861 | 6.506 | 8.429 | 0.3654 | 1.0190 | d |

**Table A3.3 cont'd**

particle 4

| Point | DP(v) | Tamb(v) | DC(v) | rh | total mfs | dry/wet |
|---|---|---|---|---|---|---|
| 1 | 5.504 | 6.495 | 6.649 | 0.5843 | 0.6801 | w |
| 2 | 5.287 | 6.496 | 5.943 | 0.5008 | 0.7609 | w |
| 3 | 5.004 | 6.508 | 5.386 | 0.4054 | 0.8396 | w |
| 4 | 5.171 | 6.48 | 5.653 | 0.4653 | 0.8000 | w |
| 5 | 5.412 | 6.496 | 6.226 | 0.5473 | 0.7263 | w |
| 6 | 5.57 | 6.499 | 6.76 | 0.6104 | 0.6690 | w |
| **7** | **5.888** | **6.499** | **9.088** | **0.7602** | **0.4976** | **w** |
| 8 | 5.845 | 6.498 | 8.554 | 0.7387 | 0.5287 | w |
| 9 | 5.796 | 6.509 | 8.119 | 0.7096 | 0.5570 | w |
| 10 | 5.744 | 6.506 | 7.677 | 0.6859 | 0.5890 | w |

**Table A3.4:**
**Raw data of water activity measurements of $NH_4NO_3/(NH_4)_2SO_4$ solutions at n=2**

particle 1

| Point | DP(v) | Tamb(v) | DC(v) | rh | total mfs | dry/wet |
|---|---|---|---|---|---|---|
| **1** | **5.776** | **6.401** | **11.003** | **0.7466** | **0.5067** | **w** |
| 2 | 5.624 | 6.403 | 9.436 | 0.5961 | 0.6739 | w |
| 3 | 5.340 | 6.408 | 7.733 | 0.5481 | 0.7210 | w |
| 4 | 5.147 | 6.413 | 7.056 | 0.4759 | 0.7902 | w |
| 5 | 54.041 | 6.414 | 6.843 | 0.4402 | 0.8148 | w |
| 6 | 4.963 | 6.430 | 6.632 | 0.4122 | 0.8407 | w |
| 7 | 4.846 | 6.425 | 5.333 | 0.3793 | 1.0450 | d |
| 8 | 5.977 | 6.440 | 16.805 | 0.8366 | 0.3318 | w |
| 9 | 5.979 | 6.452 | 16.962 | 0.8317 | 0.3287 | w |
| 10 | 5.831 | 6.446 | 13.196 | 0.7547 | 0.4225 | w |

particle 2

| Point | DP(v) | Tamb(v) | DC(v) | rh | total mfs | dry/wet |
|---|---|---|---|---|---|---|
| 1 | 5.747 | 6.399 | 5.276 | 0.7369 | 0.5255 | w |
| **2** | **5.795** | **6.403** | **5.585** | **0.7555** | **0.4965** | **w** |
| 3 | 5.734 | 6.409 | 5.236 | 0.7218 | 0.5296 | w |
| 4 | 5.565 | 6.414 | 4.442 | 0.6400 | 0.6242 | w |
| 5 | 5.391 | 6.417 | 3.958 | 0.5653 | 0.7006 | w |
| 6 | 5.218 | 6.425 | 3.610 | 0.4973 | 0.7681 | w |
| 7 | 5.079 | 6.422 | 3.474 | 0.4507 | 0.7982 | w |
| 8 | 4.977 | 6.424 | 3.358 | 0.4180 | 0.8257 | w |
| 9 | 4.856 | 6.436 | 2.990 | 0.3796 | 0.9274 | d |

particle 3

| Point | DP(v) | Tamb(v) | DC(v) | rh | total mfs | dry/wet |
|---|---|---|---|---|---|---|
| 1 | 5.824 | 6.456 | 5.338 | 0.7466 | 0.4950 | w |
| 2 | 5.715 | 6.459 | 4.667 | 0.6914 | 0.5661 | w |
| 3 | 5.540 | 6.471 | 4.054 | 0.6078 | 0.6518 | w |
| 4 | 5.352 | 6.470 | 3.593 | 0.5327 | 0.7354 | w |
| 5 | 5.192 | 6.480 | 3.342 | 0.4723 | 0.7906 | w |
| 6 | 4.933 | 6.489 | 3.114 | 0.3892 | 0.8484 | w |
| 7 | 5.247 | 6.478 | 3.420 | 0.4919 | 0.7726 | w |
| 8 | 5.435 | 6.480 | 3.763 | 0.5616 | 0.7022 | w |
| 9 | 5.656 | 6.486 | 4.348 | 0.6531 | 0.6077 | w |
| 10 | 5.779 | 6.491 | 4.811 | 0.7089 | 0.5492 | w |
| **11** | **5.835** | **6.494** | **5.089** | **0.7354** | **0.5192** | **w** |
| 12 | 4.825 | 6.501 | 2.637 | 0.3569 | 1.0020 | d |

**Table A3.5:**
**Raw data of water activity measurements of $NH_4NO_3/(NH_4)_2SO_4$ solutions at n=1**

particle 1

| Point | DP(v) | Tamb(v) | DC(v) | rh | total mfs | dry/wet |
|---|---|---|---|---|---|---|
| **1** | **5.794** | **6.493** | **28.466** | **0.7154** | **0.5298** | **w** |
| 2 | 5.729 | 6.494 | 26.904 | 0.6837 | 0.5606 | w |
| 3 | 5.619 | 6.473 | 24.724 | 0.6417 | 0.6100 | w |
| 4 | 5.465 | 6.481 | 22.396 | 0.5732 | 0.6734 | w |
| 5 | 5.321 | 6.487 | 20.925 | 0.5158 | 0.7208 | w |
| 6 | 5.222 | 6.495 | 20.086 | 0.4783 | 0.7509 | w |
| 7 | 5.063 | 6.500 | 19.077 | 0.4252 | 0.7906 | w |
| 8 | 4.872 | 6.496 | 14.922 | 0.3706 | 1.0110 | d |
| 9 | 4.455 | 6.504 | 14.944 | 0.2699 | 1.0090 | d |

particle 2

| Point | DP(v) | Tamb(v) | DC(v) | rh | total mfs | dry/wet |
|---|---|---|---|---|---|---|
| 1 | 5.478 | 6.473 | 20.778 | 0.5813 | 0.6744 | w |
| 2 | 5.144 | 6.483 | 17.770 | 0.4554 | 0.7886 | w |
| 3 | 5.267 | 6.486 | 18.642 | 0.4966 | 0.7517 | w |
| 4 | 5.365 | 6.488 | 19.484 | 0.5319 | 0.7192 | w |
| 5 | 5.577 | 6.498 | 21.929 | 0.6138 | 0.6390 | w |
| 6 | 5.726 | 6.498 | 24.363 | 0.6807 | 0.5752 | w |
| 7 | 5.841 | 6.501 | 27.372 | 0.7353 | 0.5119 | w |
| **8** | **5.890** | **6.509** | **28.732** | **0.7567** | **0.4877** | **w** |
| 9 | 4.908 | 6.508 | 16.733 | 0.3778 | 0.8374 | w |
| 10 | 4.821 | 6.512 | 16.447 | 0.3535 | 0.8520 | w |
| 11 | 4.692 | 6.512 | 13.696 | 0.3212 | 1.0230 | d |

particle 3

| Point | DP(v) | Tamb(v) | DC(v) | rh | total mfs | dry/wet |
|---|---|---|---|---|---|---|
| 1 | 5.890 | 6.479 | 15.798 | 0.7704 | 0.4717 | w |
| 2 | 5.723 | 6.490 | 13.231 | 0.6825 | 0.5632 | w |
| 3 | 5.354 | 6.491 | 10.420 | 0.5268 | 0.7152 | w |
| 4 | 5.148 | 6.494 | 9.592 | 0.4538 | 0.7769 | w |
| 5 | 5.280 | 6.492 | 10.098 | 0.4995 | 0.7380 | w |
| 6 | 5.468 | 6.500 | 11.047 | 0.5680 | 0.6746 | w |
| 7 | 5.788 | 6.506 | 13.918 | 0.7070 | 0.5354 | w |
| **8** | **5.889** | **6.505** | **15.324** | **0.7580** | **0.4863** | **w** |
| 9 | 5.672 | 6.507 | 12.557 | 0.6522 | 0.5935 | w |
| 10 | 4.968 | 6.513 | 7.353 | 0.3937 | 1.0130 | d |
| 11 | 4.467 | 6.508 | 7.349 | 0.2717 | 1.0140 | d |

**Table A3.6:**
**Raw data of water activity measurements of $NH_4NO_3/(NH_4)_2SO_4$ solutions at n=1/2**

particle 1

| Point | DP(v) | Tamb(v) | DC(v) | rh | total mfs | dry/wet |
|---|---|---|---|---|---|---|
| 1 | 5.717 | 6.444 | 32.390 | 0.6986 | 0.5525 | w |
| 2 | 5.559 | 6.461 | 28.736 | 0.6197 | 0.6228 | w |
| 3 | 5.345 | 6.468 | 25.709 | 0.5307 | 0.6961 | w |
| 4 | 5.262 | 6.478 | 24.780 | 0.4972 | 0.7222 | w |
| 5 | 5.454 | 6.479 | 26.544 | 0.5695 | 0.6742 | w |
| 6 | 5.659 | 6.488 | 30.215 | 0.6537 | 0.5923 | w |
| 7 | 5.788 | 6.495 | 33.530 | 0.7116 | 0.5337 | w |
| **8** | **5.892** | **6.503** | **37.450** | **0.7605** | **0.4779** | **w** |
| 9 | 5.837 | 6.499 | 35.180 | 0.7342 | 0.5087 | w |
| 10 | 5.221 | 6.493 | 24.379 | 0.4785 | 0.7341 | w |
| 11 | 5.166 | 6.497 | 23.653 | 0.4589 | 0.7566 | w |
| 12 | 5.053 | 6.493 | 23.002 | 0.4239 | 0.7780 | w |
| 13 | 4.942 | 6.502 | 17.531 | 0.3888 | 1.0210 | d |
| 14 | 4.514 | 6.494 | 14.531 | 0.2839 | 1.0210 | d |

particle 2

| Point | DP(v) | Tamb(v) | DC(v) | rh | total mfs | dry/wet |
|---|---|---|---|---|---|---|
| 1 | 5.477 | 6.500 | 21.333 | 0.5716 | 0.6583 | w |
| 2 | 5.671 | 6.505 | 23.864 | 0.6525 | 0.5885 | w |
| 3 | 5.791 | 6.507 | 26.325 | 0.7080 | 0.5335 | w |
| **4** | **5.892** | **6.511** | **29.165** | **0.7569** | **0.4815** | **w** |
| 5 | 5.836 | 6.518 | 27.652 | 0.7254 | 0.5079 | w |
| 6 | 5.729 | 6.511 | 25.081 | 0.6768 | 0.5600 | w |
| 7 | 5.586 | 6.510 | 22.683 | 0.6133 | 0.6192 | w |
| 8 | 5.381 | 6.521 | 20.369 | 0.5275 | 0.6895 | w |
| 9 | 5.226 | 6.514 | 19.332 | 0.4743 | 0.7365 | w |
| 10 | 5.086 | 6.524 | 18.286 | 0.4262 | 0.7680 | w |
| 11 | 4.993 | 6.517 | 17.769 | 0.4000 | 0.7904 | w |
| 12 | 4.877 | 6.520 | 17.390 | 0.3667 | 0.8076 | w |
| 13 | 4.810 | 6.527 | 17.137 | 0.3475 | 0.8195 | w |
| 14 | 4.682 | 6.521 | 16.677 | 0.3171 | 0.8421 | w |
| 15 | 4.507 | 6.517 | 13.847 | 0.2786 | 1.0140 | d |

**Table A3.6 cont'd**

particle 3

| Point | DP(v) | Tamb(v) | DC(v) | rh | total mfs | dry/wet |
|---|---|---|---|---|---|---|
| 1 | 5.478 | 6.518 | 17.115 | 0.5659 | 0.6563 | w |
| 2 | 5.669 | 6.511 | 19.124 | 0.6493 | 0.5873 | w |
| 3 | 5.791 | 6.517 | 21.159 | 0.7083 | 0.5309 | w |
| **4** | **5.895** | **6.509** | **23.447** | **0.7593** | **0.4791** | w |
| 5 | 5.857 | 6.507 | 22.566 | 0.7408 | 0.4978 | w |
| 6 | 5.760 | 6.506 | 20.885 | 0.6935 | 0.5378 | w |
| 7 | 5.613 | 6.511 | 18.756 | 0.6245 | 0.5989 | w |

particle 4

| Point | DP(v) | Tamb(v) | DC(v) | rh | total mfs | dry/wet |
|---|---|---|---|---|---|---|
| **1** | **5.895** | **6.499** | **27.476** | **0.7639** | **0.4744** | w |
| 2 | 5.818 | 6.502 | 25.540 | 0.7234 | 0.5104 | w |
| 3 | 5.705 | 6.500 | 23.129 | 0.6701 | 0.5636 | w |
| 4 | 5.494 | 6.504 | 20.184 | 0.5771 | 0.6458 | w |
| 5 | 5.328 | 6.507 | 18.667 | 0.5123 | 0.6983 | w |
| 6 | 5.185 | 6.506 | 17.755 | 0.4627 | 0.7341 | w |
| 7 | 4.928 | 6.505 | 13.237 | 0.3841 | 0.9847 | d |

**Table A3.7:**
**Raw data of water activity measurements of $NH_4NO_3/(NH_4)_2SO_4$ solutions at n=1/3**

particle 1

| Point | DP(v) | Tamb(v) | DC(v) | rh | total mfs | dry/wet |
|---|---|---|---|---|---|---|
| **1** | **5.996** | **6.503** | **38.49** | **0.8161** | **0.4138** | w |
| 2 | 5.447 | 6.507 | 24.296 | 0.5573 | 0.6556 | w |
| 3 | 5.292 | 6.505 | 22.708 | 0.4999 | 0.7014 | w |
| 4 | 5.153 | 6.508 | 21.663 | 0.4516 | 0.7353 | w |
| 5 | 5.662 | 6.506 | 27.666 | 0.6481 | 0.5757 | w |
| 6 | 5.818 | 6.499 | 31.546 | 0.7247 | 0.5049 | w |
| 7 | 5.937 | 6.504 | 35.88 | 0.7837 | 0.4439 | w |
| 8 | 5.233 | 6.505 | 22.444 | 0.4792 | 0.7097 | w |
| 9 | 5.035 | 6.501 | 16.105 | 0.4164 | 0.9890 | d |
| 10 | 4.836 | 6.504 | 16.16 | 0.3592 | 0.9850 | d |

particle 2

| Point | DP(v) | Tamb(v) | DC(v) | rh | total mfs | dry/wet |
|---|---|---|---|---|---|---|
| 1 | 5.683 | 6.493 | 13.912 | 0.6627 | 0.5679 | w |
| 2 | 6.46 | 6.49 | 12.14 | 0.5682 | 0.6508 | w |
| **3** | **5.909** | **6.491** | **17.147** | **0.7749** | **0.4607** | w |
| 4 | 5.844 | 6.493 | 16.204 | 0.7404 | 0.4876 | w |
| 5 | 5.805 | 6.492 | 15.591 | 0.7213 | 0.5067 | w |
| 6 | 5.764 | 6.503 | 15.016 | 0.6967 | 0.5261 | w |
| 7 | 5.559 | 6.505 | 13.06 | 0.6036 | 0.6049 | w |
| 8 | 5.328 | 6.504 | 11.662 | 0.5132 | 0.6774 | w |
| 9 | 5.254 | 6.503 | 11.413 | 0.4871 | 0.6922 | w |
| 10 | 5.157 | 6.494 | 11.009 | 0.4567 | 0.7176 | w |
| 11 | 4.981 | 6.49 | 8.216 | 0.4029 | 0.9616 | d |

particle 3

| Point | DP(v) | Tamb(v) | DC(v) | rh | total mfs | dry/wet |
|---|---|---|---|---|---|---|
| 1 | 5.195 | 6.479 | 15.546 | 0.4736 | 0.7329 | w |
| 2 | 5.303 | 6.481 | 16.198 | 0.5111 | 0.7034 | w |
| 3 | 5.498 | 6.485 | 17.850 | 0.5853 | 0.6383 | w |
| 4 | 5.708 | 6.492 | 20.239 | 0.6747 | 0.5630 | w |
| 5 | 5.827 | 6.496 | 22.519 | 0.7305 | 0.5060 | w |
| **6** | **5.899** | **6.500** | **24.225** | **0.7655** | **0.4704** | w |
| 7 | 5.763 | 6.506 | 21.311 | 0.6949 | 0.5347 | w |
| 8 | 5.624 | 6.504 | 19.093 | 0.6320 | 0.5968 | w |
| 9 | 5.400 | 6.507 | 16.966 | 0.5391 | 0.6716 | w |
| 10 | 5.257 | 6.513 | 16.161 | 0.4852 | 0.7050 | w |
| 11 | 5.113 | 6.501 | 15.357 | 0.4406 | 0.7420 | w |
| 12 | 5.013 | 6.507 | 11.706 | 0.4083 | 0.9734 | d |

**Table A3.8:**
**Raw data of water activity measurements of $NH_4NO_3/(NH_4)_2SO_4$ solutions at n=1/5**

particle 1

| Point | DP(v) | Tamb(v) | DC(v) | rh | total mfs | dry/wet |
|---|---|---|---|---|---|---|
| 1 | 5.896 | 6.498 | 9.540 | 0.7648 | 0.4777 | w |
| **2** | **5.840** | **6.500** | **9.180** | **0.7353** | **0.4965** | w |
| 3 | 5.796 | 6.499 | 8.896 | 0.7138 | 0.5123 | w |
| 4 | 5.737 | 6.496 | 8.471 | 0.6867 | 0.5380 | w |
| 5 | 5.673 | 6.495 | 8.092 | 0.6573 | 0.5632 | w |
| 6 | 5.603 | 6.504 | 7.749 | 0.6228 | 0.5882 | w |
| 7 | 5.490 | 6.493 | 7.290 | 0.5792 | 0.6252 | w |
| 8 | 5.369 | 6.498 | 6.947 | 0.5302 | 0.6561 | w |
| 9 | 5.276 | 6.491 | 6.737 | 0.4983 | 0.6765 | w |
| 10 | 5.162 | 6.501 | 4.729 | 0.4568 | 0.9638 | d |

particle 2

| Point | DP(v) | Tamb(v) | DC(v) | rh | total mfs | dry/wet |
|---|---|---|---|---|---|---|
| **1** | **5.895** | **6.491** | **26.376** | **0.7675** | **0.4662** | w |
| 2 | 5.827 | 6.496 | 24.569 | 0.7305 | 0.5005 | w |
| 3 | 5.706 | 6.495 | 22.207 | 0.6725 | 0.5537 | w |
| 4 | 5.591 | 6.498 | 20.579 | 0.6198 | 0.5975 | w |
| 5 | 5.497 | 6.492 | 19.538 | 0.5824 | 0.6294 | w |
| 6 | 5.389 | 6.490 | 18.620 | 0.5404 | 0.6604 | w |
| 7 | 5.285 | 6.488 | 17.893 | 0.5025 | 0.6872 | w |
| 8 | 5.231 | 6.478 | 17.530 | 0.4863 | 0.7015 | w |
| 9 | 5.148 | 6.481 | 17.191 | 0.4573 | 0.7153 | w |
| 10 | 5.034 | 6.475 | 16.612 | 0.4226 | 0.7402 | w |
| 11 | 4.911 | 6.478 | 16.174 | 0.3855 | 0.7603 | w |
| 12 | 4.753 | 6.483 | 12.707 | 0.3420 | 0.9677 | d |

particle 3

| Point | DP(v) | Tamb(v) | DC(v) | rh | total mfs | dry/wet |
|---|---|---|---|---|---|---|
| 1 | 5.483 | 6.506 | 20.139 | 0.5720 | 0.6343 | w |
| 2 | 5.712 | 6.500 | 23.001 | 0.6733 | 0.5554 | w |
| 3 | 5.839 | 6.502 | 25.622 | 0.7339 | 0.4986 | w |
| **4** | **5.892** | **6.497** | **27.157** | **0.7632** | **0.4704** | w |
| 5 | 5.773 | 6.500 | 24.386 | 0.7022 | 0.5239 | w |
| 6 | 5.615 | 6.502 | 21.704 | 0.6288 | 0.5886 | w |
| 7 | 5.357 | 6.502 | 19.089 | 0.5245 | 0.6692 | w |
| 8 | 5.216 | 6.505 | 18.019 | 0.4734 | 0.7089 | w |
| 9 | 5.024 | 6.504 | 13.209 | 0.4123 | 0.9671 | d |

## Appendix 4

## Evaporation of precursor solutions of Magnesium and Zirconium oxides

By following the change in the *DC* potential to balance the weight of a levitated particle, the electrodynamic balance can be used to study the evaporation of droplets. We have investigated the drying process of ceramic precursor solutions used in spray pyrolysis. Spray pyrolysis is a powder synthesis process in which precursor solution droplets evaporate to form solid particles, which in turn undergo thermal decomposition to yield the desired particles such as refractory oxides and superconductive powders (Gardner and Messing 1984). The conditions of evaporation of precursor solution droplets can affect the density, the morphology, the size distribution, and chemical homogeneity of the final ceramic particles formed. To understand the role of precursor chemistry and evaporation rate on the morphology and density of the solid particles (for example, understanding the factors that lead to formation of hollow spheres rather than the desired dense spheres), the evaporation of a single ceramic precursor droplet was studied. By using an electro-optical servo system to change the electric potential to balance the weight of the particle, the mass of the particle undergoing evaporation was continuously monitored throughout the evaporation process (Sageev *et al.* 1986).

In particular, we have studied the evaporation of zirconium hydroxychloride and acetate and magnesium chloride, sulfate, and acetate solution droplets. The droplet was initially levitated in an environment of relative humidity at 80% using the conventional bihyperboloidal electrodynamic balance. Dry nitrogen gas then flowed through the chamber. In conjunction with the

measurement of the *DC* balancing voltage, 90° light scattering intensity was also recorded.

Figure A4.1 shows the history of evaporation of a magnesium chloride droplet. The *DC* voltage decreased smoothly until the droplet crystallized at about 6.5 hours when the particle lost its weight almost instantaneously to become a solid particle. Well defined resonance structures in light scattering were observed before crystallization took place. The light scattering intensity fluctuated after crystallization, since the dried particle scattered light quite randomly, depending on its surface morphology. Figure A4.2 plots the same data in a logarithmic scale. The slope of the balancing voltage was quite constant, as one would expect from evaporation of simple inorganic solutions such as NaCl, etc. Figures A4.3 and A4.4 depict the drying history of magnesium sulfate and magnesium acetate droplets. No crystallization was observed. Instead, there was a transition at about 1 hour after which the $MgSO_4$ droplet lost weight at a much slower rate. Similar phenomenon was observed for $Mg(CH_3COO)_2$ droplet at about 2 hours. This abrupt decrease in the evaporation rate can be attributed to the onset of gel formation. No light scattering data for these experiments were measured.

Figures A4.5 and A4.6 show the drying history of zirconium hydroxychloride and zirconium acetate solutions, respectively. Again, similar transitions of abrupt decrease in evaporation rate without crystallization were observed. Near the transition point of reduction in the evaporation rate, the light scattering signal became noisy but still resembled the resonance structures. This can be explained by the formation of gel structure which slightly augmented the

optical homogeneity of the droplet. Unlike $MgCl_2$, the dried particle resulting from gel formation maintained a roughly spherical shape although its surface showed some irregularity. This explanation can also be extended to the evaporation studies of magnesium sulfate and acetate solutions although light scattering signal was not measured in those experiments.

In addition to the above observation of gel formation and crystallization, some of these solutions apparently showed another transition in evaporation rate before gel formation. For examples, the magnesium sulfate and zirconium acetate droplets exhibited an increase in evaporation rate at about 0.8 hour and 0.15 hour respectively as shown in Figures A4.3 and A4.6. On the other hand, magnesium acetate droplets exhibited a decrease in evaporation rate before gel formation occurred as shown in Figure A4.4.

The formation of gel inside the droplet hindered the evaporation of water vapor from the droplet. In spray pyrolysis, droplets pass through a furnace at a few hundred degrees. If the gel is porous to water vapor, water can ultimately leave the droplet. If not, further heating of the droplet would cause internal explosion of the droplet. As a result, the morphology, the size distribution, and chemical composition of the powder product cannot be controlled. Further investigations on the dependence of gel formation and the final particle chemical composition on the drying condition are suggested.

**References**

Gardner T. J. and Messing G. L. "Preparation of MgO powder by evaporative decomposition of solutions," Ceramic Bulletin, 63(12), 1498-1504, 1984.

Sageev G., Flagan R. C., Seinfeld J. H. and Arnold S. "Condensation rate of water on aqueous droplets in the transition regime," J. Coll. Interf. Sci. 113(2), 421-429, 1986.

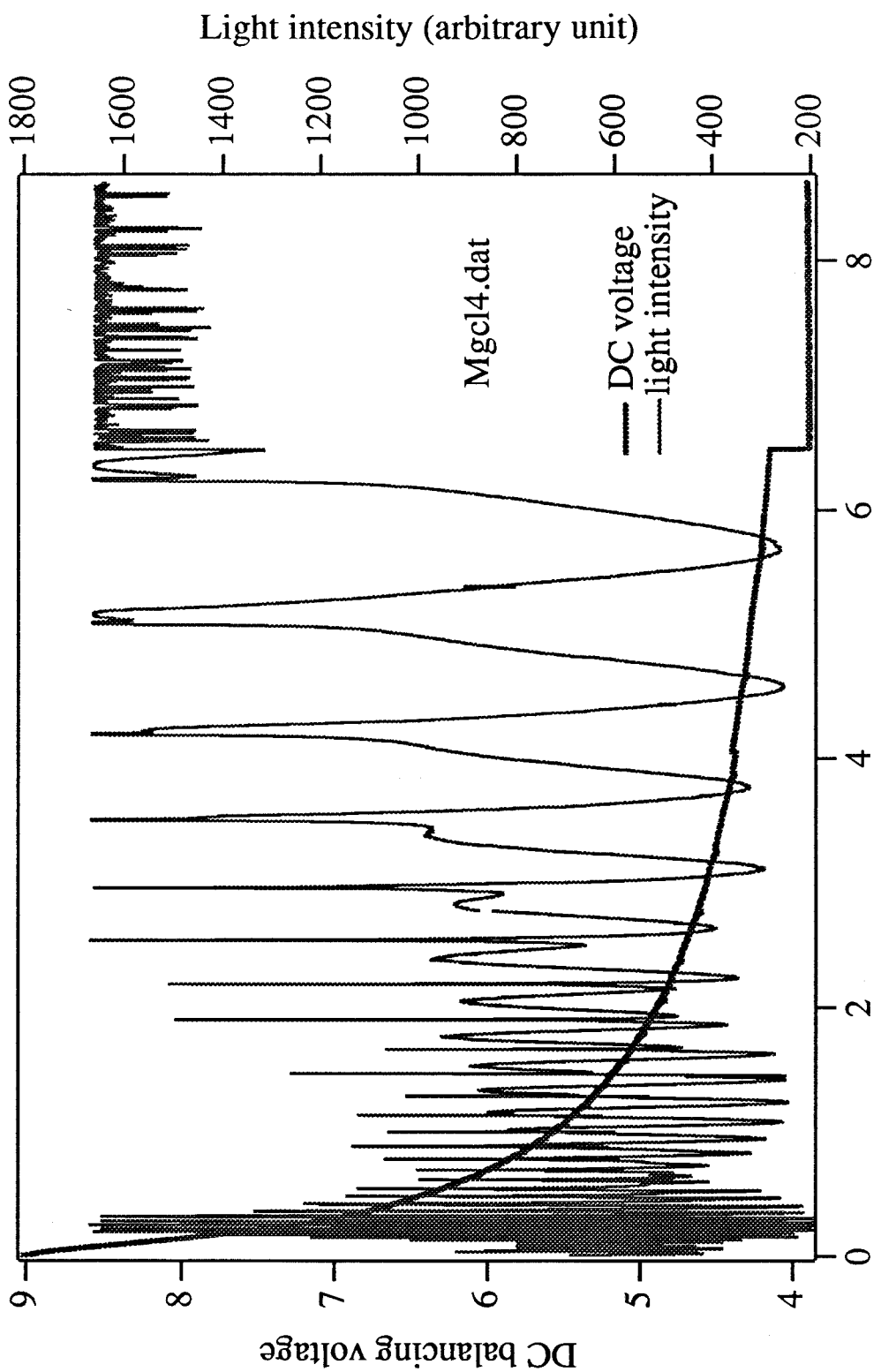


Figure A4.1: Evaporation of a magnesium chloride droplet

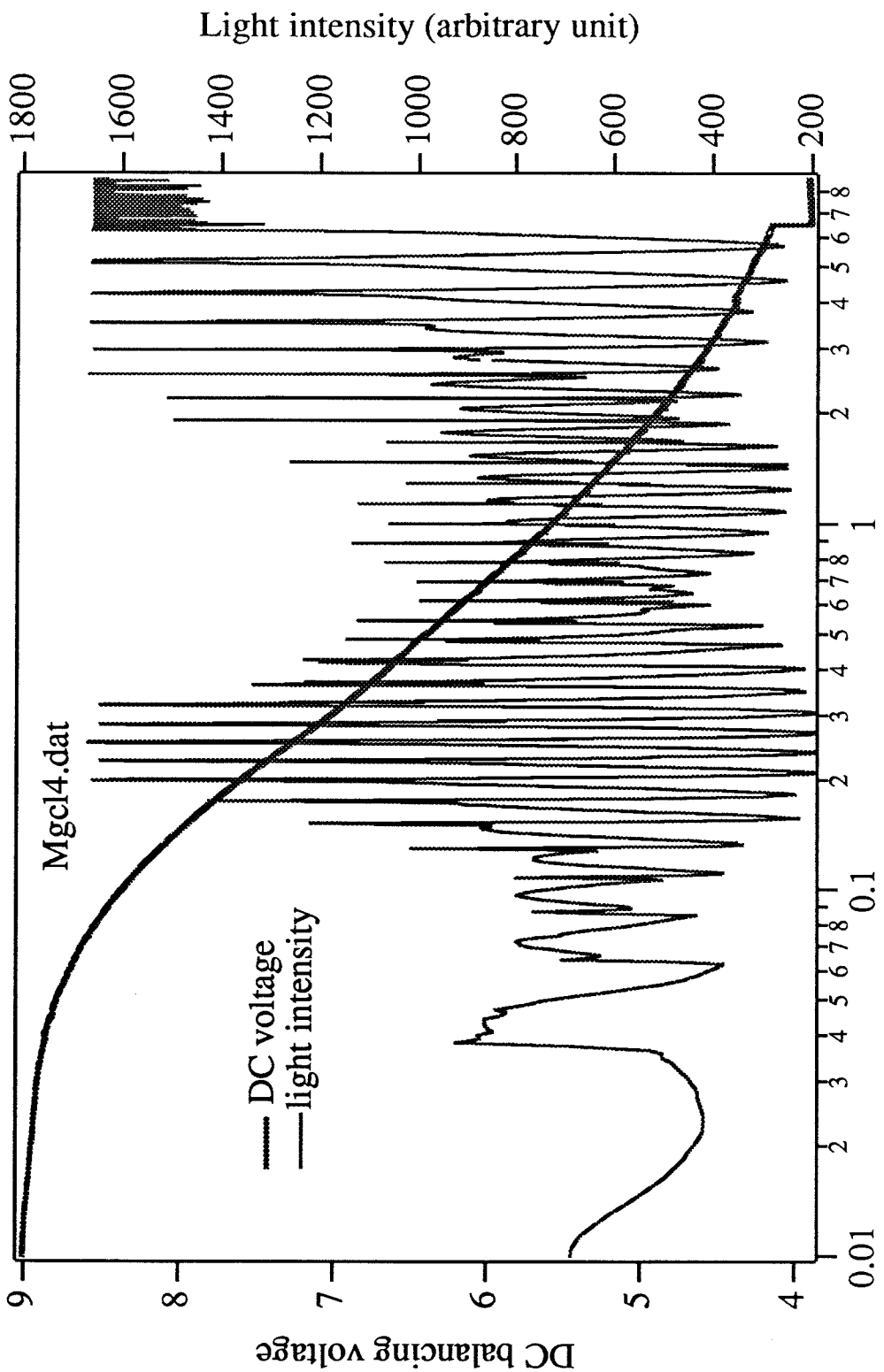


Figure A4.2: Evaporation of a magnesium chloride droplet in log scale

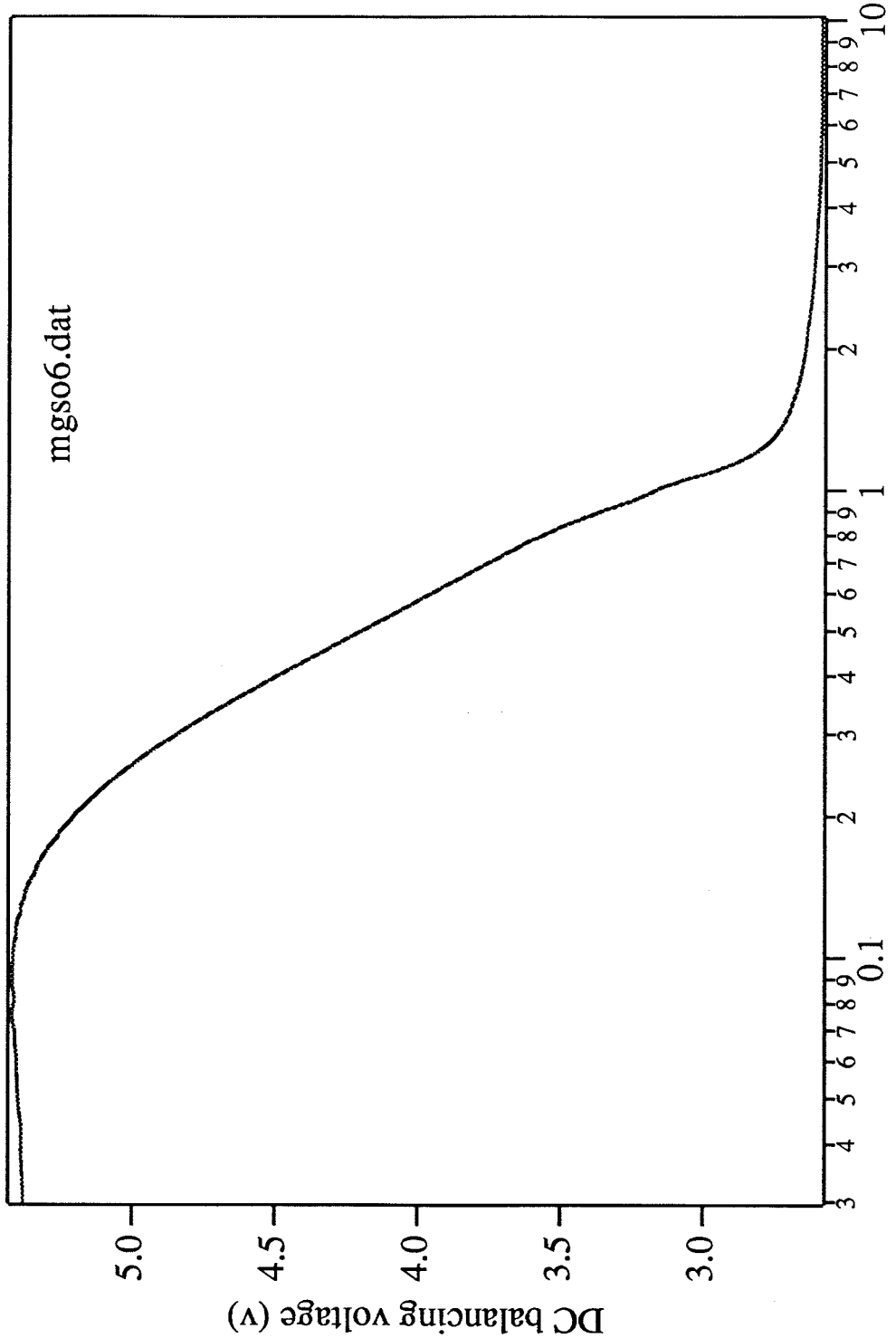


Figure A4.3: Evaporation of a magnesium sulfate droplet

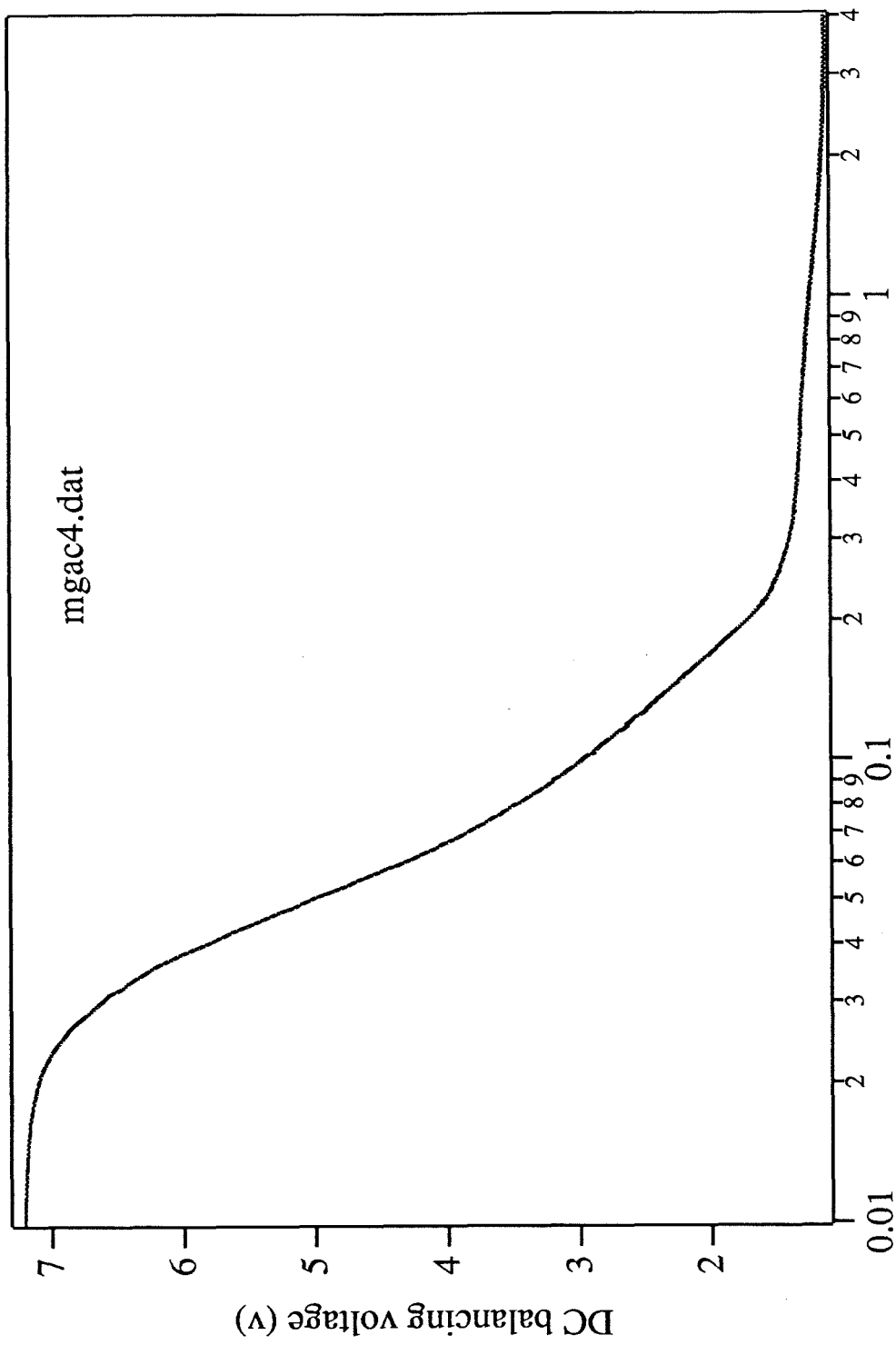


Figure A4.4: Evaporation of a magnesium acetate droplet

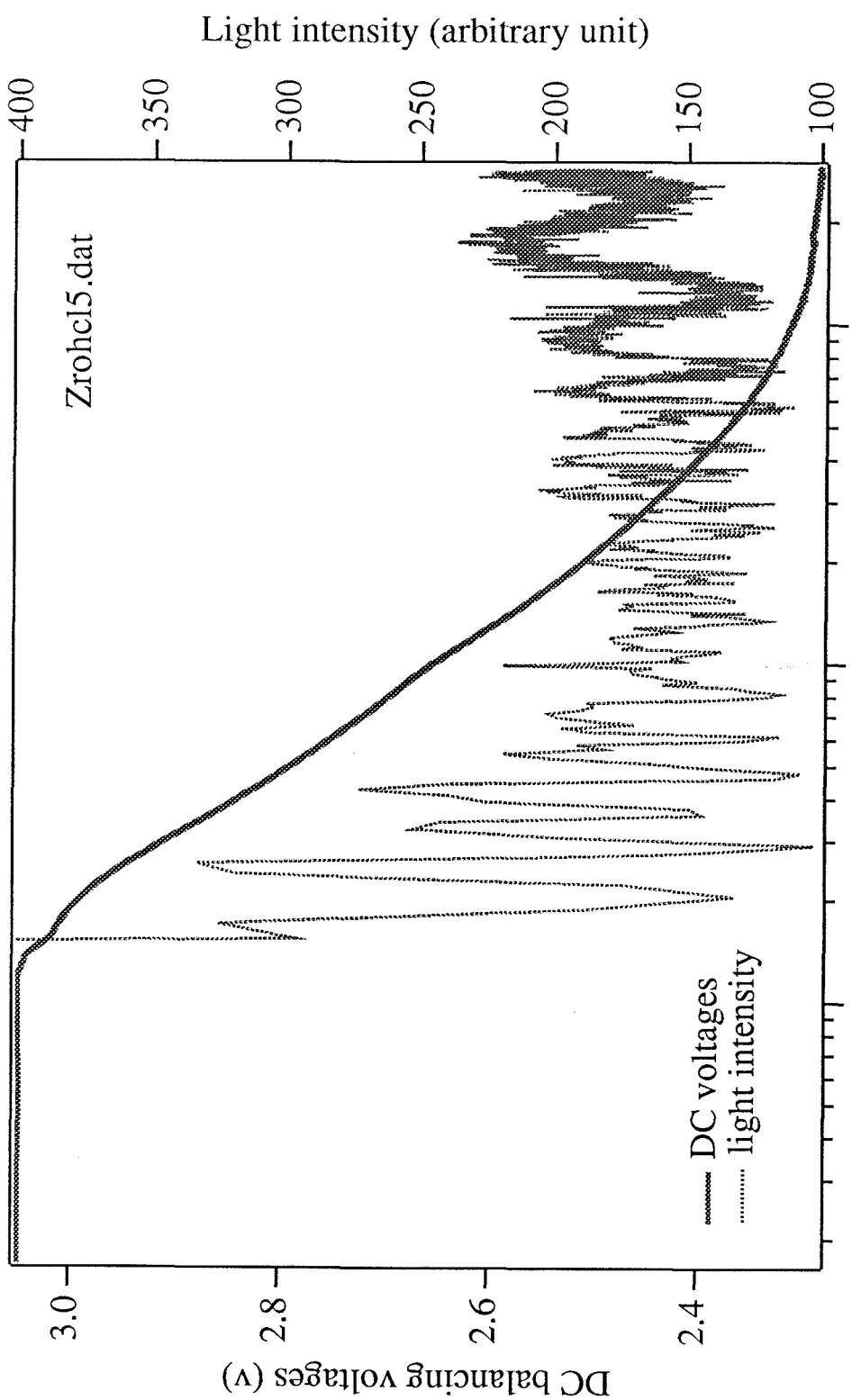


Figure A4.5: Evaporation of a zirconium hydroxychloride droplet

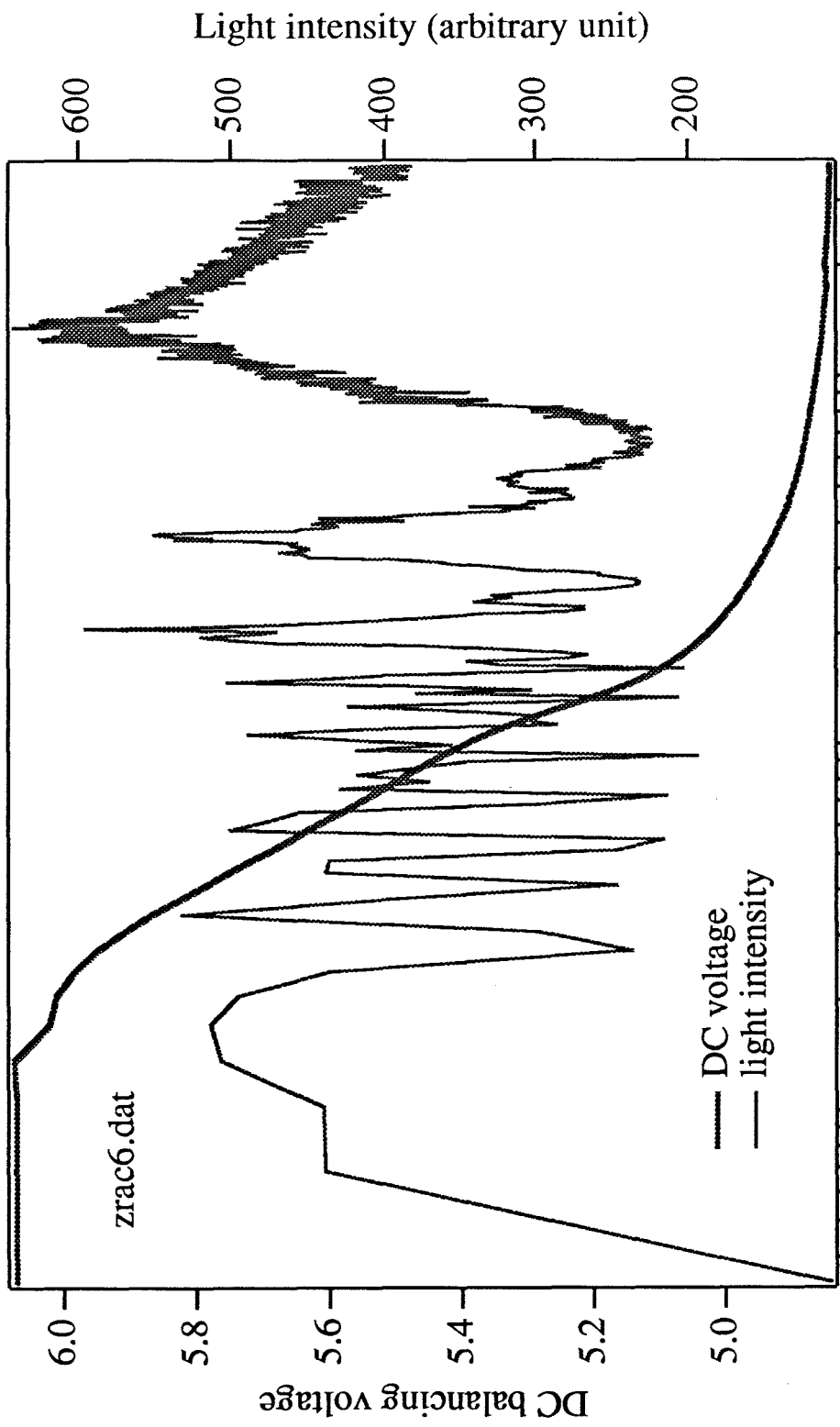


Figure A4.6: Evaporation of a zirconium acetate droplet

## Appendix 5

## Rapid evaporation of aqueous inorganic droplets

As described in Appendix 4, ceramic precursor solution droplets were levitated and dried by flowing nitrogen through the vacuum chamber containing the conventional electrodynamic balance. The residence time of the chamber was in the order of minutes and therefore did not play a significant role in the study of the evaporation kinetics of these droplets which happened in a time scale of an hour. However, for more simple droplets such as NaCl solutions, the time scale of evaporation is in the order of seconds. Evaporation kinetics of these droplets cannot be studied by changing the relative humidity of the chamber using a flowing system.

An approach to investigate the rapid drying behaviors of droplets is demonstrated in the following study of evaporations of NaCl and $(NH_4)_2SO_4$ droplets. A constant relative humidity was maintained in the chamber by flowing through humidified nitrogen for about an hour. During this period, the droplet generator was in place right above the electrodynamic balance. A teflon sleeve was made to enclose the injector as well as to seal the top opening of the chamber such that gas only came out through the small gap between the teflon piece and the droplet injector as illustrated in Figure A5.1. The servo system intended to balance any trapped particle was on before injection of particles. About 0.2 s after trapping a droplet, the servo would lock onto the particle by changing the *DC* required to balance the particle. Thus, evaporation in the time of several seconds can then be followed.

In the continuum regime, the mass ($m$) loss of an aqueous droplet due to evaporation of water alone is governed by

$$\frac{dm}{dt} = -\frac{4\pi M_w D}{RT}\left(\frac{3m}{4\pi\rho}\right)^{\frac{1}{3}}(p - p_\infty) , \qquad \text{(A5.1)}$$

where $M_w$ is the molecular weight of water, $R$ is the gas constant, $T$ is the ambient temperature, $\rho$ is the density of the droplet. $p$ and $p_\infty$ are the partial water vapor pressure above the droplet surface and that of the background, respectively. For pure water droplet where $\rho$ and $p$ are invariant assuming no evaporation cooling, the droplet surface area decreases linearly in time. For solutions droplets, $\rho$ and $p$ are functions of the droplet composition which changes as water evaporates. Equation (A5.1) can be integrated to give $m(t)$ when the compositional dependence of $\rho$ and $p$ are incorporated.

Equation (A5.1) assumes no evaporation cooling; the droplet temperature is the same as the ambient temperature. In the case of rapid evaporation of droplet, the droplet temperature may not equilibrate to the ambient temperature. Assuming quasi-steady state, the droplet temperature, $T$, can be determined by

$$\Delta H_{vap}\frac{dm}{dt} = k(4\pi a)(T_\infty - T) , \qquad \text{(A5.2)}$$

where $\Delta H_{vap}$ is the heat of vaporization of water, $k$ is the thermal conductivity of air, $a$ is the particle radius, $T_\infty$ and $T$ are the ambient temperature and the droplet temperature, respectively. Taking consideration of $T$ and $T_\infty$ being different, Equation (A5.1) becomes

$$\frac{dm}{dt} = -\frac{4\pi M_w D}{R}\left(\frac{3m}{4\pi\rho}\right)^{\frac{1}{3}}\left(\frac{p}{T} - \frac{p_\infty}{T_\infty}\right). \qquad \text{(A5.3)}$$

The partial water vapor pressure above the droplet surface, $p$, is also a function of temperature which can be described by the Clausius-Clapeyron equation

$$p_T = p_{T_\infty} \bullet exp\left[-\frac{\Delta H_{vap}}{R}\left(\frac{1}{T} - \frac{1}{T_\infty}\right)\right], \qquad \text{(A5.4)}$$

where $p_{T_\infty}$ is the partial water vapor pressure of the droplet at $T_\infty$. Combining Equations (A5.2) to (A5.4) and the compositional dependence of $\rho$ and $p$, the mass loss history of a solution droplet can be calculated.

Figure A5.2 shows the evaporation of four water droplets. When there was no particle at the center of the balance, the $DC$ voltage floated at about 9 $v$. Upon trapping a water droplet, the servo began to track the mass of the droplet until the droplet became too small to give enough light scattering signal to the servo optics. Simple diffusion theory in the continuum regime leads to a linear relationship between droplet surface area and time. Since the $DC$ balancing voltage is proportional to the mass of each droplet, $DC^{2/3}$ should be linear in time. This is illustrated in Figure A5.3 which depicts $DC$ and $DC^{2/3}$ as a function of time for the third droplet shown in Figure A5.2.

In order to compare experimental data with theory, the exact moment when a particle was injected into the chamber needs to be determined. The droplet generator uses a piezoelectric strip to squirt out tiny droplets from a glass tip upon excitation by a short electric pulse. The pulse generator has a LED which

blinks when an electric pulse is generated. The voltage pulse to the LED can then be used to estimate when a droplet is released from the droplet generator. Figure A5.4 demonstrates the use of the trace voltage of the LED as a timer for the injection of a droplet. Several pulses were fired until a particle was trapped at about 45 s. Subsequently, the servo tracked a droplet and controlled the $DC$ as the droplet evaporated.

Figure A5.5 shows the measured servo voltage as a function of time as a NaCl droplet evaporated. Time at zero was set by the pulse of the trace voltage preceded the tracking of the droplet by the servo as illustrated in Figure A5.4. Typically, the servo locked a particle 0.2 to 0.3 s after the pulse. Calculations using Equations (A5.1) to (A5.4) with and without temperature compensation are also shown for comparisons. Mass to balancing voltage conversion was made by knowing the balancing voltage and mass of the dried particle resulted from crystallization of the droplet after the rapid evaporation experiment. The predicted evaporation process occurred in the same time scale of the experimental data although no exact match was observed. If there was a time delay between the LED pulse and the injection of the droplet, the experimental data would be closer to the theoretical predictions. Evaporation of the droplet decreases the droplet temperature and therefore lowers the evaporation rate. Calculations with consideration of temperature compensation apparently predict the measured evaporation rate better. Similar study with an ammonium sulfate droplet is presented in Figure A5.6. A program to calculate $M(t)$ of $(NH_4)_2SO_4$ droplets are also attached at the end of this appendix.

This study demonstrates the approach of dropping a droplet into a constant

relative humidity environment to study rapid evaporation of droplets using the electrodynamic balance. The method needs to be refined in reducing the uncertainty of the timing of droplet release and the time required for the servo to track a droplet after a droplet is injected. However, for evaporation process in the time scale of 10 s, the approach is applicable since it takes less than 0.5 s for the servo to track a particle.

The crystallization of ammonium sulfate droplets is rather interesting that warrants a short discussion. Figure A5.7 shows the evaporation of an $(NH_4)_2SO_4$ droplet by flowing nitrogen through the chamber. Unlike NaCl droplets which crystallize almost instantaneously to the final dried particle, $(NH_4)_2SO_4$ droplets continue to evaporate water right after crystallization occur. The drying conditions may affect the amount of water left in the particle after the onset of crystallization and the morphology of the final dried powder. Such a study may lead to some more understanding in the control of morphology of dried powder made from evaporation of droplets.

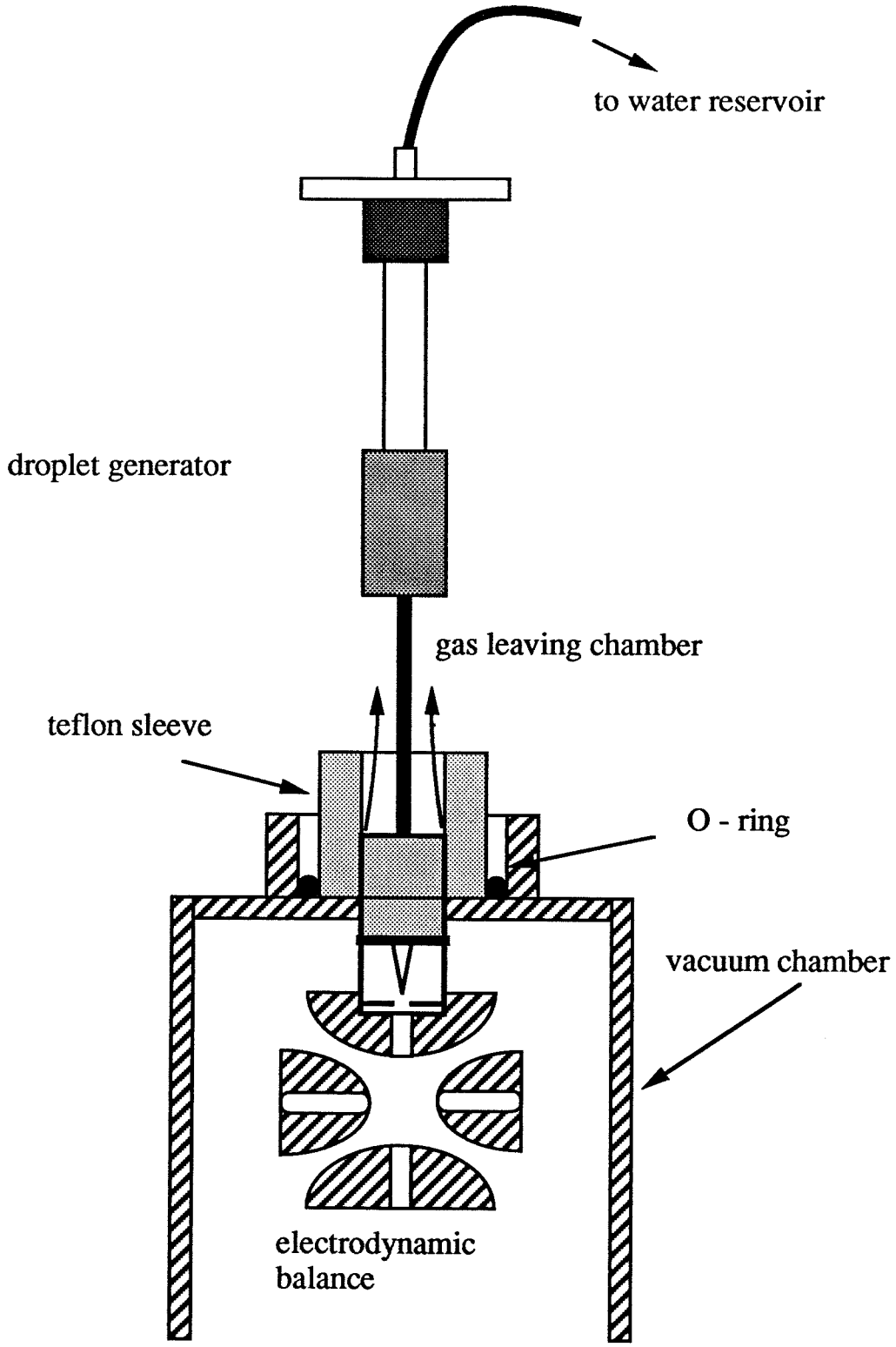


Figure A5.1: Configuration of the electrodynamic balance to study rapid evaporation of droplets

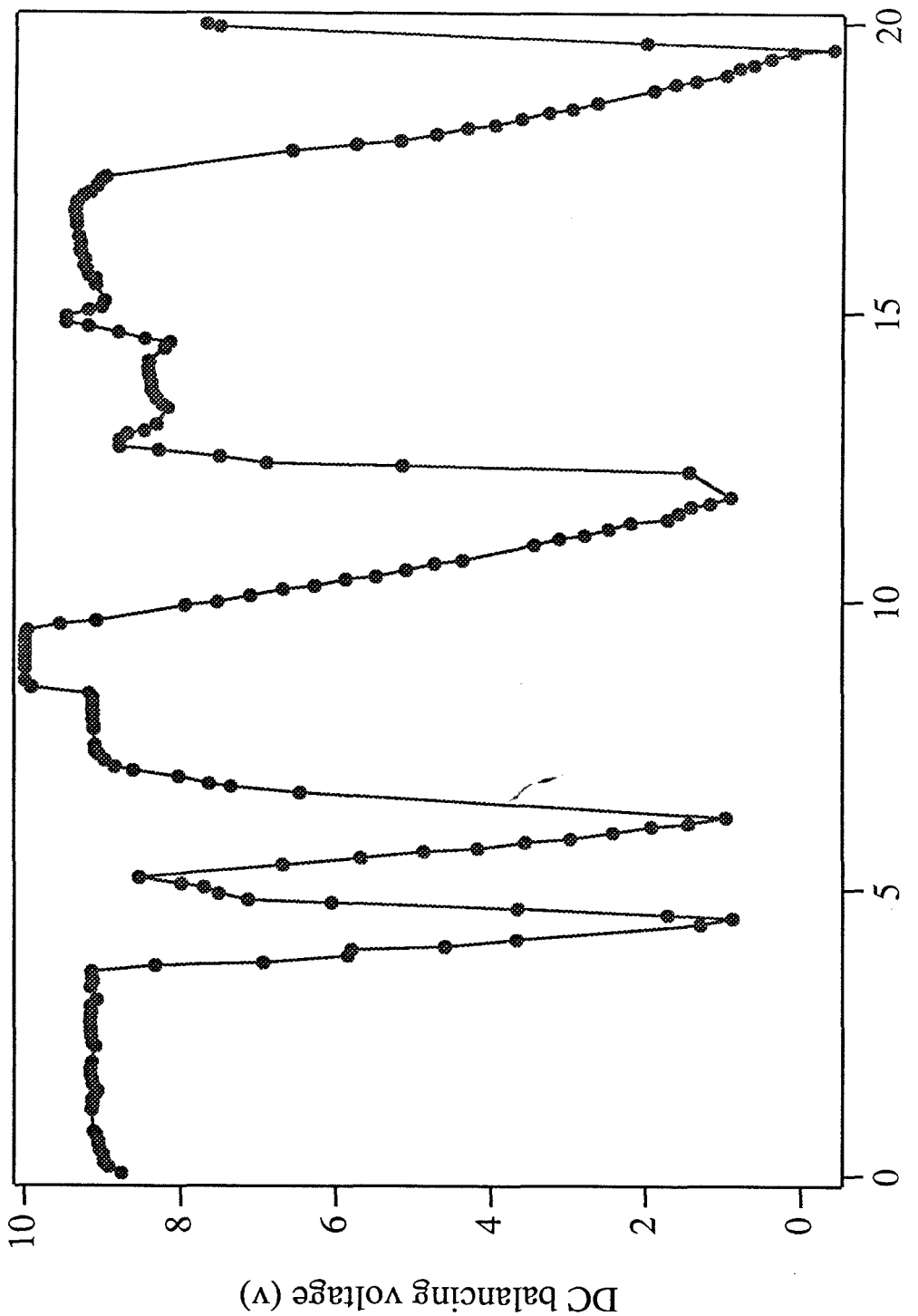


Figure A5.2: Evaporation of water droplets

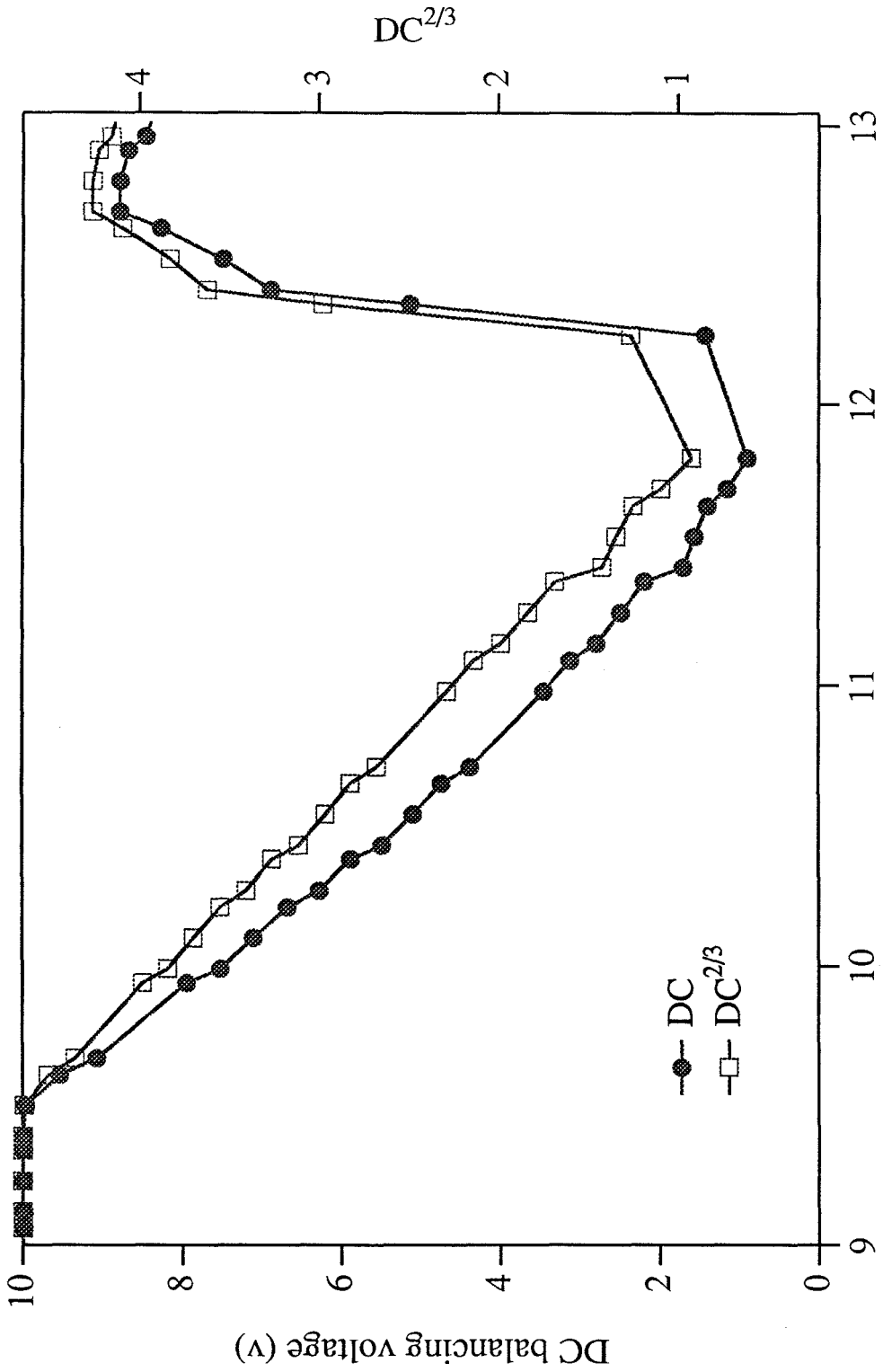


Figure A5.3: Surface area dependence of evaporation rate of water droplet

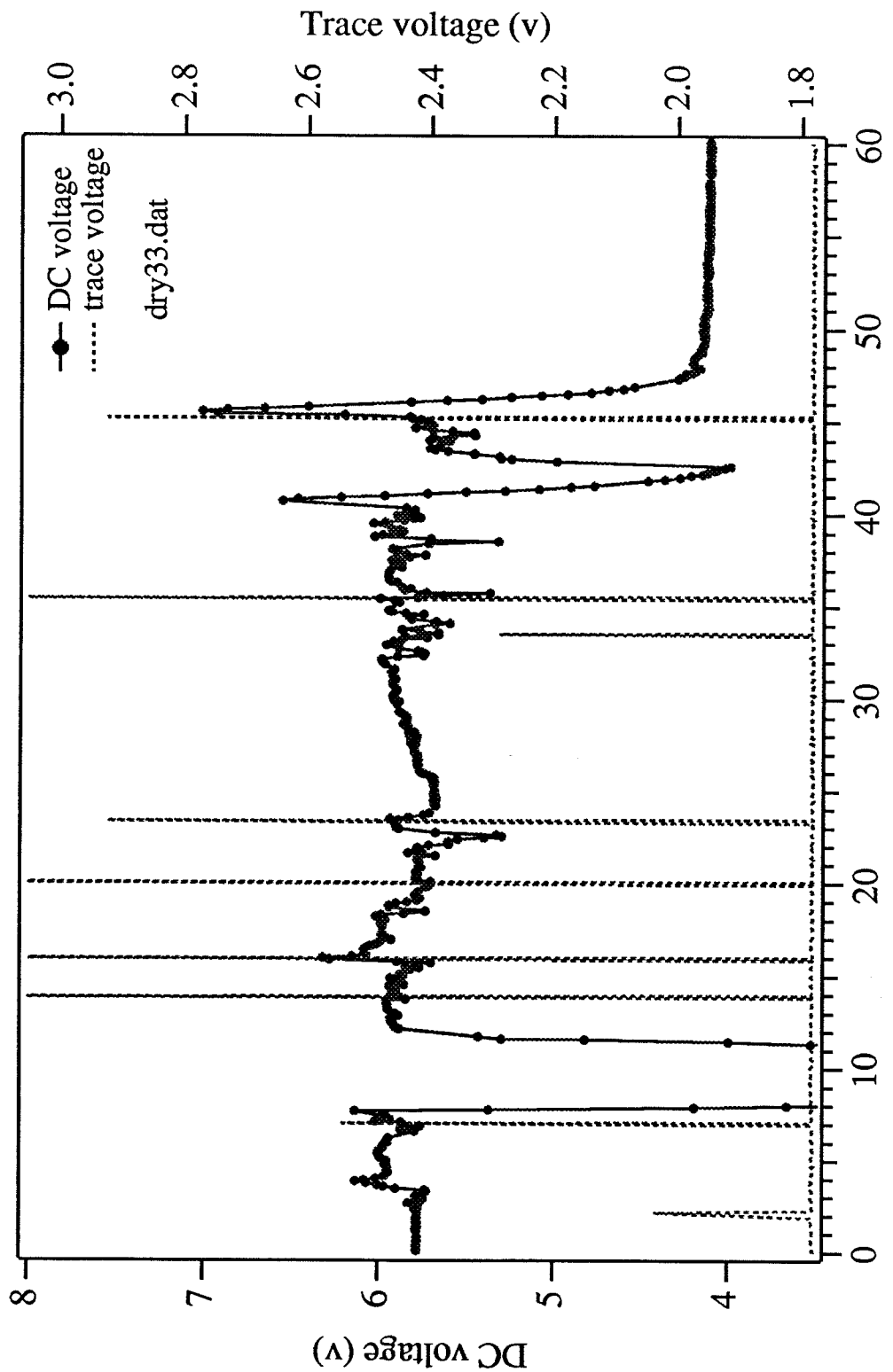


Figure A5.4: Timing of the injection of droplet

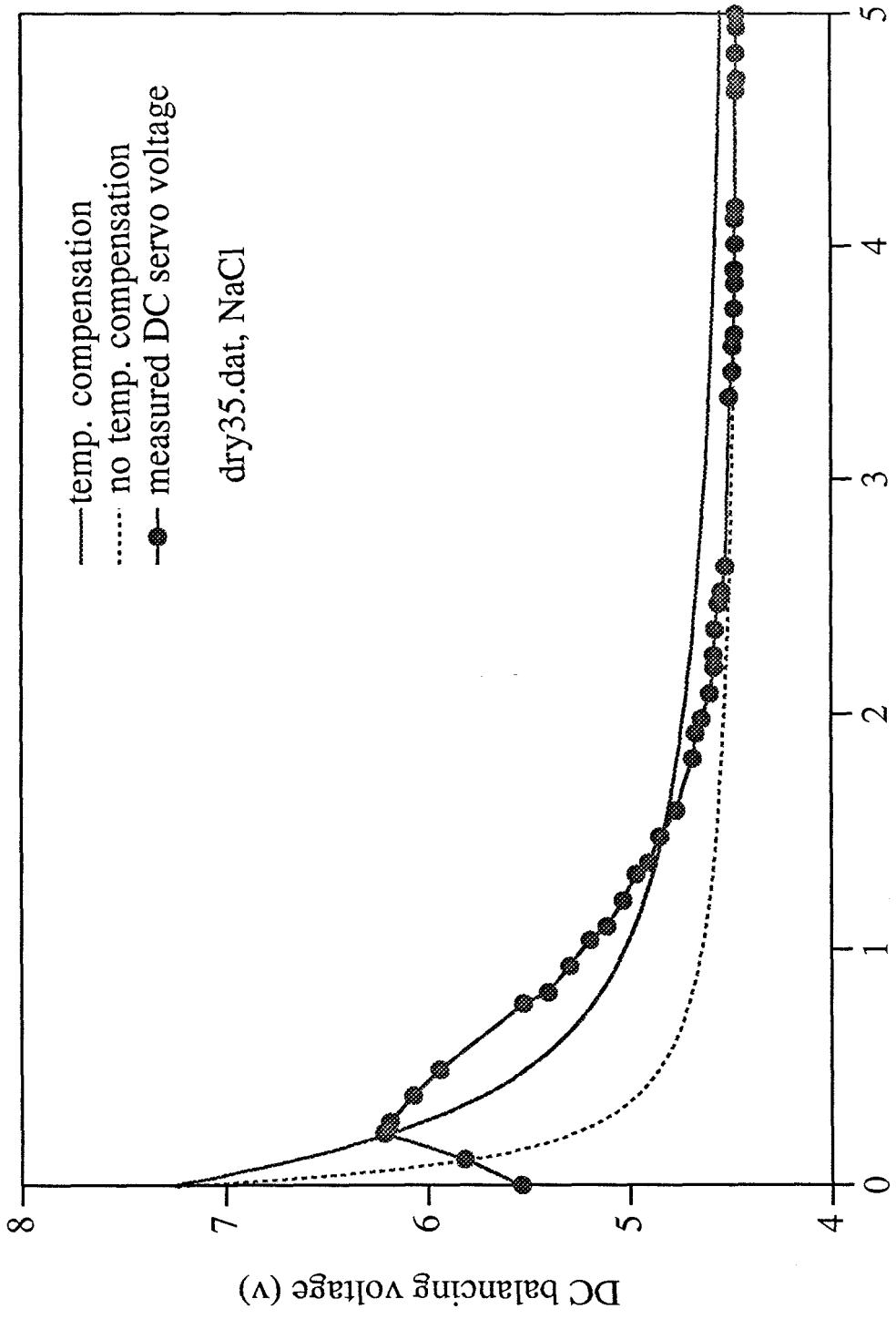


Figure A5.5: Evaporation of a sodium chloride droplet

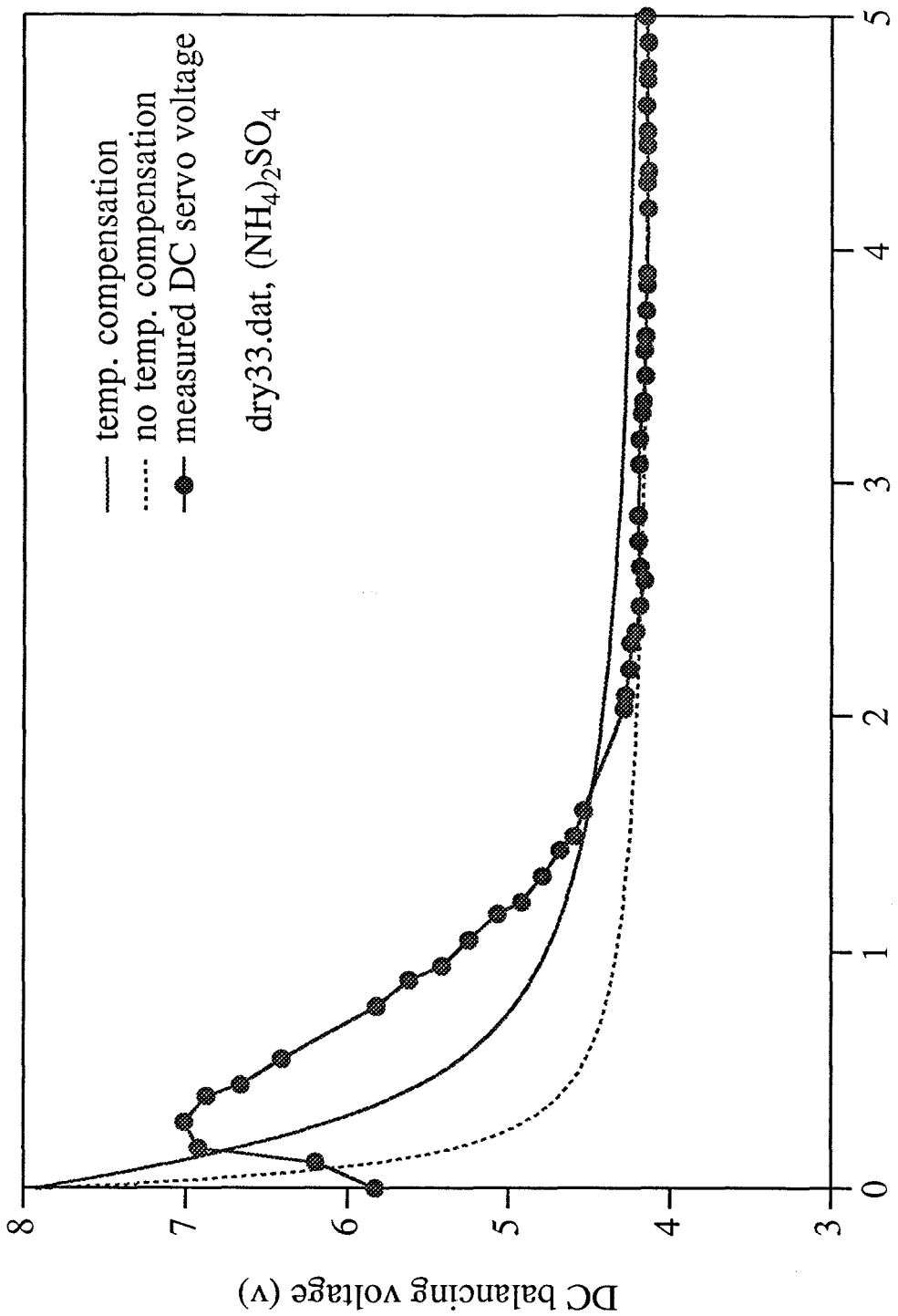


Figure A5.6: Evaporation of an ammonium sulfate droplet

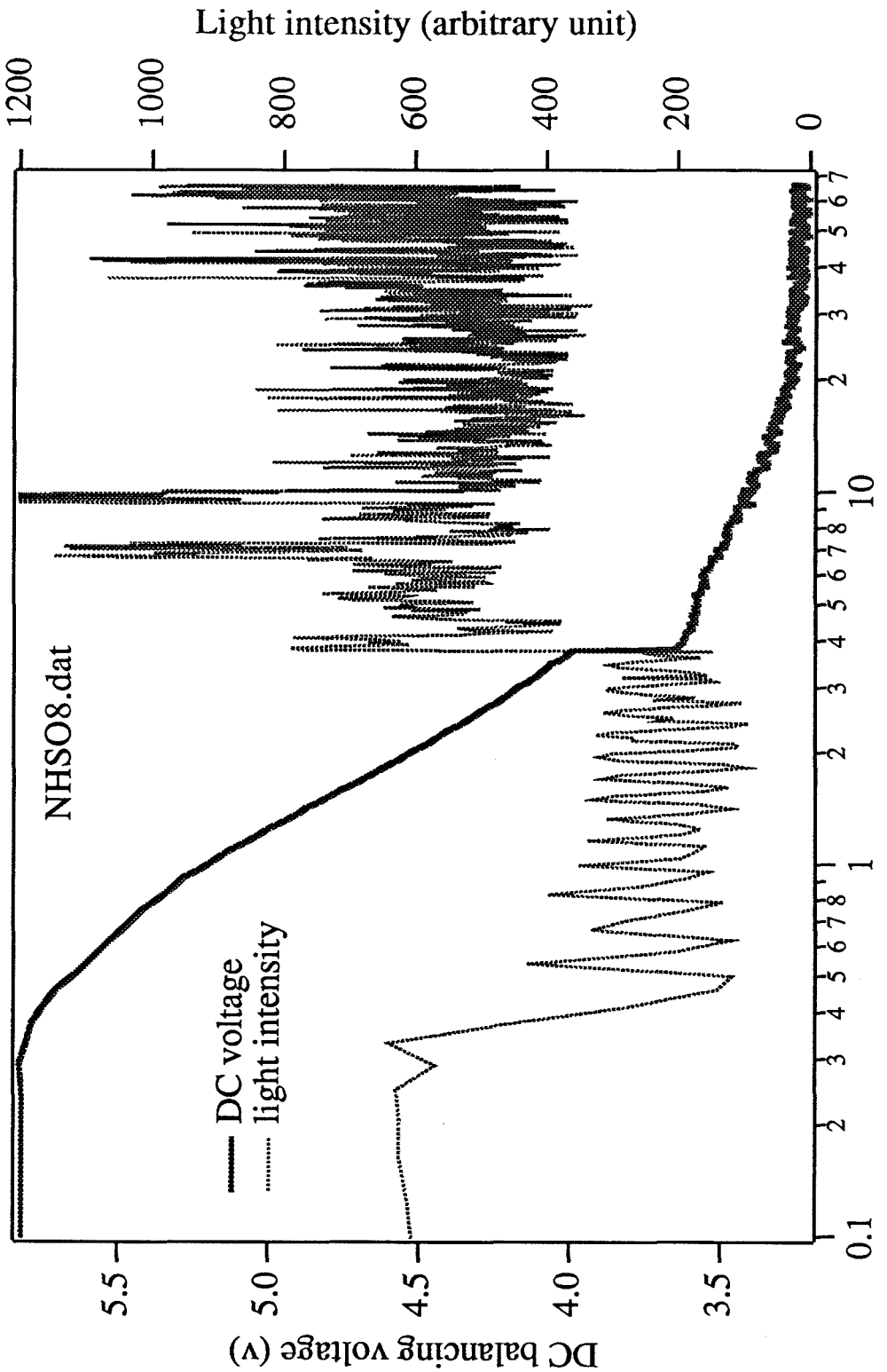


Figure A5.7: Crystallization of an ammonium sulfate droplet

```
      program nhso
      real ms, m, mo
      common tinf, pinf,rh,ms,den,d,rtsec
      external func,tseq
      open(unit=2, file='nhso.out', status='old')
c
c     this is a program to simulate the evaporation water from an
c     ammonium sulfate solution droplet through diffusion in gas
c     phase when a droplet is instantaneously exposed to a lower
c     relative humidity environment. Input parameters are the
c     ambient temperature and dew point, initial droplet mass and
c     dry particle mass. Simple diffusion theory, with and without
c     consideration of droplet cooling due to evaporation, is
c     considered.

      write(*,*) 'enter ambient temp and ambient dew point inC'
      read(*,*) tinf, dp
      tinf=tinf+273.15
      dp=dp+273.15
      pinf=exp(-5313.88/dp+20.988)
      write(*,*) 'enter original and dry particle mass in g'
      read(*,*) mo,ms
      write(*,*) 'enter dry particle voltage in mv'
      read(*,*) vs
c     d=diffusion coefficient of water vapor in air at 298K, taken
c     as 0.25 cm2/s
      d=0.25
      do 200, j=1,500
      m=mo*(500-j)/500
      wfs=ms/m
c
c      calulate density of the solution
c     The density of the droplet, a function of its composition,
c     changes as evaporation proceeds. It is estimated from models
c     of Celeda( Collection Czechoslovak Chem. Commun.,
c     vol 48, 1538-1551, 1983).
      den=1./(1. - 0.63568942*wfs)
10    rhs=((sqrt(den*wfs)*0.239142293-0.63568942)*wfs+1.)*den
      if ((abs(rhs-1.0)).le.1.e-5) go to 101
      den=den-(rhs-1)*den
      go to 10
c
c     The water vapor pressure above the solution surface is also
c     a function of composition. The compositional dependence of the
c     water activity (= relative humidity) is obtanied from Chapter
3     of this thesis, Table 2.
c
c
101   rh=1.0004-0.295351*wfs-0.113992*wfs**2+1.55769*wfs**3
      rh=rh-8.17712*wfs**4+6.98261*wfs**5

c
c     The subroutine srtsec calculate the steady state temperature
```

```
c     of the droplet at each decrement of droplet mass; subroutine
c     qromb calculates the time required for the droplet to lose its
c     weight to the new mass; polint is an interpolation routine
c     used in the integration routine of qromb. They are obtained
c     from Numerical Recipes: The Art of Scientific Computing,
c     W. H. Press, B. P. Flannery, S. A. Tenkolsky, and W. T.
c     Vettering, Cambridge UK, 1988.
c
c
           call srtsec(rtsec, tseq, 200., 400., 1.0e-4)
           call qromb(func, mo, m, s)
           s1=s
           tsurf=rtsec
           rtsec=tinf
           call qromb(func,mo,m,s)
           s2=s
           if ((s1.le.0.).and.(s2.le.0.)) go to 201
c     s1(sec) and s2(sec) are the time for each new mass of the
c     droplet when droplet cooling is and is not considered,
c     repectively.

c     m is in gram. it is now changed to voltage so that
c     experimental data can be directly compared.
           v=m/ms*vs
           write(*,*) j,s1,v,tsurf
100        format(1x, 4(4x,e12.4))
200        write(2,100) v,s1,tsurf,s2
201        stop
           end

           subroutine qromb(func,a,b,ss)
           parameter (eps=1.e-5,jmax=20,jmaxp=21,k=5,km=4)
           common tinf, pinf,rh,ms
           external func
c          jmaxp=jmax+1 and km=k-1
           dimension s(jmaxp), h(jmaxp)
           h(1)=1.
           do 11 j=1,jmax
c
                call trapzd(func,a,b,s(j),j)
                if (j.ge.k) then
                     jj=j-km
                     call polint(h(jj),s(jj),k,0.,ss,dss)
                     if (abs(dss).lt.eps*abs(ss)) return
                endif
                s(j+1)=s(j)
                h(j+1)=0.25*h(j)
11         continue
           pause 'too many steps'
           end
c
c
c
c
```

```
c
      subroutine trapzd(func,a,b,s,n)
      real a,b,s,ms
      common tinf, pinf,rh,ms

      if (n.eq.1) then

           s=0.5*(b-a)*(func(a)+func(b))
           it=1
      else
           tnm=it
           del=(b-a)/tnm
           x=a+0.5*del
           sum=0.
           do 10 j=1,it
                fx=func(x)
                sum=sum+fx
                 x=x+del
10         continue
           s=0.5*(s+(b-a)*sum/tnm)
           it=2*it
      endif
      return
      end

      real function func(x)
      real ms
      common tinf, pinf,rh,ms,den,d,rtsec
      psurf=(exp(-5313.88/rtsec+20.988))*rh
      func=-444.45/d/((x/den)**(1./3))
      func=func/(psurf/rtsec-pinf/tinf)
      return
      end

c
c
c
c
      subroutine polint(xa,ya,n,x,y,dy)
      parameter (nmax=10)
      dimension xa(n),ya(n),c(nmax),d(nmax)
      ns=1
      dif=abs(x-xa(1))
      do 11 i=1,n
           dift=abs(x-xa(i))
           if (dift.lt.dif) then
                ns=i
                dif=dift
           endif
           c(i)=ya(i)
           d(i)=ya(i)

11         continue
```

```
      y=ya(ns)
      ns=ns-1
      do 13 m=1,n-1
           do 12 i=1,n-m
                ho=xa(i)-x
                hp=xa(i+m)-x
                w=c(i+1)-d(i)
                den=ho-hp
                if (den.eq.0.) pause
                den=w/den
                d(i)=hp*den
                c(i)=ho*den
12         continue
           if (2*ns.lt.n-m) then
                dy=c(ns+1)
           else
                dy=d(ns)
                ns=ns-1
           endif
           y=y+dy
13    continue
      return
      end



      subroutine srtsec(rtsec,tseq,x1,x2,xacc)
      real m,ms,mo
      common tinf, pinf, rh,ms,den,d
      parameter (maxit=30)
      external tseq
      fl=tseq(x1)
      f=tseq(x2)
      if (abs(fl).lt.abs(f)) then
           rtsec=x1
           xl=x2
           swap=fl
           fl=f
           f=swap
      else
           xl=x1
           rtsec=x2
      endif
      do 11 j=1,maxit
           dx=(xl-rtsec)*f/(f-fl)
           xl=rtsec
           fl=f
           rtsec=rtsec+dx
           f=tseq(rtsec)
           if (abs(dx).lt.xacc.or.f.eq.0.) return

11    continue
      pause 'rtsec exceed maximum interations'
```

```
      end


      real function tseq(ts)
      common tinf,pinf,rh,ms,den,d
c
c     calculate surface temperture
c     heat of vaporization of water at 298K = 583 cal/g
c     thermal conductivity of air = 6.2e-5 cal/cm-s-K
c
      psurf=(exp(-5313.88/ts+20.988))*rh
      tseq=(tinf-ts)-2718.62*d*(psurf/ts-pinf/tinf)
      return
      end
```